Mechanochromic and Conductive Sensing for Crack Detection in FRP-Strengthened Concrete

An experimental study of self-sensing techniques for structural health monitoring

MSc Thesis

Arla F.G. van der Ende

Mechanochromic and Conductive Sensing for Crack Detection in FRP-Strengthened Concrete

An experimental study of self-sensing techniques for structural health monitoring

by

Arla Feline Georgette van der Ende

Student Number: 5168503

Thesis Committee: Dr. Mohammad Fotouhi (Chair)
Dr. ir. Fengqiao Zhang (Secondary supervisor)
Msc. Eyüphan Küçükkalfa (Daily supervisor)

Project Duration: April 2025 – December 2025
Faculty: Faculty of Civil Engineering and Geosciences, TU Delft
Cover: Cover photo by the author

TU Delft

Preface

This thesis marks the completion of my Master's degree in Structural Engineering at TU Delft. With this, my student life comes to an end. I am grateful for all the memories, experiences, and people I encountered during this time, and I look forward to finally applying what I have learned in practice within the field of Civil Engineering, while continuing to learn along the way.

This thesis focuses on the interesting and important field of Structural Health Monitoring and allowed me to bring theory into practice through experimental work. This research would not have been possible without the help of many people. First, I would like to thank my thesis committee. I thank Mohammad, my chair, for introducing this topic and for always being available to give feedback. I always felt welcome in your office, thank you for this. I would also like to thank Fengqiao for her continuous support, valuable feedback, and positive energy, which made working on this thesis even more enjoyable. Lastly, I thank Eyüphan, my daily supervisor, for your time and help in the lab. Thank you for the many hours you spent supporting me during specimen manufacturing and for your constant feedback on how things could be improved and for thinking along during my experiments. I also want to thank Baris Caglar for helping me at the beginning of my thesis and for thinking of new ideas.

Furthermore, I would like to thank the laboratory technicians for their support. I would like to thank Paul Vermeulen for his help with the electrical test setup. I really appreciated your enthusiasm for my topic and the time you spent helping me, including during the second round of testing. I also thank Ake Blom for his support during the experiments and for being flexible with my planning. In addition, I would like to thank Sam Reus for helping with the experiments and the electrical setup when Paul was not available. I am also grateful to Ton Blom for his help during the casting of the specimens, and to Maiko van Leeuwen for guiding me to the right people in the lab. Carrying out experimental research as a master's student can be challenging, and having people who are willing to help makes a big difference.

I would also like to note that I used AI-based tools to check my grammar. It was employed to help refine sentences and improve clarity where needed.

Finally, I would like to thank my family and friends. I thank my parents for always supporting me during my time in Delft. I am grateful to my friends, whom I could always rely on, also during my thesis period. I would also like to thank my EJD'22, Board 10, and everyone I met during my time at U-BASE. Thank you all for being part of this journey; it would not have been the same without you, and I am very happy to have you in my life. Lastly, I would like to give a special thank you to Hijme for supporting me over the past two years. I am happy to celebrate every milestone, big or small, with you and really appreciated the endless tea sessions we had during this period.

Arla van der Ende
Delft, December 2025

Summary

Aging infrastructure is increasingly subjected to degradation as structures approach the end of their service life. Consequently, monitoring, strengthening, and replacement of existing structures will play a crucial role in maintaining structural safety in the coming years. One effective strengthening technique for damaged concrete structures is Externally Bonded Reinforcement (EBR), in which Fiber Reinforced Polymer (FRP) composites are applied to the concrete surface. Recent developments include mechanochromic FRP systems that exhibit color changes in response to crack formation, offering visual damage indication.

This thesis investigates the feasibility of using the conductive carbon layer within a hybrid glass/carbon mechanochromic FRP to enable damage detection through electrical resistance measurements. The central research question is:

To what extent can electrical resistance measurements through a conductive network in mechanochromic composites be used to detect damage in FRP-retrofitted concrete beams under flexural loading?

Several methods for establishing electrical contact with the carbon layer were evaluated. Embedding copper strips between the glass and carbon layers proved to be a robust and reliable solution, providing stable electrical connectivity without significantly affecting the mechanical performance of the composite.

Four-point bending tests were conducted on concrete beams retrofitted with mechanochromic FRP to relate applied load, crack opening, color change, and fractional change in resistance (FCR). The results reveal a clear correlation between mechanical loading, crack development, and electrical resistance changes. The conductive carbon fiber network, measured using the Wheatstone principle, exhibited a mean gauge factor of 484 across three specimens, which is significantly higher than that of conventional metal strain gauges. This high sensitivity is attributed to the intrinsic piezoresistive behavior of the carbon fibers and their alignment within the composite, enabling the detection of very small strain levels.

The sensor response was repeatable and reliable in well-bonded specimens, allowing for early detection of damage associated with crack initiation and propagation. Notably, a consistent drop in electrical resistance was observed prior to ultimate failure, occurring at approximately 75% FCR and up to 50 seconds before failure, demonstrating the method's potential as an early-warning indicator. In contrast, specimens with insufficient bond quality exhibited inconsistent and specimen-specific electrical responses, limiting the reliability of damage interpretation.

Overall, the findings demonstrate that electrical resistance measurements in conductive carbon fiber composites are most effective as a global structural health monitoring technique. When adequate bond quality is ensured, the method enables reliable detection of damage initiation, progression, and pre-failure behavior in FRP-retrofitted concrete beams. The high gauge factor highlights the strong potential of this approach for sensitive, early-stage damage detection in structural applications.

Recommendations for future research include integrating direct strain measurements, optimizing sensor design and experimental setups, developing damage localization techniques, and conducting microstructural analyses of the carbon FRP. Further investigation under varying damage levels and loading conditions is also recommended.

Contents

Nomenclature

Abbreviations

Abbreviation	Definition
AE	Acoustic Emission
AFRP	Aramid Fiber Reinforced Polymer
CFRP	Carbon Fiber Reinforced Polymer
COD	Crack Opening Displacement
CV	Coefficient of Variation
DIC	Digital Image Correlation
EBR	Externally Bonded Reinforcement
EIS	Electrochemical Impedance Spectroscopy
FRP	Fiber Reinforced Polymers
GF	Gauge Factor
GFRP	Glass Fiber Reinforced Polymer
LVDTs	Linear Variable Differential Transformers
NDE	Non-Destructive Evaluation
RC	Reinforced Concrete
SHM	Structural Health Monitoring
STD	Standard Deviation
ULS	Ultimate Limit State

Symbols

Symbol	Definition	Unit
I	Current	[A]
R	Resistance	[Ω]
U	Voltage	[V]
ϵ	Strain	[-]
ρ	Electrical resistivity	[Ω mm]

1 Introduction

1.1. Background and motivation

In many parts of the world, large infrastructure assets are reaching the end of their designed service life. As a result, degradation occurs in both their structural and mechanical properties. This deterioration can lead to situations where structures no longer meet the load-bearing capacity or safety requirements for which they were originally designed. In the Netherlands in particular, tens of thousands of structures, including bridges, railways, and roads, will need to be replaced or renovated in the coming decades. Most of these assets were designed for a lifespan of approximately 50 to 100 years. However, due to the high costs of construction and the significant environmental impact, with CO_2 emissions, it is important to accurately assess how long these structures can continue to function safely and effectively. From a technical perspective, complete replacement is not always necessary. Many structures were designed using conservative assumptions and safety factors based on the engineering knowledge available at the time. Advances in research and monitoring techniques have since then shown that these design rules can be conservative, suggesting that the actual remaining lifetime of many structures may be longer than initially expected [1].

Structural Health Monitoring (SHM) is the process of monitoring damage during service life of a structure [2]. Several methods are developed to monitor the structural health of civil structures such as radiography, ultrasonic pulse velocity and acoustic emission testing [3]. Other methods focus on strengthening or repairing structures to extend its service life, such as adding braces or injecting grout to fill cracks in concrete [4]. One specific method for strengthening damaged concrete structures is by using Fiber Reinforced Polymers (FRP), also referred to in this thesis as composites. Composites can be used to externally reinforce damaged concrete. This is a fast and flexible way of strengthening a concrete structure since the properties of composites are tailorable.

Detecting cracks in structures at an early stage is crucial for preventing failures and ensuring timely management. In the research by Czél et al., a mechanochromic hybrid glass/carbon composite was developed [5]. Mechanochromic materials change their optical properties, such as color, in response to mechanical forces [6]. This composite provides immediate visual feedback by changing colors when cracks occur in the material. Importantly, the color changes are induced by deformation and cracking in the underlying substrate, allowing the composite to act as an indicator of damage in the material it is applied to.

The research conducted by Mohammadi et al. expanded on this work by applying the mechanochromic composite for the retrofitting of concrete structures. In this application, the color changes in the composite provide an early warning system for cracks in the concrete substrate, enabling easier visual detection of structural damage [7].

Traditional SHM is an expensive and time-consuming process that requires extensive cabling along a structure to record data [8]. Installing these cables is labor-intensive, especially for large or hard-to-reach structures. Recent research focuses on optimizing these sensors by eliminating the need for cables and instead using a conductive network, making the system more cost-effective, easier to implement, and less power-consuming. However, when applied to FRP retrofitted structures, monitoring remains complex due to various potential damage mechanisms, such as debonding, fiber rupture, or cracking of the concrete beneath the composite. These damage processes are difficult to track with traditional instruments and still require extensive cabling setups [9].

In this context, mechanochromic composites present a promising alternative by offering an immediate color change in response to mechanical stress. Although mechanochromic composites simplify the monitoring process, they still rely on frequent visual inspections. To further enhance their monitoring capability, the integrated carbon layer within the composite could be utilized as a conductive network for electrical-based damage detection. This visual cue and electrical responses, have the potential to provide more reliable and continuous structural health monitoring without the need for extensive external sensors or cabling.

1.2. Research Objective

The objective of this research is to investigate the potential of using a conductive network for electrical resistance measurements in mechanochromic composites, with the aim of enabling damage detection for retrofitting concrete structures using FRP. The mechanochromic composite includes a carbon-based layer that is inherently conductive, and this study explores methods to utilize this property for self-sensing purposes. Furthermore, the research investigates whether the cracks indicated by the visual color change of the mechanochromic composite correspond to those detected by Digital Image Correlation (DIC), and whether changes in electrical resistance correlate with the crack patterns identified by DIC.

1.3. Research scope

This research focuses on electrical resistance measurements of retrofitted concrete beams strengthened with mechanochromic composites. The retrofitting is limited to flexural strengthening using the same lay-up of glass and carbon layers as described by Mohammadi et al. [10]. This study does not investigate the use of different types of FRP materials that could also serve as a conductive network. Electrical resistance measurements will be conducted under four point bending load conditions only.

In addition, the study aims to evaluate the correlation between electrical resistance changes and damage progression identified through DIC and visual color changes in the mechanochromic composite. The scope is therefore confined to the experimental validation of this combined monitoring approach, without extending to long-term durability, environmental effects, or large-scale structural applications.

1.4. Research questions

The main research question addressed in this study is:

To what extent can electrical resistance measurements through a conductive network in mechanochromic composites be used to detect damage in FRP-retrofitted concrete beams under flexural loading?

With the following subquestions:

1. What methods can be employed to integrate a conductive network within mechanochromic composites for the purpose of electrical resistance-based damage detection?
2. How does the electrical resistance of the mechanochromic composite change under flexural loading in retrofitted concrete beams?
3. To what extent do changes in electrical resistance correlate with cracks identified by DIC and visual color changes?
4. How sensitive are the conductive network sensors embedded in the mechanochromic composite as quantified by the gauge factor?

1.5. Thesis outline

Chapter 2 presents a literature review covering the material behaviour of concrete and composites, the principles of structural retrofitting, the concept of mechanochromic composites, and the use of conductive carbon composites for electrical resistance–based damage detection. Chapter 3 describes the methodology used in this research, including the manufacturing of the concrete beams and composite laminates, the sensor integration methods, and the experimental testing program. Chapter 4 presents the experimental results, while Chapter 5 provides a discussion and interpretation of these findings in relation to the research questions. Finally, Chapter 6 contains the conclusions drawn from the study, and Chapter 7 presents recommendations for future research.

2 Literature study

To understand the benefit of mechanochromic composites for the purpose of externally reinforce concrete, it is important to explore the different materials, their properties, and the ways in which they interact. This includes an examination of concrete and its limitations, existing retrofitting techniques, the role of (mechanochromic) composites and their specific layouts, and finally the principles of using electrical resistance measurements for damage detection and their integration into SHM.

2.1. Concrete

As mentioned in Chapter 1, much of our existing infrastructure is reaching the end of its service life. High construction costs and the associated CO_2 emissions have limited the realization of new projects. Since concrete is the most widely used construction material in the world, known for its excellent compressive strength but low tensile capacity, it is essential to assess the condition of concrete structures. Therefore, it is important to understand the types of concrete cracks and the current available monitoring techniques.

2.1.1. Types of cracks in concrete

Cracks in concrete are an indicaton of the state of a structure. Cracks in concrete are visible in different stages in lifetime for different reasons. These cracks can be categorized as occurring in plastic or hardened concrete. Table 2.1 provides an overview of cracks occurring in both plastic and hardened concrete, with particular emphasis on the mechanisms and causes of cracking in hardened concrete [11].

Plastic Concrete	**Hardened Concrete**
• Plastic shrinkage cracking	• Drying shrinkage
• Settlement cracking	• Thermal stresses
	• Chemical reaction
	• Weathering
	• Corrosion of reinforcement
	• Poor construction practices
	• Construction overload
	• Errors in design and detailing

Table 2.1: Causes of cracking in concrete [11]

2.1.2. Crack width control

The Eurocode (NEN 1992-1-1) provides general guidelines for crack control that must be considered when designing concrete structures. A maximum allowable crack width, w_{max}, is specified in this standard, taking into account the exposure class and load combination. Crack width control is typically applied to steel-reinforced concrete. When cracks develop in the concrete, the steel reinforcement carries the tensile forces, and the exposure of the reinforcement to the environment through the cracks is kept limited. For this reason, the Eurocode prescribes a crack width limit generally between 0.1 and 0.4 mm [12].

2.1.3. Crack monitoring in concrete structures

The presence of cracks indicates that the structural performance is lower than originally intended. As said, structures are often designed with a maximum allowable crack width, the location and timing of a crack can influence the overall performance of the structure.

Therefore, monitoring cracks in concrete throughout the service life is essential. A common method involves inspecting the structure regularly using a crack width ruler, which can be seen in Figure 2.1. While this approach is simple, it is labor-intensive and prone to human error, which limits its accuracy and reliability. Nowadays, alternative devices for tracking crack widths have become available. For instance, trained algorithms can analyze cracks based on photographs taken with a smartphone [13].

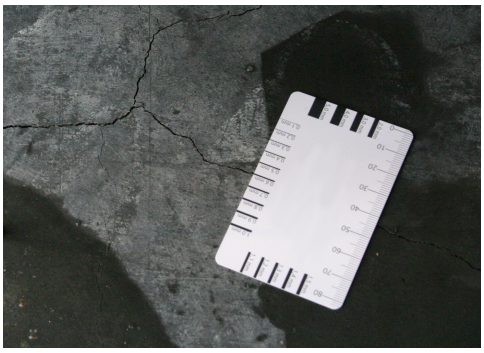

Figure 2.1: Example of a crack width ruler [14]

The cracks that will be investigated in this research are flexural bending cracks of plain concrete. These type of cracks occur in hardened concrete due to overloading in the tension side of concrete. In that case, the tension stress is higher than the tension strength of concrete and flexural cracks occur.

2.2. Composites and FRP

The terms *composites* and *FRP* are often used interchangeably. A composite is a material composed of two or more constituents that, when combined, exhibit improved properties compared to the individual components. For example, a concrete beam combined with a steel plate can be regarded as a composite. FRP consists of fibers and a resin, and can therefore be considered a type of composite [15].

Components of FRP
The fibers in FRP provide the load-bearing function. Fibers are grouped into bundles to form a reinforcement, arranged either unidirectionally or bidirectionally to form mats. Different fiber types include, Glass fibers (GFRP), Carbon fibers (CFRP) and Aramid fibers (AFRP). Each fiber type has distinct mechanical properties and strengths.

The resin (or polymer matrix) serves several functions [16]:

1. Fixing the fibers in place
2. Transferring forces between fibers
3. Preventing fiber buckling
4. Protecting the fibers from environmental damage

Types of Resin
There are two main types of resins:

- **Thermoset resins:** permanently set after polymerization and cannot be reshaped by heating.
- **Thermoplastic resins:** soften when heated and return to their solid state upon cooling.

Common polymers used include Polyester, Vinylester, and Epoxy.

Manufacturing Techniques
Several manufacturing methods are available depending on the geometry and project requirements. Pre-impregnated fibers (*prepregs*) are fibers impregnated with a controlled amount of thermosetting epoxy. Other techniques include vacuum infusion, where resin is drawn into dry fiber layers using vacuum pressure, and hand lay-up, a manual method in which resin is applied by hand or roller. Prepregs can be stacked in specific orientations, making this method less labor-intensive than vacuum infusion or hand lay-up.

Advantages
A major advantage of FRP is its tailorability: the fiber type, resin, fiber orientation, and amount can all be customized for a specific project [17].

2.3. Retrofitting

2.3.1. What is Retrofitting?

Retrofitting refers to adding a new component or feature, which was not there at the time of original construction, in order to improve the load-bearing capacity of an existing structure. On structural level, there are many ways to retrofit a concrete structure in order to restore the strength. Structural retrofitting can be done on :

1. Local member level;
2. Global structural level

Concrete retrofitting is usually done by the use of external steel plates, called steel jacketing. However, it is shown that FRP has certain advantages over the use of steel plates regarding retrofitting. Steel plates are generally more heavy to transport, prone to corrosion and there are limitations regarding available dimensions. Therefore, FRP can be more convenient compared to steel, also considering the higher strength and lower density than steel [18].

2.3.2. Externally Bonded FRP Reinforcement

FRP is used as strengthening material for reinforced concrete (RC). The reasons why FRP is used as strengthening are: high corrosion resistance, low weight, no need for scaffolding systems, reduction of labor costs, and tailorable to the design requirements. Disadvantages of using FRP for strengthening are composites are in general linear elastic to failure, which reduces the ductility. Also the thermal expansion coefficients from carbon or aramid are different to those of concrete. Exposure to high temperatures can cause early degradation and collapse. Therefore, steel reinforcement should not immediately be replaced by FRP, but this should depend on factors such as mechanical performance, constructibility, and long-term durability. Retrofitting concrete structures on global level by FRP is usually done as Externally Bonded Reinforcement (EBR) to enhance the shear, flexural or compression capacity of structural element. FRP retrofitting is in recent years often used in seismically active regions, due to its fast and flexibel way to strengthen a damaged structure [17][19]. The stress-strain diagram for unidirectional composites is shown in figure 2.2 to make a comparison with steel. It can be seen that the ultimate stress is higher for FRP than for steel.

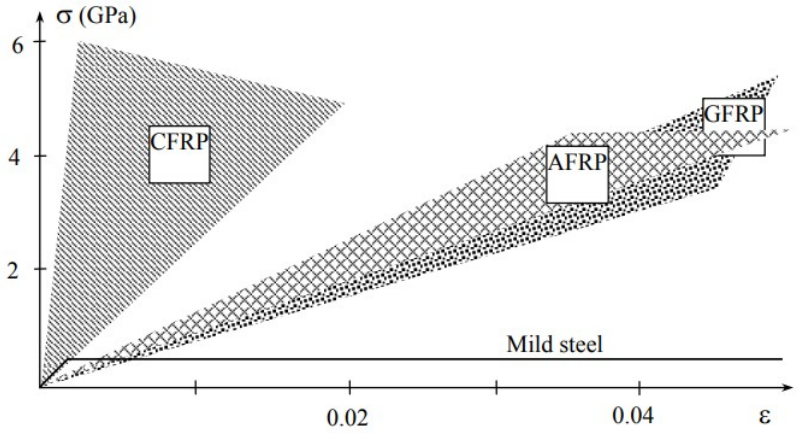

Figure 2.2: Stress-strain diagram for different unidirectional FRPs and steel. (CFRP = carbon FRP, AFRP = aramid FRP and GFRP = glass FRP) [17]

EBR is typically applied either by the hand lay-up (wet lay-up) method or by using pre-cured composite systems, shown in Figure 2.3. For both methods, surface preparation such as removing dust and cement paste needs to be done before applying adhesives in order to limit debonding.

Hand lay-up
This method consists of using dry or preimpregnated fabrics in situ. When dry fabrics are used, a resin is applied to the fabric after using a primer on the concrete surface.

Pre-cured systems
This method uses pre-manufactured and cured FRP laminates to attach to the concrete surface using an adhesive.

(a) Hand lay-up [16]

(b) Pre-cured laminates applied with an adhesive [20]

Figure 2.3: Two types of retrofitting concrete structures with FRP

2.3.3. Failure Modes

There is currently no specific design code, such as the Eurocode, that describes the retrofitting of concrete structures with FRP. However, a design document for the use of FRP in civil engineering structures (the JRC document) has been developed and is considered a potential basis for a future Eurocode. In addition, several design guidelines for retrofitting concrete with FRP are already available. Among these, the fib Bulletin 14 was the first to be published and will be used as the main reference for this research [19].

Flexural strengthening
Often, EBR is used to increase the flexural strength of members. Fibers need to be glued parallel to the direction of the principal stress to increase the flexural capacity [19]. The ultimate limate state (ULS) is analyzed that a) the external FRP reinforcement is taken into account and b) special consideration is given to debonding issues [17].
ULS failure modes can be divided into full composite action and loss of composite action, see Figure 2.8 for the different types of failure modes. Full composite action consists of FRP rupture or concrete crushing (compression failure or shear failure). Loss of composite action consists of different type of debonding failures. These failure types happen often sudden and are brittle failure, which limits the achievement of a specific strength [19].

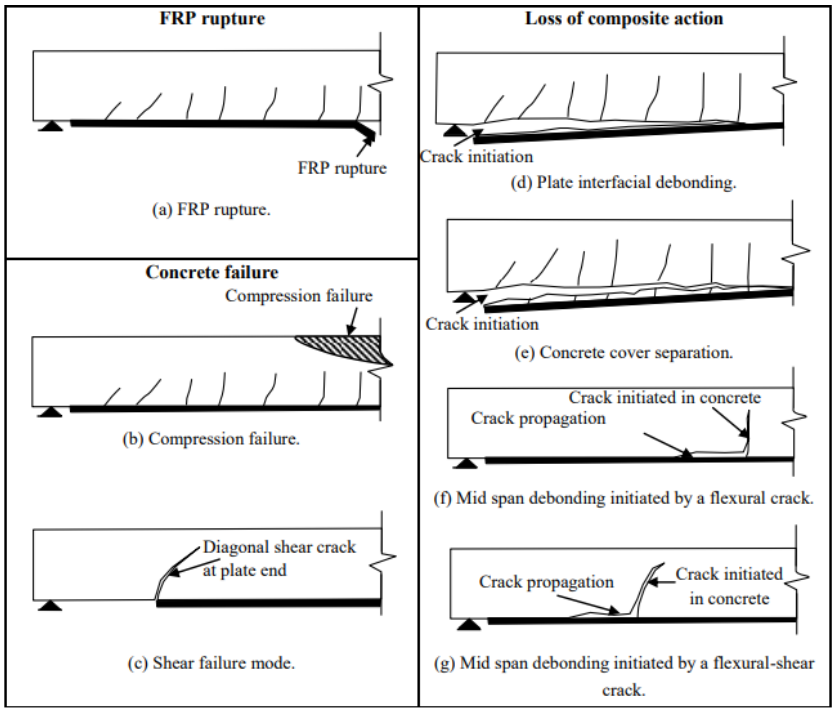

Figure 2.4: Failure modes flexural retrofitted beam [19]

Multiple studies have focused on the structural behaviour of RC beams retrofitted with FRP. Often, a combination of shear and flexural retrofitting is applied, since shear failure typically initiates near the supports and can result in sudden collapse, whereas flexural failure is more ductile. The study by Durgadevi et al. investigated the retrofitting of a concrete beam reinforced with longitudinal steel bars and stirrups. Three different types of FRP: glass, carbon, and basalt were fully wrapped around the beam using either two or four layers. The specimens were tested to failure under a four-point bending configuration, and deflections were recorded using Linear Variable Differential Transformers (LVDTs). The results showed that wrapping a steel-reinforced beam with two to four FRP layers increased the load-bearing capacity by 8–32%. Deflections were reduced for all specimens, and CFRP retrofitting proved to be the most effective in enhancing flexural strength [21].

Similarly, Kachlakev and McCurry investigated the structural behaviour of beams retrofitted flexurally with unidirectional CFRP, in shear with unidirectional GFRP, and with a combination of both [22]. Their results demonstrated that flexural retrofitting with CFRP can increase the static load-bearing capacity by up to 150%, depending on the failure mode, geometry, and material properties. The load corresponding to the first visible crack increased by approximately 23% due to the additional stiffness provided by the CFRP. Moreover, in beams retrofitted only flexurally with CFRP, without any steel shear reinforcement, diagonal tension cracks were observed. In such cases, the CFRP fibers were able to maintain integrity even after shear cracking. Normally, shear failure leads to transverse rupture of the composite, resulting in matrix shear failure and premature collapse.

2.3.4. Monitoring

A limitation of FRP retrofitting is that it is difficult to see what is happening to the concrete surface underneath the composite, especially regarding concrete crack propagation, but also debonding. Different studies have been conducted on various monitoring techniques using FRP and concrete.

A Non-Destructive Evaluation (NDE) for the debonding of CFRP and concrete beams is done by Hong et al. using Electrochemical Impedance Spectroscopy (EIS). As described, debonding is a common failure mode, therefore it is important to inspect the integrity of the interfacial bond between concrete and FRP. Visual inspection is not always a reliable method and 'tap' tests are time consuming and can not always be done in difficult to access areas. Three sensor elements were used: copper tape with conductive adhesive, stainless steel wire placed in grooves on the bottom of the concrete and a reinforcing bar. Impedance measurements within the internal wire sensors revealed the location of the debonded regions. This EIS sensor technology showed an inexpensive and effective way to determine debonding between CFRP and concrete [23].

Different techniques for monitoring during experiments on retrofitted reinforced concrete beams were investigated by Pohorles et al [24]. This research focuses on the measurement of effective strain and debonding using different monitoring techniques: Electrical strain gauges, Fiber Bragg Grating sensors, and DIC. These techniques are used to monitor strain on the concrete or composite surface. Acoustic Emission (AE) sensors are used to assess debonding mechanisms of the composite, while LVDT is used to measure vertical deflection of the beam. This research showed that DIC and AE are very useful for monitoring strain and displacement on retrofitted concrete beams. AE can accurately determine the development of debonding and DIC can give quantitive information about the effective strain on the specimen surface. It also showed that AE analysis gives more depth compared with simple observations because it can identify and classify cracks below the surface of FRP, without any visual observation.

2.4. Chromogenic materials

Chromogenic materials react to a force, temperature, humidity or light and this provides an optical variation, such as color, fluoresence or force [25]. Among these chromogenic materials, mechanochromic materials react specifically to mechanical forces. Different applications in different fields are using these types of chromogenic materials to make environmental variation visual by eye. From a structural point of view, these materials are useful to detect elastic or plastic deformation and can be used for structural health monitoring purposes [26]. Mechanochromic composites can be categorized in two groups, chemical based and phyical based. Chemical based composites uses pigments or dyes to visualize mechanical variation. While physical based composites changes color due to an external source, such as light, heat or strain [10].

2.4.1. Mechanochromic glass/carbon hybrid FRP

Mechanochromic glass/carbon hybrid FRP are a specific type of mechanochromic material, designed in such a way that the color change occurs when loaded beyond a predefined strain level. This material consists of a "sensing" carbon layer and a glass outer layer. The principle of this design is that the sensor, the carbon layer, experiences similar strains as the material beneath, called the "substrate". When the failure strain of the carbon layer is exceeded, different fractures develop, and the incident light reflects back from the damaged carbon layer, showing light stripes. An illustration of this, can be seen in Figure 2.5. This interfacial damage is caused by the damage to the carbon fiber layer, followed by delamination[27].

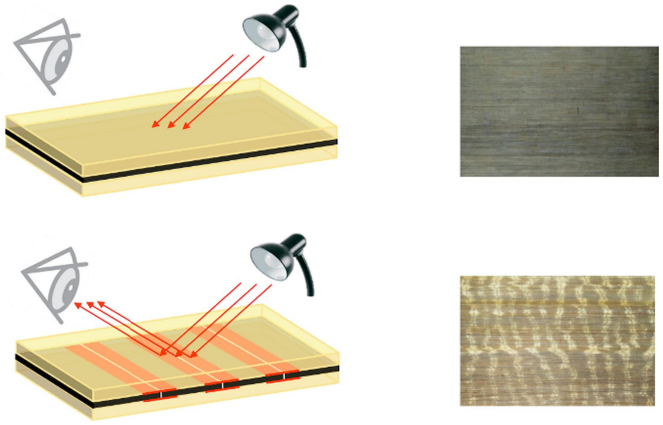

Figure 2.5: Illustration of the principle of light stripes in mechanochromic composites [2]

Different studies have been conducted to check the sensor response and its accuracy [5] [28]. Uniaxial tensile tests of co-cured retrofitted composite specimens were carried out to compare the color changes in the sensor layer. DIC and AE were used to verify the fragmentation of the hybrid sensor. This showed that the AE results match the appearance of the first crack in the carbon sensing layer and that the DIC images taken during the experiments correspond with the color change [2].

An extension of this work was performed by Mohammadi et al., where this type of mechanochromic composite was used for concrete retrofitting purposes. In this research, different types of damage levels on retrofitted concrete beams were tested and compared with non-retrofitted beams. These damage levels where obtained by using 5 and 15 mm notches which aligns with 5% and 15% compared to the height of the beam. This study showed that flexural retrofitting of concrete with this type of mechanochromic composite can improve the load-bearing capacity by up to 208% for non-steel-reinforced concrete beams.
In this study five glass layers, one carbon layer, and one top glass layer are used to retrofit the concrete . The first five additional glass layers are used to flexurally strengthen the concrete more. YSH-90 carbon fiber and S-glass prepregs with Epoxy Hexply@913 were used. It was shown that the mechanochromic effect can be used both to detect cracks in the concrete and to strengthen it [7]. In Figure 2.6 the mechanochromic effect on the retrofitted concrete beam can be seen after testing. Figure 2.7 shows the results that are obtained with four-point bending tests for different test groups.

Figure 2.6: Mechanochromic effect on retrofitted concrete beam [7]

Group	specimen	F_{max} (kN)	Deflection (δ_{max}) (mm)	Average F_{max}	Averageδ_{max}
REF	C1	18.01	0.257	17.43	0.246
	C2	18.50	0.238	± 1.43	± 0.009
	C3	15.81	0.244		
5 % damage	LD1	12.15	0.287	12.18	0.293
	LD2	12.08	0.301	± 0.12	± 0.007
	LD3	12.33	0.293		
15 % damage	HD1	7.87	0.212	9.10	0.237
	HD2	9.88	0.241	± 1.08	± 0.024
	HD3	9.57	0.260		
Retrofitted	RLD1	46.10	1.445	50.76	1.603
5 % damage	RLD2	53.27	1.703	± 4.04	± 0.138
	RLD3	52.92	1.661		
Retrofitted	RHD1	32.62	1.041	50.03	1.592
15 %	RHD2	62.34	1.960	± 15.5	± 0.486
damage	RHD3	55.13	1.777		

Figure 2.7: Results four point bending test different test groups [10]

2.5. Damage detection using the concept of electrical resistance

Damage detection based on the concept of electrical resistance is not new. Multiple studies have demonstrated that incorporating conductive elements into materials can create a "sensing" network for monitoring structural integrity. Such networks can be implemented in both concrete and FRP materials.

In FRP, this can be achieved either by (i) adding conductive elements such as carbon particles, nanomaterials, or carbon fibers to a non-conductive matrix, or (ii) by using the conductivity properties of a carbon fiber reinforced polymer (CFRP) [2]. Damage in FRP is typically related to irreversible fiber breakage, delamination, matrix deterioration, interfacial debonding, and elastic strain caused by microstructural changes as illustrated in Figure 2.8. The electrical properties of CFRP are influenced by strain, temperature, and damage [29].

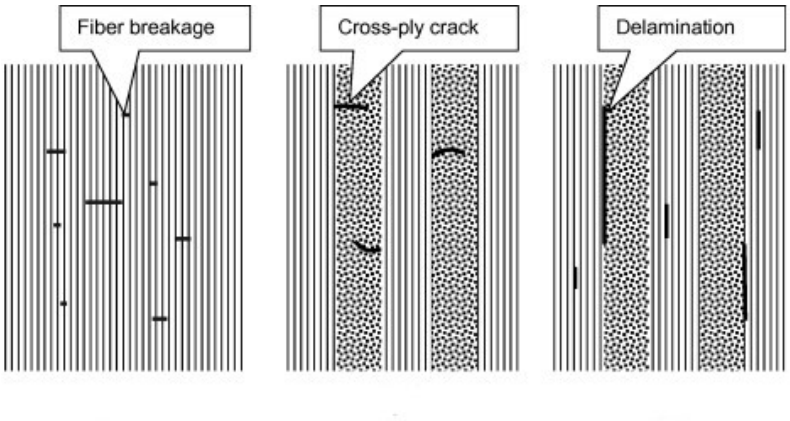

Figure 2.8: Types of damages in FRPs [30]

CFRP can be used for electrical conductivity, although they exhibit certain unfavorable characteristics. Carbon fibers are good electrical conductors, but the epoxy matrix between the fibers acts as an electrical insulator. Furthermore, the orientation of the fibers determines the electrical anisotropy: conductivity is higher along the fiber direction and lower perpendicular to it. As a result, unidirectional CFRP typically has lower conductivity than bidirectional CFRP. Under ideal conditions, the current would flow through individual fibers. However, due to the wavy nature of carbon fibers, contact points occur between adjacent fibers. When the fibers are stretched, the number of contact points decreases, see Figure 2.9, resulting in an increase in resistance. These contact points allow current to pass from one fiber to another. Consequently, unidirectional CFRP laminates show anisotropic electrical behavior, with higher conductivity along the fiber direction than across it [29]. This is an important factor to consider when performing electrical measurements on CFRP for damage detection.

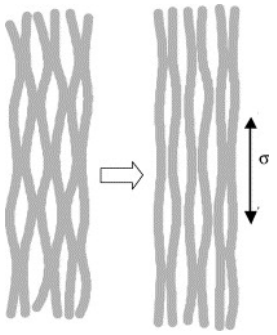

Figure 2.9: Curving carbon fibers in CFRP [31]

The resistance of CFRP can be calculated using the following formula.

$$R_{CFRP} = \rho \frac{L}{A} \tag{2.1}$$

where R_{CFRP} is the resistance of the CFRP [Ω], L is the length between the two electrodes [mm], ρ is the electrical resistivity of the fiber [Ω mm], and A is the cross-sectional area [mm^2].

From the study done by Wen et al., it can be concluded that electrical resistance change is linearly proportional to strain due to the conductive fibers and that damage in the fibers will show sudden increase in resistance [30]. In another study by Alexopoulos et al., carbon nanotube (CNT) fibers were embedded within glass fibers for sensing and damage monitoring purposes. The study demonstrated that embedding CNT fibers into a non-conductive composite does not degrade the mechanical properties of the material and that a direct correlation exists between mechanical loading and changes in electrical resistance [32].

Electrical resistance measurements can also be applied to concrete by adding conductive elements. In a study by Jiang and Wu, various dosages of steel fibers and nano-carbon black were used to detect cracks through resistance measurements. The objective was to achieve self-monitoring of concrete cracking and crack development. The study examined the variation in resistance with load, deflection, and crack opening displacement (COD) during three-point bending tests. Results showed that the resistance change was zero before cracking, and increased rapidly as the concrete beam cracked [33].

Research by Malik et al. focused on the use of metallic foils co-cured on top of carbon fibers to form stable electrodes with low electrical contact resistance. Establishing good electrical contact between carbon fibers and external sources is challenging, as the polymer matrix acts as a barrier, resulting in high contact resistance. Electrode fabrication techniques can generally be divided into two categories:

1. Co-cured electrodes integrated with the carbon fibers, and
2. Electrodes applied to cured composites after surface preparation.

The latter approach is less favorable due to the risk of surface damage during preparation. In the research by Malik et al., two co-cured electrode concepts were tested: electrically conductive metal foils and thermosetting conductive paint. Different electrode thicknesses and spacings, the distance between electrodes, were evaluated to measure resistance. The study showed that copper foil electrodes exhibit the lowest contact and interface resistance, followed by silver paint and brass foils. Electrode thickness above 0.02 mm had no significant effect on total resistance, while electrode lengths greater than 2.5 mm did not influence interface resistance. It also showed that autoclave curing, which applies both temperature and pressure, significantly reduces the contact resistance [34].

2.6. Research Gap

From the literature review, the following conclusions can be drawn:

- FRP can effectively strengthen concrete externally, with performance depending on the type of FRP, the number of layers, and the strengthening configuration.
- The bond between concrete and FRP is critical and often governs the failure mechanism.

Mechanochromic Composites

- Digital Image Correlation (DIC) results show that crack patterns can be correlated with visible color changes in mechanochromic composites.
- Mechanochromic composites show promising potential for flexural strengthening of concrete beams, while simultaneously enabling visual detection of flexural cracks.

Electrical Measurements

- Previous studies indicate that CFRP or FRPs with added conductive components can be used for damage detection in the composite through electrical measurements.
- Metallic foils can be applied on top of CFRP layers to form stable electrodes.
- Establishing a reliable electrical contact remains challenging due to the insulating nature of the polymer matrix.

Based on the reviewed literature, it can be concluded that flexural retrofitting of concrete with FRPs enhances structural performance. When mechanochromic composites are used, this strengthening effect is complemented by the ability to visually detect cracks through color change. Although the use of CFRP for damage detection via electrical measurements has been reported, there is a lack of research focusing on hybrid or layered FRP systems that combine multiple fiber types (GFRP and CFRP) or integrate sensing capabilities. To the best of the author's knowledge, no studies have yet examined the performance of electrical measurements on FRP retrofitted concrete incorporating such hybrid composite systems.

3 Methodology

The main objective of this experimental study is to investigate the potential of using a conductive carbon layer prepreg embedded between glass layers to enable resistance measurements on FRP-retrofitted concrete for damage detection. For this, a reliable method for connecting the embedded carbon layer to a measurement device need to be established. The experimental program includes electrical resistance measurements on FRP specimens in static condition, compression tests on concrete cubes, and four-point bending tests on FRP-retrofitted concrete beams in order to collect resistance change data. Firstly, nine retrofitted beams where tested and reviewed, which will be referred to as ***Iteration 1***. Afterwards, another three beams were tested with an optimalised design and manufacturing process, which will be referred to as ***Iteration 2*** in this chapter.

3.1. Experimental Methodology

In Figure 3.1 the steps regarding the experimental program are shown.

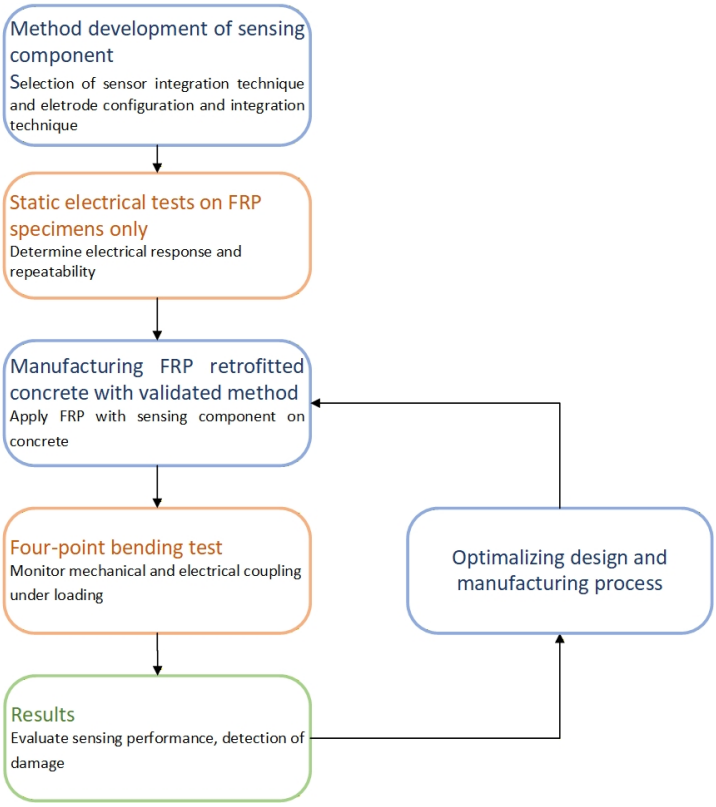

Figure 3.1: Flow Diagram Experimental Methodology

3.2. Concrete manufacturing

3.2.1. Mixture properties

The concrete mix used in this research, is based on the paper from Mohammadi et al, which is an uniform concrete mix. The concrete mix is shown in Table 3.1.

Component	Weight [kg/m^3]
CEM I 42.5 N	586.70
Water	79.13
Sand (2-4 mm)	698.85
Gravel (4-16 mm)	1247.94

Table 3.1: Proportions of concrete mix

3.2.2. Casting specimens

In the end, two casting days were executed. On the first day, ten concrete beams with dimensions 100 × 100 × 400 mm (lxbxh) were cast, along with two concrete cubes measuring 150 × 150 × 150 mm. Since the mix ended up more sticky then expected, there was not enough mix left for three cubes. These concrete cubes are used for testing the concrete strength. On the second day, four beams and four concrete cubes were cast.

On the day before the casting, the moulds were cleaned and oiled. Firstly, the cement was mixed with the sand and gravel, then the water was gradually added to create a well-mixed mixture. Secondly, the moulds were filled with the mixture. After the molds were filled, the vibration table is used to remove the air bubbles inside the concrete. It was noticed that no excessive bleeding occurred. Lastly, the concrete specimens were sealed with a plastic foil to retain a moist environment. After one day, all specimens were demoulded and placed in a climate room with a relative humidity above 95 percent for the following 27 days to optimize the hardening process. Images of the casting and curing process can be found in Appendix A.

3.2.3. Concrete testing

The compressive strength is measured using a loading rate of 13.5 kN/s, following NEN-EN 12390-3, 2019 and calculated from Formula 3.1.

$$f_c = \frac{F}{A_c} \tag{3.1}$$

Where f_c is the compressive concrete strength in MPa, F is the maximum load at failure in N, A_c is the cross-sectional area in mm^2

The mean compressive cube strength can be calculated to the mean compressive cylinder strength using Formula 3.2 from the Eurocode NEN-EN-1992-1.

$$f_{cm,cube} = 1.25 * f_{cm,cylinder} \tag{3.2}$$

The corresponding 28-day mean concrete cube strength can be calculated using Formulas 3.3 and 3.4.

$$f_{cm}(t) = \beta_{cc}(t)\, f_{cm} \tag{3.3}$$

with

$$\beta_{cc}(t) = \exp\left\{ s \left[1 - \left(\frac{28}{t} \right)^{1/2} \right] \right\} \tag{3.4}$$

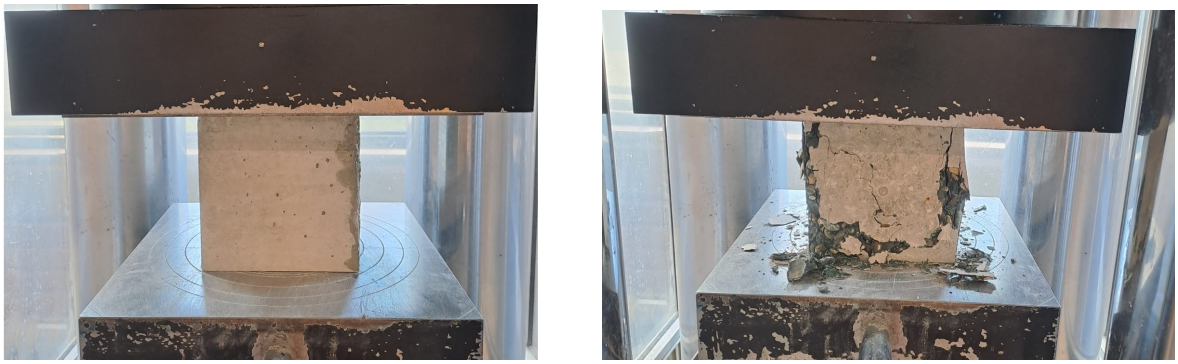

(a) (b)

Figure 3.2: Concrete compression test, before (a) and after (b)

- f_{cm} is the mean compressive strength at 28 days
- $\beta_{cc}(t)$ is a coefficient which depends on the age of the concrete t
- t is the age of the concrete in days
- s is a coefficient which depends on the type of cement:
  - $= 0.20$ for cement of strength Classes CEM 42.5 R, CEM 52.5 N and CEM 52.5 R (Class R)
  - $= 0.25$ for cement of strength Classes CEM 32.5 R, CEM 42.5 N (Class N)
  - $= 0.38$ for cement of strength Classes CEM 32.5 N (Class S)

$$f_{ck}(t) = f_{cm}(t) - 8MPa \tag{3.5}$$

Batch 1
Batch 1 is tested after 35 days instead of the usual 28th days due to unforeseen closure of the lab. The compressive strength of the two cubes after 35 days are respectively 64.80 and 60.64 MPa. Since only two cubes were tested, the lowest measured value, 60.6 MPa, is taken as the mean concrete cube strength ($f_{cm,cube,35}$). Applying formulas 3.2, 3.3 and 3.4, it is found that the mean compressive cylinder strength at 28 days, ($f_{cm,cylinder,28}$), is 47.47 MPa. Formula 3.5 is used to calculate the characteristic cylinder compressive strength at 28th days. This gives a strength of 39.5 MPa, which belongs, according to Eurocode NEN-EN-1992-1, to concrete class C35/45.

Batch 2
The four concrete cubes of Batch 2 were also tested after 35 days. The cubic compressive strength is found to be 47.15, 66.01, 69.26 and 66.39 MPa. This gives a mean concrete cube strength of 62.20 MPa. The same approach as batch 1 using formalas 3.2, 3.3 and 3.4, gives a mean compressive cylinder strength at 28 days ($f_{cm,cylinder,28}$) of 48.72 MPa. Applying formula 3.5 gives a characteristic cylinder strength of 40.72 MPa. Similar and expected as batch 1 this belongs to concrete class C35/45.

In conclusion, both batches show similar results which corresponds to concrete class C35/45.

3.2.4. Concrete Notch Fabrication

For six specimens in Iteration 1 of the experiments, notches were introduced. Notches serve to create a stress concentration at the tip, thereby reducing the material's fracture resistance. At these notches, initial microcracks are likely to form, which can propagate to macrocracks and eventually lead to failure [35]. In this study, the notches are intended to simulate damage levels in concrete that has been retrofitted with FRP. To allow for comparison, the same damage levels as those used by Mohammadi et al. [10] were adopted. Specifically, three specimens were prepared with low damage and three with high damage, corresponding to notch depths of 5 mm and 15 mm, respectively. These depths represent damage levels of approximately 5% and 15%. All notches have a width of 2 mm. In Table 3.2 are the different specimens shown for each iteration with each damage level.

Iteration	Specimen	Damage [mm]
1	REF1	0
1	REF2	0
1	REF3	0
1	RLD1	5
1	RLD2	5
1	RLD3	5
1	RHD1	15
1	RHD2	15
1	RHD3	15
2	2-REF1	0
2	2-REF2	0
2	2-REF3	0

Table 3.2: Overview of specimens testing

The notches were made using a diamond grinding disk. First, the depth of the notches were indicated with a marker on the beam. Then, the notches were carefully made, while water was spraying to minimalize dust particles, this process is shown in Figure 3.3.

Figure 3.3: Creating notches in concrete beams using a diamond grinding disk

3.3. Evaluation of Electrical Methods on FRP

3.3.1. Implementing Electrical Connections in the Embedded Carbon Layer

Establishing an electrical connection between the embedded carbon layer and external measurement equipment requires a reliable and non-destructive approach. This is challenging, as the carbon layer is enclosed between glass fiber layers. Several alternative methods were evaluated prior to selecting the final approach involving embedded copper strips.

Method 1: Creation of Holes in the Top Glass Layer
One possible method involved creating openings in the upper glass layer through techniques such as surface sanding, grinding, or using a laser [36]. An additional concept considered the removal of epoxy from a localized region of the glass layer, subsequently filling the hole with a conductive product such as silver paint to establish electrical contact with the underlying carbon layer. Alternatively, small holes could be drilled directly through the glass ply. However, both approaches presented a significant risk of damaging the prepreg material, an outcome that is undesirable for maintaining the mechanical integrity of the composite [34].

Method 2: Connection from the Side
Another investigated approach involved connecting to the carbon layer from the edge of the prepreg. This configuration posed challenges in both manufacturability and measurement reliability. Given that the polymer matrix functions as an electrical insulator (see Section 2.5), such a setup would likely result in measurements dominated by the resistance of individual carbon fibers rather than the bulk layer. Moreover, the small thickness of individual prepreg ply would complicate accurate electrical measurements.

Method 3: Shortening of the Top Glass Layer
A further alternative is fabricating the top glass layer with a shorter in-plane length than the carbon layer, thereby leaving a section of the carbon layer exposed at the prepreg edge, often referred to as a *ply drop*. This technique is comparatively simple, as it avoids direct mechanical alteration of the composite itself. Nevertheless, shortening the glass layer can induce additional interlaminar and edge stresses, which may promote delamination or reduce the overall structural strength of the composite [37] [38].

Method 4: Insertion of a Component Between Layers
A final method considered the insertion of an intermediate component between the glass and carbon layers to facilitate electrical connection with the external measurement system. Two configurations were evaluated: the use of wires and strips. Harikumar et al. [39] embedded copper wires of 5 and 7 mm diameter within GFRP laminates to investigate their mechanical behavior. Their results indicated that wire embedding enhanced delamination resistance as well as tensile and impact strength compared with pure GFRP composites. However, a reduction in flexural strength was observed due to limited adhesion between copper and glass fibers. Similarly, as discussed in Section 2.5, the co-curing of electrodes within CFRP systems has been shown to provide direct good fiber–electrode contact [34].

Conclusion
Based on the discussion above, copper strips integrated between the glass and carbon layers were selected as the final design solution, as illustrated in Figure 3.4. Although introducing this additional element between the prepregs creates a local discontinuity, it was considered acceptable given the necessity of accessing the embedded carbon layer. Copper strips were chosen over wires because they provide a wider contact interface with the carbon ply, thereby improving signal reliability.

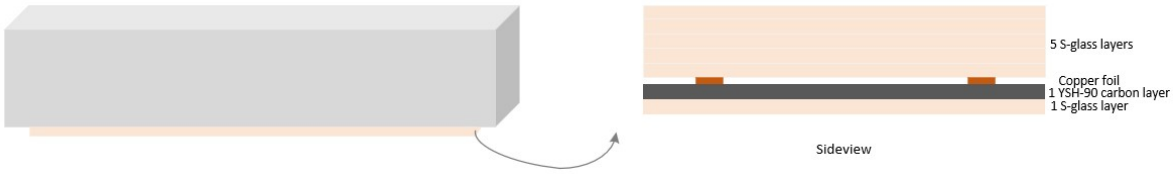

Figure 3.4: Illustration design hybrid mechanochromic FRP with copper foil between glass and carbon layer (not on scale)

3.3.2. Electrical measurements

Electrical measurements on composites can be performed using different methods: two-point probe method, four-point probe method or multi-probe method.
Two-point probe method uses two electrodes to pass current through the specimen. This method is relatively simple since it can be done using a digital Ohmmeter, but is more sensitive to the quality of the electrical contacts.

Next to the resistance of the carbon layer itself, the resistance of the wire, the meter and the imperfect bond needs to be considered. The measured resistance can be approximated as the carbon layer resistance, only if the sum of the last three resistances is small compared to the resistance of the carbon layer. The four-point probe method consists of four electrodes, of which the two inner contacts pass the electrical current and the outer contacts detect the voltage. Resistance will be measured between the inner two probes. Using the four-point probe method, eliminates the contact resistance and any additional resistance, such as the wire resistance. This is useful for measuring very low resistance values or high contact resistance cases.
Finally, the Multi-Probe electric potential method has high reliability for measurements of low electric resistance changes [30] [34]. The different methods set-ups are shown in Figure 3.5.

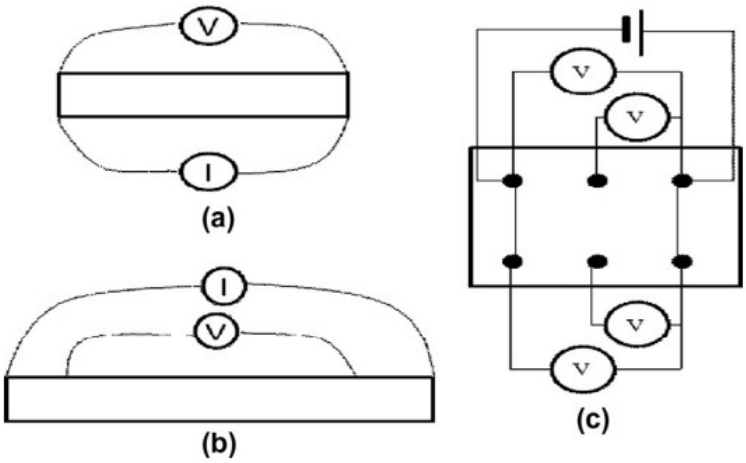

Figure 3.5: Electrical resistance measurement methods: a) Two-Probe Method, (b) Four-Probe Method, and (c) Multi-Probe Method [30]

Using the different connection methods described above, the electrical resistance of the specimen can be determined. The resistance can be calculated using Formula 3.6.

$$R = \frac{U}{I} \tag{3.6}$$

where R is the resistance in Ohm [Ω] , U the voltage in volt [V] and I the current in Ampère [A].

In order to accurately charaterize the measured response, the fractional change in electrical resistance (FCR) can be used, following Formula 3.7.

$$FCR = \frac{R - R_0}{R_0} * 100[\%] \tag{3.7}$$

Where R is the resistance at any time during the test and R_0 is the initial resistance of the specimen prior to the test.

The sensitivity of the measurement device can be expressed as the FCR related to strain. This is called Gauge Factor (GF), which defines the ratio of fractional change in electrical resistance to the strain, shown in Formula 3.8.

$$GF = \frac{\Delta R}{R_{0\epsilon}} \tag{3.8}$$

3.4. FRP Sample Testing

As discussed in Section 3.3.2, several options were considered to establish a connection between the embedded carbon layer and the electrical device. Ultimately, copper strips integrated between the glass and carbon prepregs were selected as the final design. Prior to retrofitting the concrete, four composite samples were fabricated to verify the manufacturing process and to perform preliminary electrical measurements, in order to confirm that this method is feasible.

3.4.1. Sample Manufacturing

The composite specimens measured 100 × 300 mm and were manufactured on an aluminium plate. The plate was first cleaned with ethanol, after which a peel ply was placed on top. The peel ply, as the name suggests, facilitates the removal of the ply from the composite and the plate. Subsequently, five layers of glass fiber, one layer of carbon fiber, and one additional glass layer were laid up in sequence. Four copper strips with a thickness of 0.05 mm were positioned on top of the carbon layer using a thin layer of BARE electric paint. This paint was applied to optimize the electrical bonding between the copper strips and the carbon prepreg, as also demonstrated by Irving et al. [40]. The copper strips were made longer than the width of the prepreg on both sides to ensure sufficient space for connection to the electrical device. In addition, if one side of a strip were to fail, which happened in some cases, the opposite side could still be used. Images of the manufacturing can be found in Appendix B.1.
After every three layers, the specimens were debulked under a pressure of 1 bar to remove any trapped air between the layers. Finally, an additional release foil and aluminium plate were placed on top to achieve a smooth surface finish. A vacuum bag was then prepared and tested to confirm the absence of leaks. The specimens were cured in an oven at 125 °C for one hour, in accordance with the technical datasheet of the epoxy system HexPly® 913, while maintaining continuous vacuum. After curing, the specimens were removed from the oven and cooled to room temperature.
During the first manufacturing trials, it was observed that the orange release foil used, was not suitable for this process, as it adhered to the specimen surface, even though it was rated for the curing temperature. Additionally, the aluminium plate on top of the laminate bonded slightly to the composite, making demoulding difficult. In subsequent trials, an additional layer of peel ply was applied on top of the laminate. This modification successfully prevented adhesion and allowed for easier removal of the specimens after curing. Furthermore, in later iterations, the copper strips were positioned beneath the carbon prepreg to ensure that the mechanochromic effect remained visible.

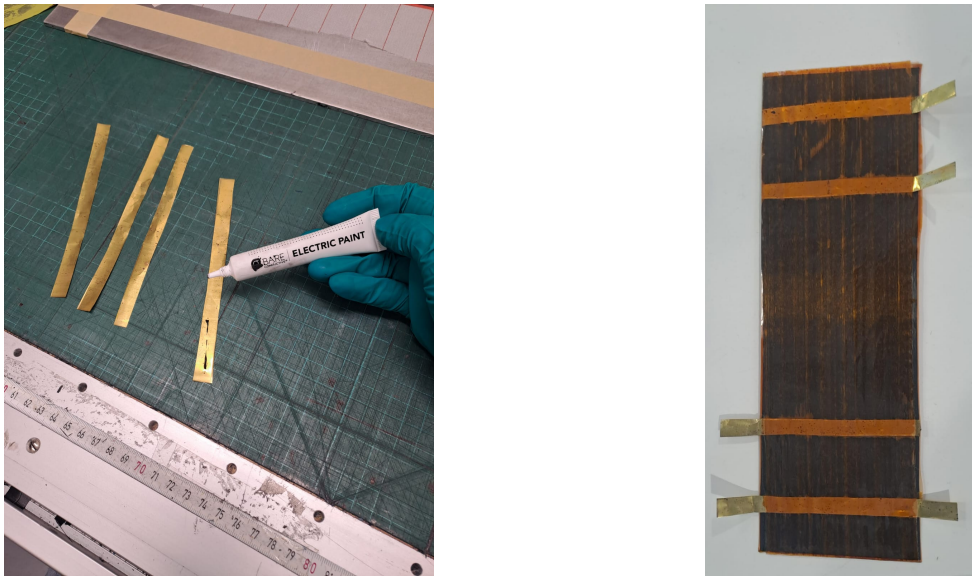

(a) (b)

Figure 3.6: a) Adding electrical paint on the side which touches the CFRP b) Endproduct after first trial manufacturing

3.4.2. Sample Testing

After manufacturing, the first specimens were tested using the four-point probe method under both static and bending conditions. The electrical measurements were performed using a Rohde and Schwarz NGU401 Source Measure Unit, set to operate between –6 V and +6 V with a current limit of 100 mA. The static measurements showed a relatively low resistance between 0.4 and 0.5 Ω. Similar measurements performed during bending revealed an increase in resistance, as expected, although fluctuations prevented determination of a single stable value while bending.
Additionally, two-point probe measurements between different copper strips were performed using a multimeter. These measurements yielded resistances between 2 and 3 Ω, indicating that the accuracy of the multimeter is not as good as performing a four-point probe method. Therefore, the use of four-point probe measurements enables accurate determination of the resistance of the carbon layer itself, eliminating the influence of contact resistance or wire resistance as mentioned in Section 3.3.2.
Furthermore, measurements showed that testing on opposite sides of the copper strips or on the same side resulted in a difference of several milli Ohms, indicating that conductivity along both the length and width of the strip was sufficient for reliable testing. Next to this, the measured heat dissipation was approximately 4 mW, which is considered low enough to assume that thermal effects on the electrical measurements can be neglected.

These preliminary tests were considered sufficient to apply this method in combination with concrete. The use of copper strips provided reliable resistance measurements with stable electrical connections, while allowing the prepregs to remain intact.

3.5. Four-point bending and measuring techniques

3.5.1. Four - point bending test

The flexural FRP retrofitted concrete beams are tested by performing a four-point bending test. A four-point bending test is chosen since this creates a region of constant bending moment, where a fully developed crack pattern can be established. The hydraulic press with a capacity of 100 kN applies a load on a box spreader beam. This box spreader divides the load into two equal loads (F/2). The loading surface of this box spreader is connected to the beam using two loading plates on both sides. On one side, the loading plates are considered fixed, as they are welded together. On the other side, the loading plates can slide over each other, forming a free hinge. This is illustrated in Figure 3.7b. The tests are executed in displacement-controlled with a speed of 0.005 mm/s.

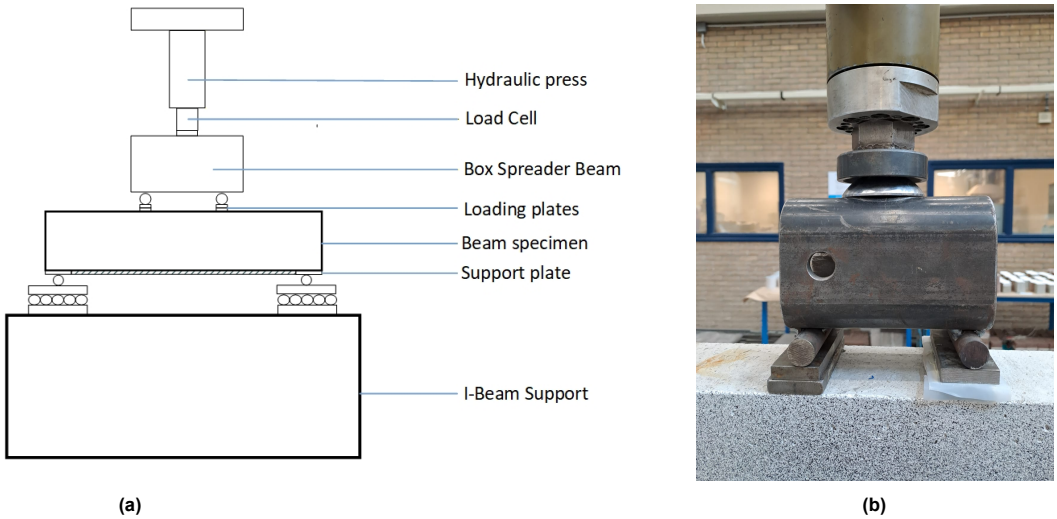

Figure 3.7: Four-point bending test: (a) Loading set-up schematic, (b) Close-up of box spreader and loading plates; the left plate is fixed, and the right plate is a free hinge

The effective span is 360 mm with an equal distance between the loads, shown in Figure 3.8. The FRP retrofitting is applied along a 320 mm span on the bottom surface of each beam, ensuring that sufficient space is left near the supports to prevent any direct contact between the supports and the FRP layer. Additional metal plates are used with a width of 3.5 mm to place the beam on the supports. Both supporting conditions using sliding hinges with limited horizontal movement. This setup is selected to achieve a uniform stress distribution and to establish pure bending conditions.

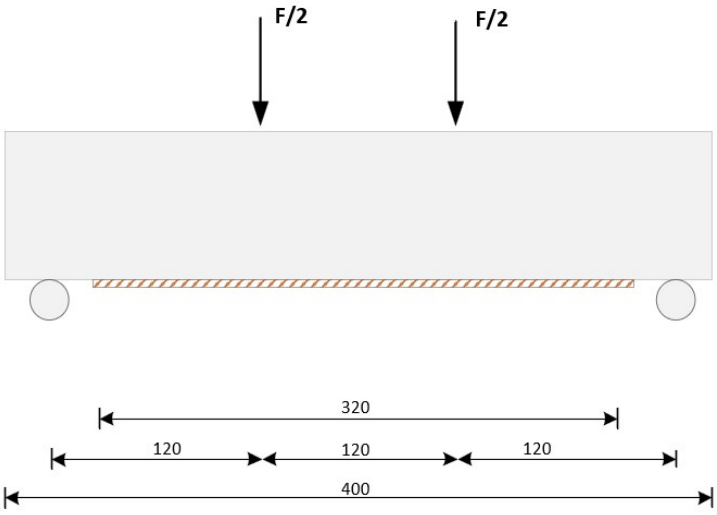

Figure 3.8: Model four-point bending test including FRP

3.5.2. Digital Image Correlation

Digital Image Correlation (DIC) is used to obtain deflections, strains, and crack widths in both two-dimensional and three-dimensional analyses. Consecutive images are compared to determine the relative displacement between the deformed and undeformed states. The displacement vectors of corresponding points in the images are then used to calculate the normal strain, shear strain, and von Mises strain fields. DIC is often employed as a quantitative technique for detecting and monitoring the occurrence and propagation of cracks [41].

Each specimen is first coated with two layers of white paint to form a uniform base layer. Subsequently, a stochastic black speckle pattern was applied using a spray gun on one side of the specimens, covering the entire length and height of the beam, shown in Figure 3.9. During testing, images were captured using a 50 MP Canon 5D camera with a 50 mm lens and ISO 100 setting. The accuracy of the measurements depends strongly on lighting conditions. Therefore, a flash was used for each image to ensure consistent illumination. However, due to reflections from surrounding steel components, images could only be recorded at intervals of five seconds.

Figure 3.9: Stochtastic pattern applied over the full length of the beam

The DIC software *Zeiss Correlate* is used to compare the speckle patterns at different loading stages and to compute the displacement, strain, and deformation fields. A facet size of 19 pixels and point distance of 12 are used. Prior to each test, the quality of the applied speckle pattern is verified in *Zeiss Correlate*, as shown in Figure 3.10a, and adjustments were made when necessary. A mean value above 5 is accepted for these experiments. In addition, two images were captured before the start of each test to perform a noise analysis, with the maximum measured displacement used to assess the background noise level, shown in Figure 3.10b. It can be seen that the difference in displacement is below 0.013 mm, which is considered to be acceptable for all beams.

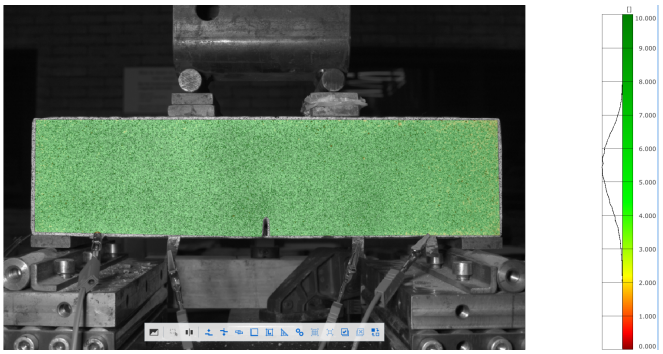

(a) Check pattern quality

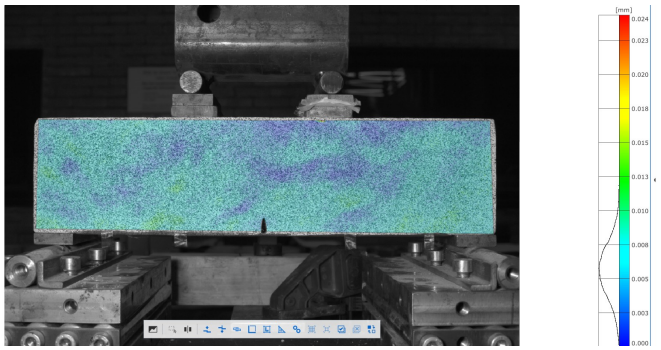

(b) Noise analysis prior to the test

Figure 3.10: Overview of DIC preparation: (a) check pattern quality and (b) noise analysis prior to testing.

3.5.3. Linear Variable Differential Transformer (LVDT)

In addition to DIC, a LVDT is used to measure linear displacements. The linear movement of an object is converted into a corresponding electrical signal that varies proportionally with the object's displacement. The measurement range of LVDTs can vary widely, from 0–0.5 mm up to 0–1000 mm, depending on the specific model and application [42].

In this research, one LVDT is mounted on the backside of the beam near the bottom surface, as shown in Figure 3.11. In this configuration, the strain measured by the LVDT is assumed to represent the strain within the FRP, under the assumption of perfect bonding between the FRP and the concrete, and considering that the FRP thickness is negligible compared to the overall beam height. For this setup, two aluminium blocks are fixed to the beam using Permacol epoxy adhesive, with an end-to-end distance of 200 mm (L_0). A steel rod is placed in one of the aluminium holders, while the LVDT sensor is mounted in the opposite holder and mechanically connected to the rod to accurately record the relative displacement between the two points.

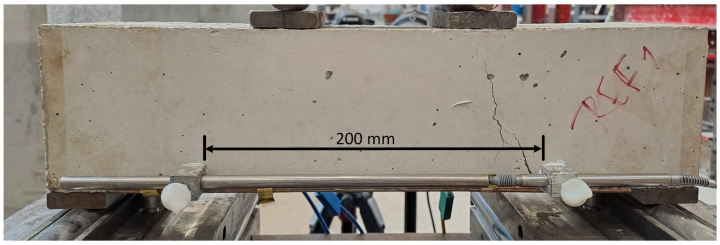

Figure 3.11: LVDT set-up on specimen

Prior to testing, the LVDT was zeroed to eliminate any initial offset. The displacement measured by the LVDT can then be converted to strain in the direction of the displacement using Equation 3.9.

$$\epsilon = \frac{\Delta L_{LVDT}}{L_0} \tag{3.9}$$

where ϵ is the strain in the direction of the LVDT, ΔL_{LVDT} is the change in length measured by the LVDT, and L_0 is the initial length between the LVDT holders.

3.6. Iteration 1

3.6.1. Manufacturing retrofitted concrete

After the manufacturing the FRP sample with copper strips, the retrofitted concrete specimens were manufactured using a similar procedure, shown in Figure 3.12. First, the concrete surface was cleaned and sanded with coarse sandpaper to create a rough texture, improving adhesion with the prepreg layers. The prepregs were then stacked sequentially onto the concrete surface. As in the previous manufacturing process, the specimens were debulked after every three plies to remove trapped air between the layers and to improve the bonding between the composite and the concrete. After the fifth glass layer, copper strips were positioned using a thin layer of conductive paint on top to ensure good electrical contact with the carbon prepreg. Once all layers were stacked, the specimens were individually sealed in vacuum bags. Each vacuum bag was leak-tested before placing the samples in the oven.
The first two samples were cured at 125 °C for one hour, according to the datasheet of the HexPly® 913 epoxy system. However, after curing, it was observed that the epoxy had not fully hardened. A possible explanation is that the concrete beam acted as a heat sink, slowing down the temperature rise in the composite. Consequently, the resin on top could not reach the required curing temperature. Based on the recommendation of the laboratory technician, the curing time was extended to allow the concrete to reach thermal equilibrium. The following two specimens were therefore cured at 125 °C for one hour and 45 minutes, after which full curing of the epoxy was achieved. The remaining seven specimens were manufactured using the same extended curing procedure.

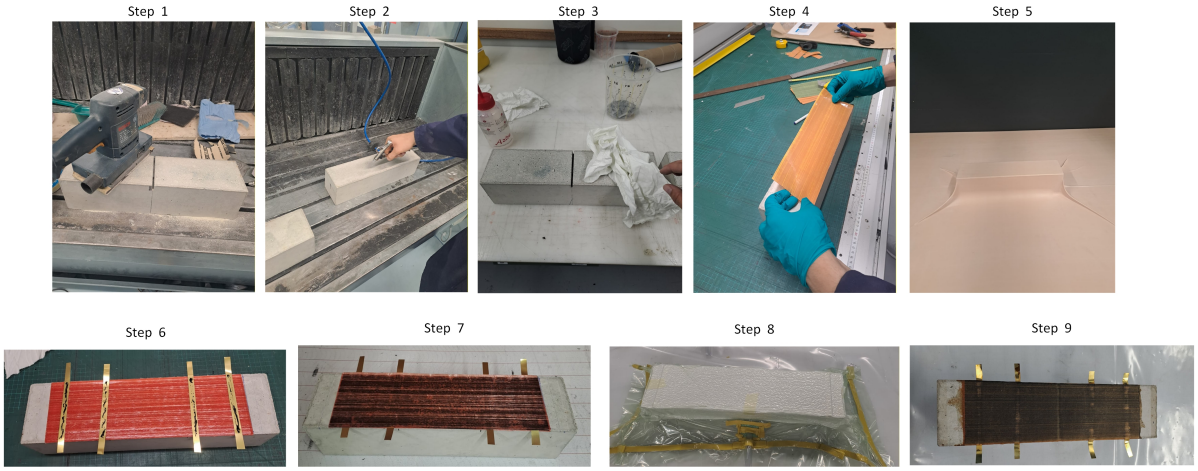

Figure 3.12: Step 1: Using a sander with high roughness sandpaper to create a rough surface, Step 2: Using an air gun to remove dust particles, Step 3: Cleaning the concrete surface using isopropyleen, Step 4: Applying prepreg layers on marked area, Step 5: Debulking at 1 bar after every three layers, Step 6: Applying copper strips with black conductive paint, Step 7: Add final carbon and glass layer, Step 8: Apply peelply and breather material on top of the composite and prepare a vacuumbag and seal the beam, Step 9: Take specimen out of the oven and let it cool down.

3.6.2. Electrical set-up Iteration 1

In Iteration 1, nine samples were tested using the four-point probe method. Four conductive strips were embedded below the carbon layer, allowing the mechanochromic effect of this layer to remain visible. The placement of the electrodes was inspired by Liu et al., whose configuration of conductive strips is shown in Figures 3.13 and 3.14 [43]. Similarly, Wang et al. [30] used silver paint electrodes to measure resistance in CFRP specimens, employing an inner probe spacing of 60 mm and an outer probe spacing of 78 mm. It is important to maintain sufficient spacing between the inner probes, as well as between the inner and outer probes, to ensure uniform current density across the voltage contacts [44].

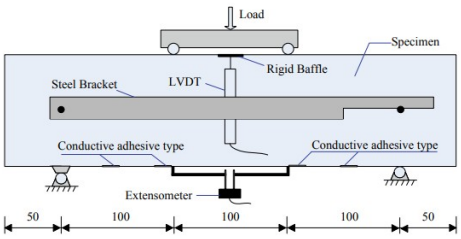

Figure 3.13: Experimental setup by Liu et al. [43]

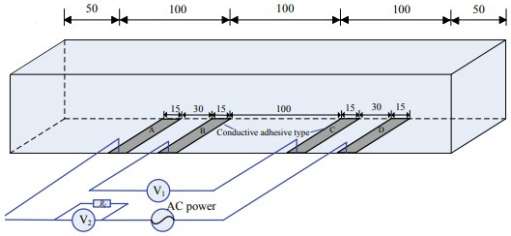

Figure 3.14: Sample configuration for measuring resistance by Liu et al. [43]

In the present study, the outer electrodes were positioned at a distance of 2 mm from the edges of the FRP specimens to avoid introducing discontinuities. The spacing of the inner probes was selected based on the region of the concrete beam expected to experience the highest bending moment. The inner electrodes were placed just outside this critical area to accurately capture resistance changes corresponding to maximum bending stress, following the approach of Liu et al. [43]. A width of 1 mm was used for the electrodes. The final placement configuration of the copper strips beneath the carbon prepreg is shown in Figure 3.15.

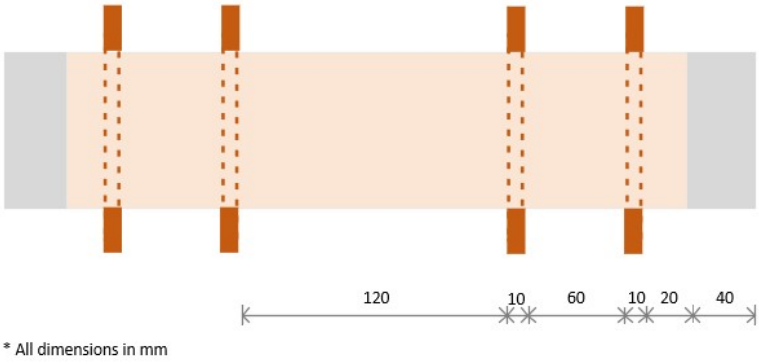

Figure 3.15: Iteration 1: Topview, configuration of strips

3.6.3. Test set-up

The electrical device used is the Rohde Schwarz NGU401, with similar settings when testing the samples. Four cables with alligator clips are used to connect the device with the copper strips. The complete set-up of the testing is shown in Figure 3.16.

Figure 3.16: Test set-up Iteration 1

3.7. Iteration 2

After evaluating the results of Iteration 1, it was decided to perform additional experiments, referred to as Iteration 2. The main reason for this, was the lack of mechanochromic effects after testing and the poor bonding between concrete and composite which influenced the electrical resistance measurements. Due to the time required to execute these experiments and the time limitations of this research, only three additional beams were manufactured and tested. Based on the outcomes of Iteration 1, the manufacturing process and the electrical method were modified, which will be discussed in the following sections.

3.7.1. Manufacturing retrofitted concrete

In Iteration 2, three specimens were manufactured. Based on the results of the first tests, it was recommended to adopt a different manufacturing approach. For Iteration 2, the same method as described by Mohammadi et al. [10], utilizing an autoclave, was employed. The primary reasons the autoclave was not used in Iteration 1 were practical considerations and the desire to maintain a process closer to real-life application conditions.

In addition to the change in curing process, two other modifications were made in Iteration 2. Firstly, two copper strips were used instead of four, which will be explained in Section 3.7.2. Secondly, no conductive paint was applied between the carbon layer and the copper strips. Based on the results, which will be discussed in Chapter 4, this modification is considered to be a more effective approach. The other steps of the manufacturing process remained unchanged.

An autoclave was used for the curing process, shown in Figure 3.17. In addition to heat, this machine provides applied pressure. According to the datasheet, a pressure of seven bar was applied. The exact curing procedure followed that of Mohammadi et al. [10], and further details are provided in Appendix B.2.

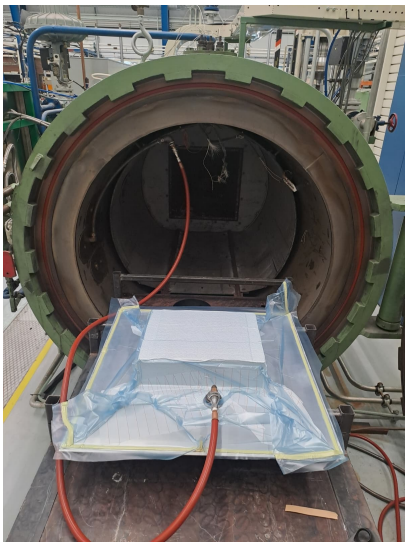

Figure 3.17: Autoclave curing

3.7.2. Electrical set-up

In Iteration 2, a different electrical set-up is used to achieve higher measurement accuracy. In Iteration 1, the resistance measurements recorded, were in the order of milli-ohms, which was close to the accuracy limit of the equipment. This made it challenging to detect small changes in resistance and resulted in relatively noisy measurements. To measure very small changes in resistance, strain gauges often use a bridge configuration. In this case, a Wheatstone Bridge is employed, as shown in Figure 3.18. When one known resistor in the Wheatstone Bridge is replaced by a strain gauge, the configuration is referred to as a Quarter Bridge Circuit, shown in Figure 3.19 [45]. Since the resistance of three resistors and total voltage of the bridge circuit is known. A change in resistance and thus voltage can be related to the strain gauge.

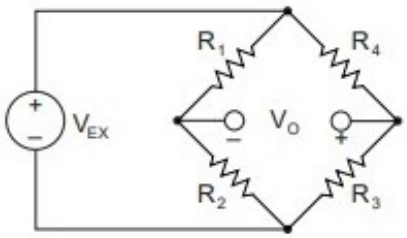

Figure 3.18: Wheatstone Bridge

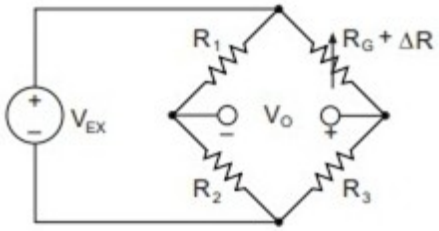

Figure 3.19: Quarter Bridge Circuit

For Iteration 2, one resistance in the Quarter-Bridge Circuit is replaced by the resistance of the carbon layer. The other three resistors in the bridge have a resistance of 350 Ohm with an accuracy of 0.01%. A bridge current of 6V is used with an amplifier of 1000. During the test, the relative change in current is measured. Prior to testing, the measurements are zerood in order to take measurements from a range from -10V to 10V. In order to go from the relative change in current to the relative change in resistance, the following formulas can be used.

The nominal current through the Wheatstone bridge branch is given by:

$$I = \frac{V_{\text{ex}}}{R_1 + R_3 + R_0} \tag{3.10}$$

The resulting output voltage due to a change in resistance of the carbon layer can be expressed as:

$$U_u = \Delta R_g \cdot I \tag{3.11}$$

where:

- R_0 = initial resistance of the carbon layer [Ω],
- I = current through the carbon layer [A],
- V_{ex} = excitation voltage of the bridge = 6 [V],
- R_1, R_3 = fixed resistances in the bridge = 350 [Ω],
- U_u = output voltage of the bridge [V],
- ΔR_g = relative resistance change [Ω].

For this method, only two probes are required. Consequently, only two copper strips are used for the next three specimens. Using an electrode configuration with an inner distance of 260 mm, shown in Figure 3.20. The wires from the measurement device are connected to the copper strips via soldered connections to minimize additional contact resistance. An additional benefit of this method is that the area over which the electrical resistance is measured becomes larger.

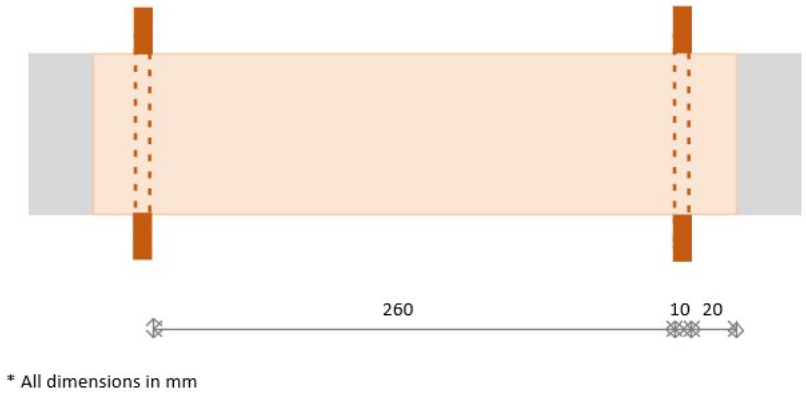

Figure 3.20: Iteration 2: Topview, configuration of strips

3.7.3. Test set-up

Some modifications were made in Iteration 2 of the experiments. As mentioned in Section 3.7.2, the electrical setup was different. Instead of using alligator clips, a soldered connection was made. In addition, a laser setup was used to more accurately measure the specimen's deflection during loading. A 3D-printed plate was also fabricated to allow the specimen to be recorded from below, enabling observation of any color changes during the experiment. To ensure a sharp video, an additional light source was placed beneath the specimen to improve camera focus. The set-up can be seen in Figures 3.21, 3.22a and 3.22b.

Figure 3.21: Test set-up Iteration 2

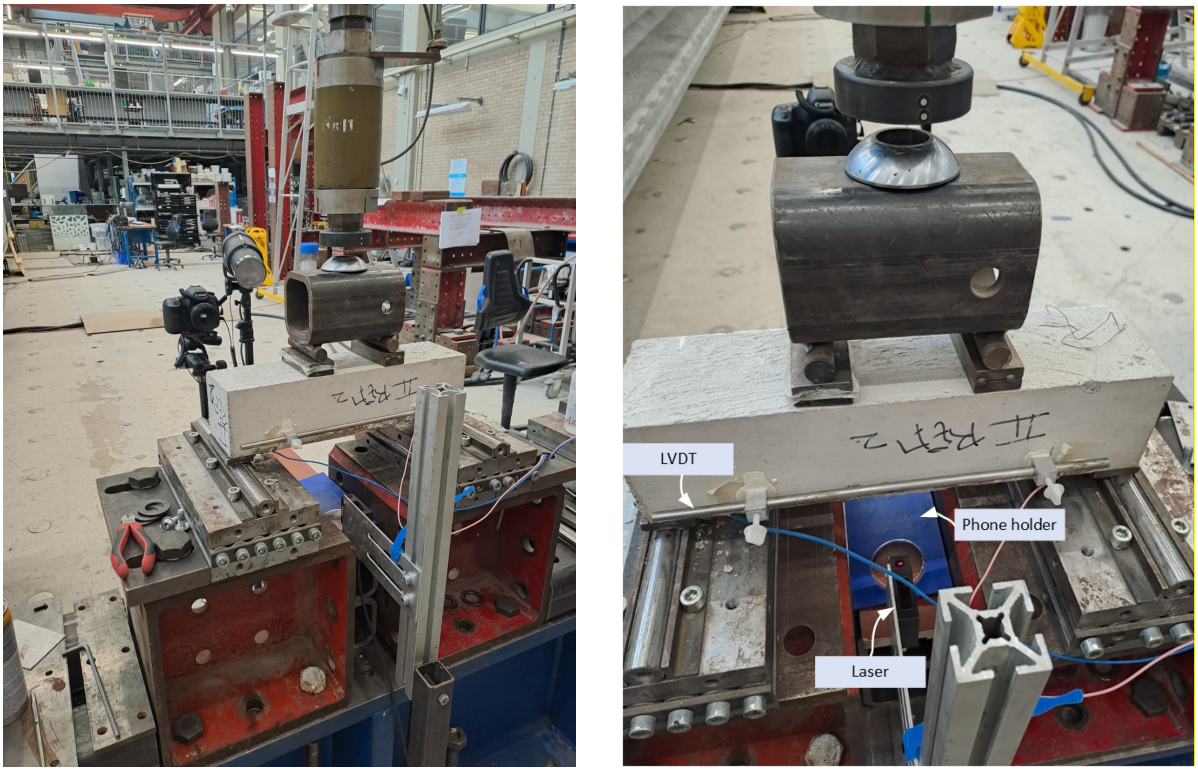

(a) Backside test set-up

(b) Backside test set-up close-up

Figure 3.22: Iteration 2 test set-up backside

After testing the first beam, 2-REF2, a failure near the supports was observed, with no noticeable color change effect. To aim for a higher ultimate load and potentially induce a color change, the support plates were glued to the concrete specimen in 2-REF1, preventing any relative movement between the concrete beam and the plate, as shown in Figure 3.23a. The support plate remained free to move on the rolling hinges, so the overall support conditions were unchanged. Despite this modification, a similar failure mechanism occurred with the glued plate.

For specimen 2-REF3, the support plates were glued to the concrete beam with partial overlap onto the composite surface, as shown in Figure 3.23b. Specifically, 3 mm of the plate rested on the composite, while 1 mm rested on the concrete. Due to this arrangement, the supports for 2-REF3 had to be positioned closer together, reducing the effective span to 30 mm from the initial 36 mm. Consequently, the box spreader now applies pressure over a 10 mm distance to maintain the same proportion of 10 mm on each side. An overview of the different plate conditions is presented in Table 3.3.

Specimen	Support plate
2-REF1	glued
2-REF2	not glued
2-REF3	glued with 3 mm overlap

Table 3.3: Specimen list

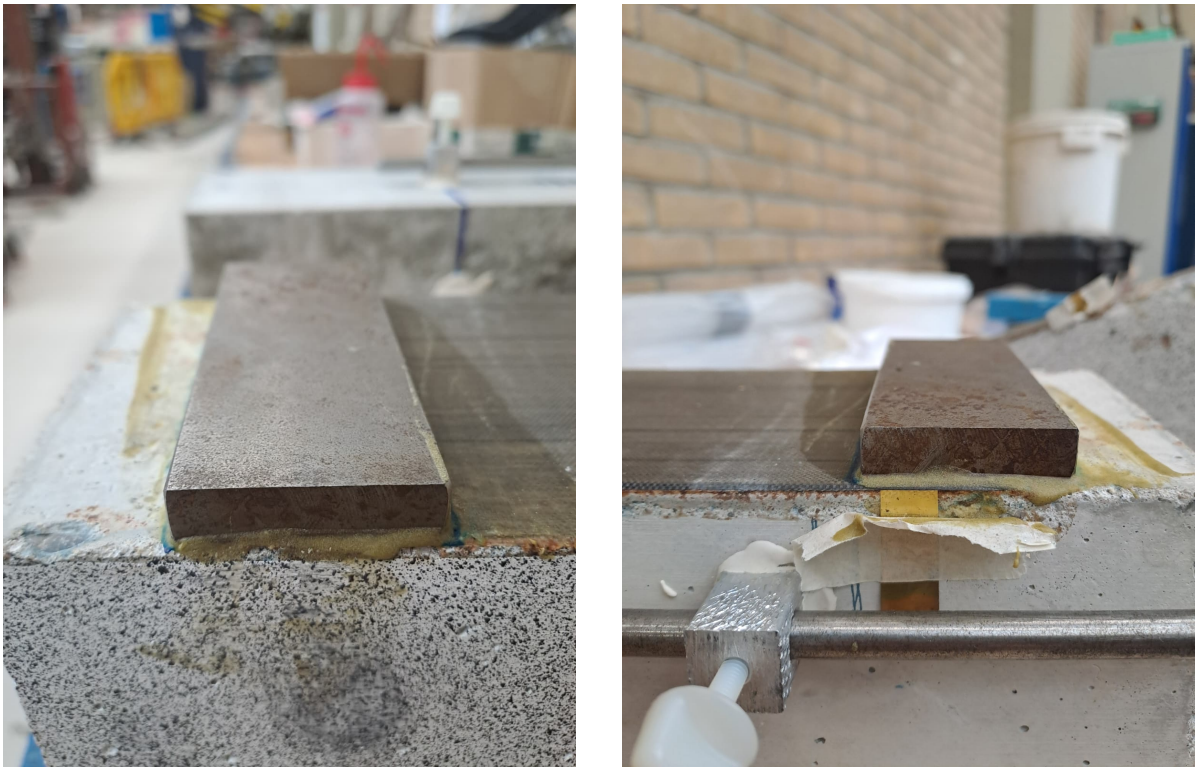

(a) (b)

Figure 3.23: (a) Specimen 2-REF1: glued support plates at the edge of the composite (b) Specimen 2-REF3: glued support plates with overlap to the composite

4 Results

This chapter presents the results obtained before, during and after the four-point bending tests for Iteration 1 and Iteration 2. First, Iteration 1 will be presented using different graphs to show the relation between mechanical and electrical response. Later, Iteration 2 will be discussed, including a short comparison between the two different iterations. In the end, the outcome of Iteration 2 will be the main focus of this study.

4.1. Iteration 1

4.1.1. Pre-testing: Qualitative Results

After manufacturing the retrofitted specimens, as described in Section 3.6.1, each specimen is carefully inspected. During inspection, hollow sounds were detected when tapping on the composite surfaces, with the intensity of sound varying among specimens. These sounds were accompanied by uneven surface profiles, particularly in the areas between the inner and outer strips. The occurrence of hollow sounds and surface irregularities may indicate bonding issues between the concrete substrate and the composite layer. In addition, visible stripes corresponding to the copper strips were observed after curing. The degree of visibility differed between specimens. More orange-colored speckles were also noted, likely originating from the glass prepregs. Although the copper strips were placed beneath the black carbon prepregs, their visibility, along with the orange speckles, suggests that the carbon fibers may have opened locally, exposing the underlying materials. Figure 4.1 presents three specimens to illustrate the differences in copper strip visibility.

Figure 4.1: Three specimens after curing with different visibility in color stripes

4.1.2. Initial Resistance Measurements

Before each four-point bending test, the initial resistance (R_0) of each specimen is measured using the four-point probe method to determine the change in resistance during the testing. This measurement is performed under static conditions, with no load applied. As shown in Table 4.1, the initial resistance values vary between 0.268 Ω and 0.453 Ω. Variations in R_0 can be attributed to differences in the number of contacting carbon fibers and minor variations in the electrode spacing. It can be observed that specimen REF2 exhibits a significantly higher initial resistance compared to the other beams. Therefore, the standard deviation (STD) and the coefficient of variation (CV) were recalculated excluding REF2, resulting in lower values for the STD and CV.

Group	Specimen	R_0 [Ω]
REF	1	0.279079
	2	0.452817
	3	0.315452
RLD	1	0.267888
	2	0.302812
	3	0.320624
RHD	1	0.274792
	2	0.291004
	3	0.291562
Mean - All groups		0.3106
STD - All groups		0.0562
CV - All groups		18.09%
STD - without REF2		0.0190
CV - without REF2		6.49%

Table 4.1: Initial electrical resistance R_0 prior to testing

The elevated initial resistance of REF 2 is likely related to variations in the prepreg material, which may contain minor initial defects. Directly after curing, REF 2 exhibited visible indentations, as shown in Figure 4.2. These indentations can contribute to the higher measured resistance. In no other sample, these kind of identations were observed.

Figure 4.2: Indentations in REF 2 sample after curing

The obtained initial resistance measurements can be compared with the theoretical value calculated using Formula 2.1. For this calculation, the electrical resistivity of the carbon fibers is taken from the datasheet, giving a value of $\rho = 3 \times 10^{-3}\,\Omega \cdot \text{mm}$. The distance between the inner electrodes is $L = 120\,\text{mm}$, and the cross-sectional area A is determined from the thickness and width of the specimen, with $t = 0.01\,\text{mm}$ and $w = 100\,\text{mm}$. Using these parameters, the theoretical resistance of the CFRP sample can be estimated, giving $R_{\text{theoretical}} = 0.36\,\Omega$. It can be seen that this theoretical resistance is of the same order of magnitude as the experimentally obtained values. This formula assumes zero interface resistance and a uniform current distribution between the electrodes, without any spreading resistance [34]. Differences in the measured resistance can arise from misalignment of the electrode spacing or variations in the specimen thickness. The thickness of the carbon layer is determined on an uncured specimen, but in practice, or once cured, it may differ from the assumed value.

4.1.3. Overview of Mechanical and Electrical Behaviour

For each test, the mechanical and electrical properties were determined, as summarized in Table 4.2. It can be observed that the highest ultimate force is achieved by the retrofitted specimens with a high damage level (RHD), while only minor differences were found between the undamaged reference specimens (REF) and those with a low damage level (RLD). This trend is contrary to expectations, as notched specimens typically exhibit stress concentrations that can initiate debonding and consequently lead to lower ultimate loads. Therefore, the REF specimens without a notch were expected to sustain higher ultimate forces. The observed FCR remained below 1.006% for all specimens, corresponding to only a few tenths of an ohm.

Group	Specimen	F_{max} [kN]	Deflection [mm]	Strain at F_{max} [%]	FCR min. [%]	FCR max. [%]
REF	1	13.95	0.287	0.145	0.477	0.650
	2	13.06	0.618	0.217	0.043	1.075
	3	14.23	0.170	0.223	0.412	0.789
	Mean ± STD	*13.75 ± 0.61*	*0.358 ± 0.232*			
RLD	1	15.59	0.582	0.164	0.554	0.722
	2	13.13	0.511	0.130	0.138	0.290
	3	12.66	0.315	0.031	0.400	0.464
	Mean ± STD	*13.79 ± 1.57*	*0.469 ± 0.138*			
RHD	1	19.18	0.634	0.225	0.181	0.559
	2	17.37	0.745	0.271	0.317	0.705
	3	25.77	0.999	0.319	0.536	1.006
	Mean ± STD	*20.77 ± 4.42*	*0.793 ± 0.187*			

Table 4.2: Overview test results Iteration 1

4.1.4. Post-testing: Qualitative Results

Mechanochromic effects

For each specimen, photographs were taken before and after testing, provided in Appendix C. As discussed in Section 2.4.1, a color change in the carbon layer is expected to indicate fiber failure. However, no visible color change was observed after testing. From the strain values reported in Table 4.2, it can be seen that the maximum strains remain below 0.3%, except for specimen RHD 3. The 0.3% strain corresponds to the strain-to-failure limit of the carbon layer provided by the manufacturer's datasheet. Strains below this threshold are expected to cause elastic deformation of the fibers without irreversible fiber breakage. Therefore, the observed changes in electrical resistance are most likely due to elastic strain of the fibers. For specimen RHD 3, an ultimate strain of 0.319% was obtained, which exceeds the strain-to-failure of the carbon fibers, so fiber breakage and a visible color change would be expected.

Failure Modes

Next, the failure mechanism of each specimen was determined using DIC images to identify the crack initiation during testing. Based on these images combined with an inspection after testing and the failure modes described in Section 2.3.3, two main failure modes can be distinguished:

- **Type 1:** Mid-span debonding initiated by a flexural crack.
- **Type 2:** Mid-span debonding initiated by a flexural-shear crack.

The failure modes for each specimen are summarized in Table 4.3. All the images taken after testing are shown in Appendix D.

Figures 4.3 and 4.4 show a Type 1 failure, mid-span debonding initiated by flexural crack, before and after failure of specimen RLD 2. From Figure 4.3b the crack path of the flexural crack can be seen. Figure 4.4b

Group	Specimen	Failure Modes
REF	1	Type 2
	2	Type 1
	3	Type 1
RLD	1	Type 2
	2	Type 1
	3	Type 1
RHD	1	Type 2
	2	Type 1
	3	Type 2

Table 4.3: Overview Failure modes

shows the crack after failure. It can be seen that a debonded region is developed until the tip of the flexural crack.

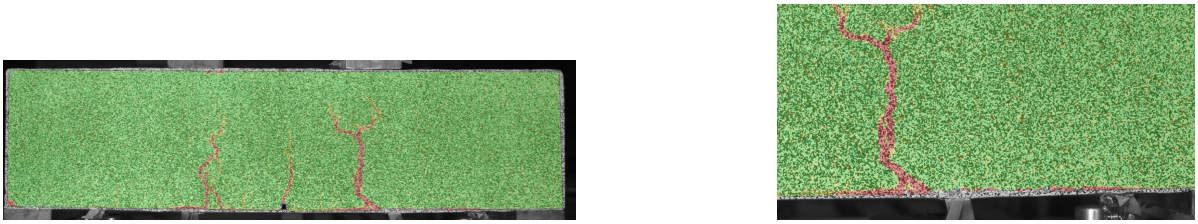

(a) Crack pattern RLD2 **(b)** Close-up main flexural crack

Figure 4.3: Crack region specimen RLD2 before failure

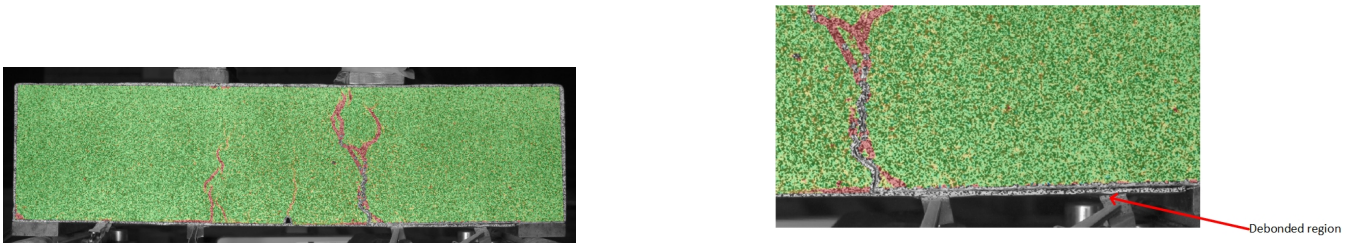

(a) Crack pattern RLD2 **(b)** Close-up cracked zone

Figure 4.4: Crack region 2 specimen RLD2 after failure

Figures 4.5 and 4.6 show a Type 2 failure before and after failure. From the inclination of the crack, it can be seen that it is a flexural combined with shear failure.

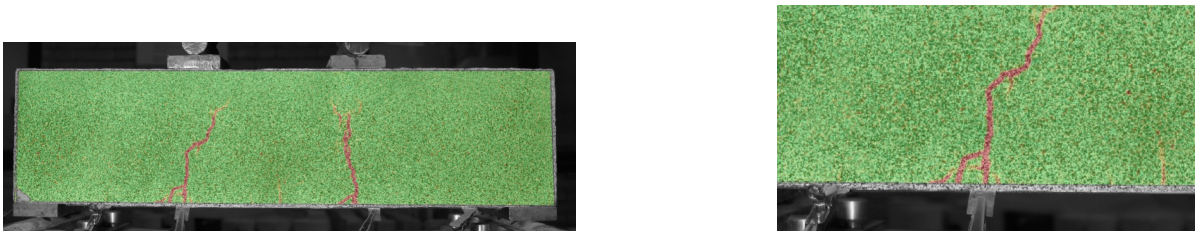

(a) Crack pattern RLD2 **(b)** Close-up main flexural crack

Figure 4.5: Crack region specimen REF1 before failure

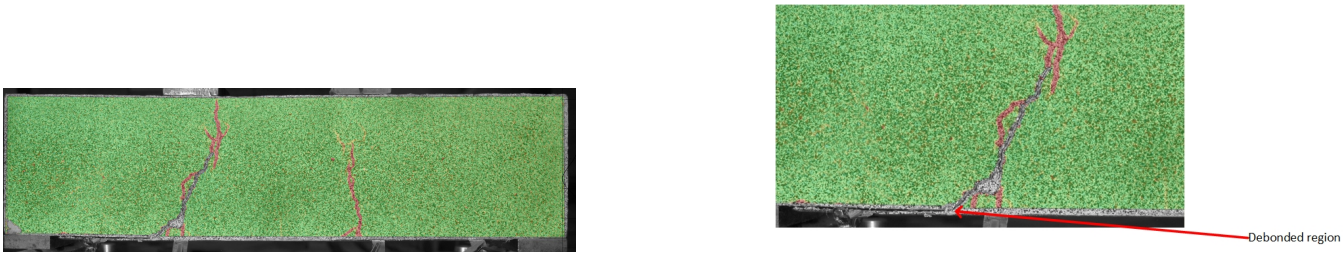

(a) Crack pattern REF1

(b) Close-up cracked zone

Figure 4.6: Crack region 2 specimen REF1 after failure

Bonding

Next, photographs of the cross sections were taken to examine the bonding between the composite and the concrete. In Figures 4.7a and 4.7b, the cross sections of two specimens are shown. Poor bonding can clearly be observed, as the fibers are completely unattached from the concrete. Moreover, air gaps were visible between the concrete and the composite.

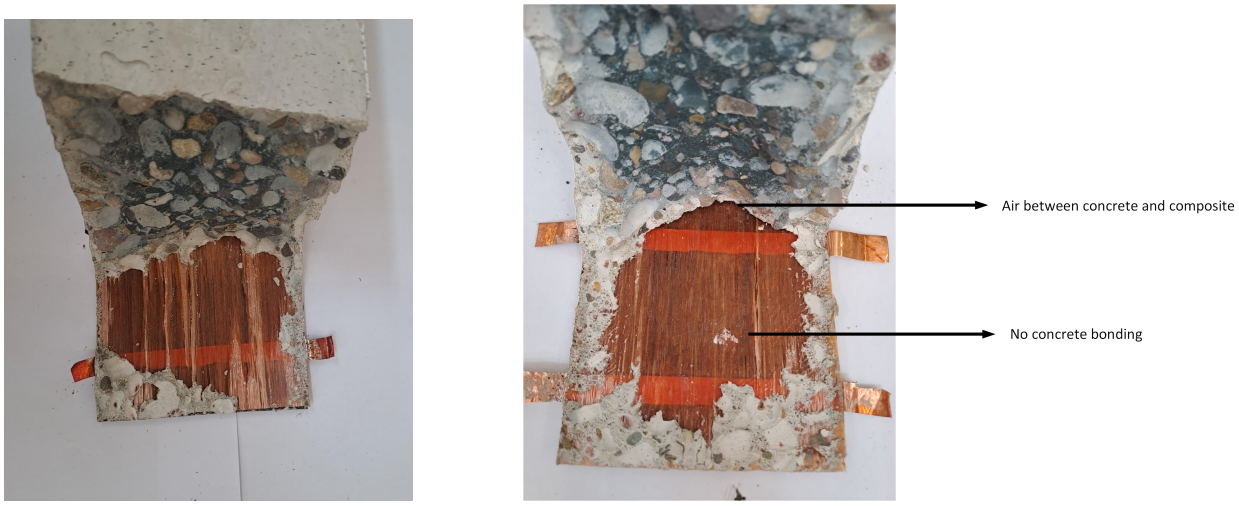

(a) Specimen RHD1 after testing

(b) Specimen RHD3 after testing

Figure 4.7: Bonding behaviour specimens RHD1 and RHD3

4.1.5. Piezoresistive behaviour

The piezoresistive behavior of each specimen is evaluated by plotting the applied load and the FCR against time on separate y-axes. This allows assessment of whether changes in load correspond to increases or decreases in FCR. From Figure 4.8, it can be seen that all specimens, except RLD2, exhibit a positive correlation between load and FCR over time. An increase in FCR corresponds to an increase in the resistance of the carbon layer during testing, whereas a negative correlation indicates a decrease in resistance compared to the previous timestep. Only negative FCR values suggest improved electrical connectivity within the carbon layer, however, this is not obtained. The cause of the negative FCR response in RLD2 will be addressed in the discussion. Different phases can be identified in the graphs, starting with an initial phase, where the FCR fluctuates between one value. This phase is followed by a gradual increase in FCR. The range of FCR values is highly dependent on the specific specimen. No clear correlation can be found between FCR values and loading values. In specimen REF2, a drop in load coincides with a notable FCR increase of approximately 0.7%. To clarify this clear FCR increase, the next section will link these graphs to the Crack Opening Displacement (COD) of the concrete.

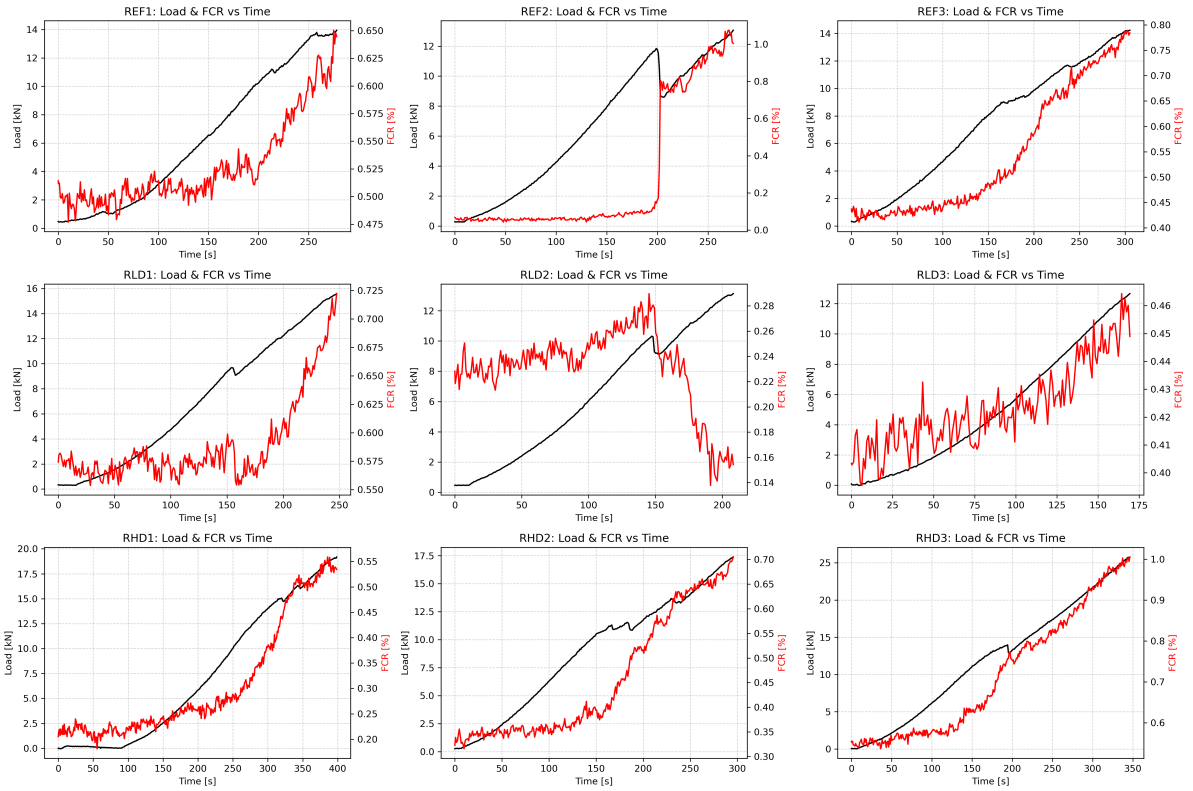

Figure 4.8: Piezoresistive behaviour specimens Iteration 1

4.1.6. Correlation between Load, FCR and COD

In this section, the relationship between Load, FCR, and Crack Opening Displacement (COD) is analyzed in order to link FCR to the development of high strain levels in concrete. These high strain levels can potentially lead to the formation of cracks. COD is determined using DIC with a virtual extensometer, which functions similarly to an LVDT, as described in Section 3.5.3. The COD is measured between the inner copper strips as illustrated with a green arrow in Figure 4.9, following the same method used by Liu et al.[43] for determining the COD.

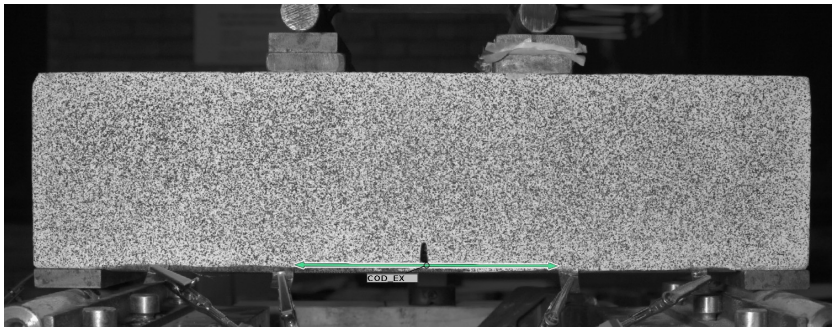

Figure 4.9: Placement virtual COD extensometer between inner electrodes

In addition to plotting Load, FCR, and COD on a single curve, significant time points corresponding to high strain levels are highlighted with vertical lines in the graph. Corresponding DIC images are displayed next to these lines to visually illustrate the development of localized strain concentrations. These DIC images show the major strains over a range from -1% to 1%, considering all the measured strain values of the different photos.

REF - specimens

From the Figures 4.10, 4.11 and 4.12, it can be seen that the start of high strain zones corresponds to the foot of the gradual increase of the FCR curve. Specimen REF 2 experiences a sudden drop in loading which aligns with a clear increase in FCR and major strain. For all specimens, the COD curve aligns with the FCR curve.

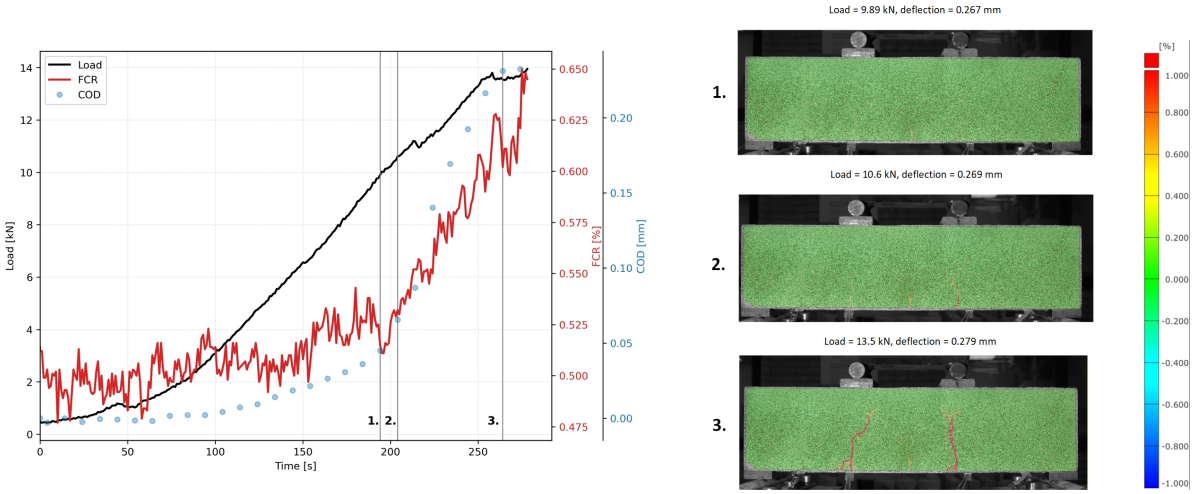

Figure 4.10: REF1: Load, FCR, COD vs Time with DIC images

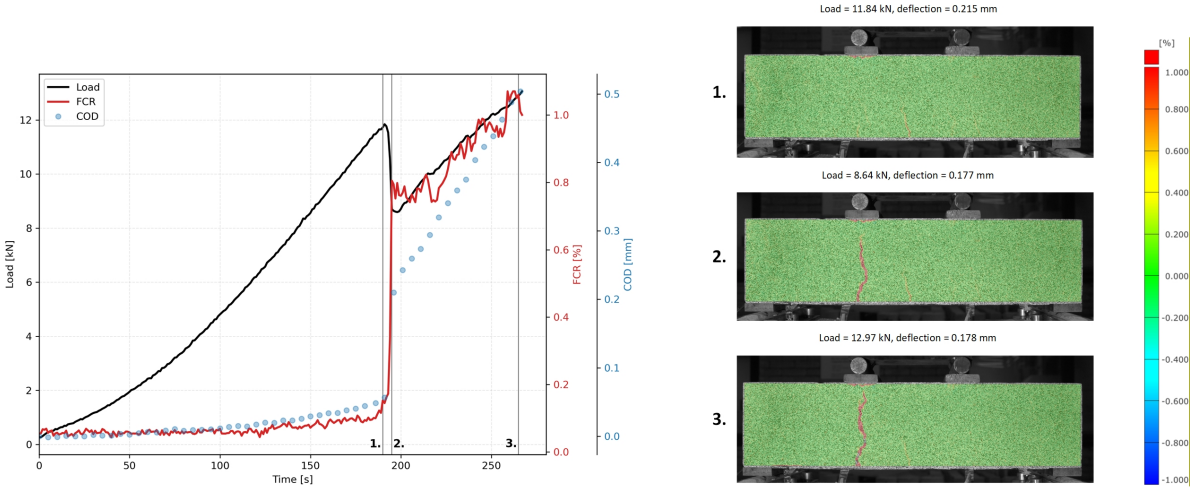

Figure 4.11: REF2: Load, FCR, COD vs Time with DIC images

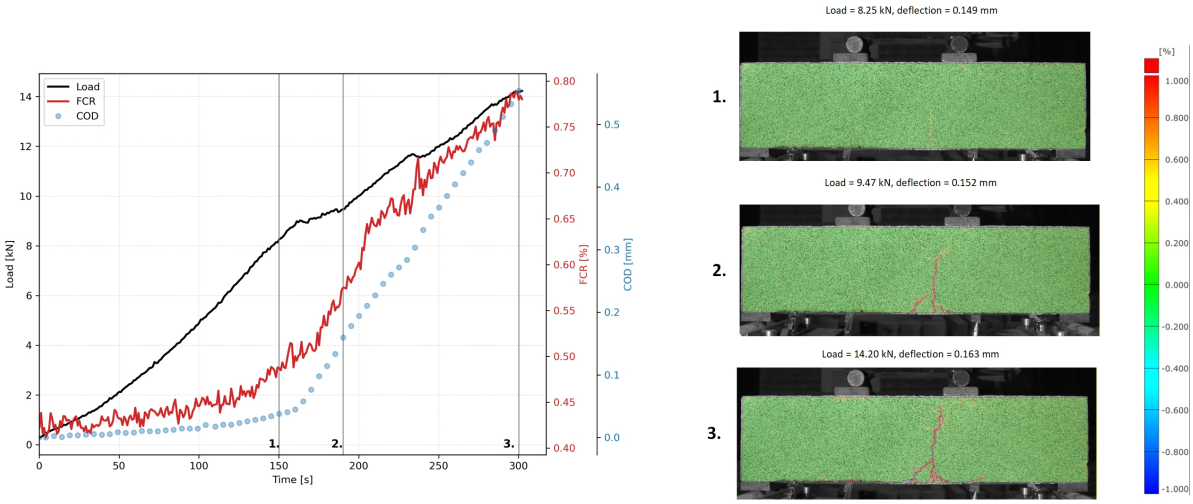

Figure 4.12: REF3: Load, FCR, COD vs Time with DIC images

RLD - specimens

In Figure 4.13, a local drop in load corresponds to a local drop in FCR, coinciding with strain initiation. The initial increase in COD, marking the onset of a visible strain level along a line, aligns with the decrease in both load and FCR. At later stages, however, FCR increases, following the trend of both the COD and load curve. For specimen RLD 2, shown in Figure 4.14, a different pattern is observed. Again, a local drop in load corresponds to a drop in FCR, while COD continues to increase. Subsequently, FCR rises over time, resulting in a negative correlation between FCR and both load and COD. For specimen RLD 3, COD increases gradually with the load. Although the FCR signal is dominated by noise, a slow increasing trend can still be observed. The COD range of 0.01–0.45 mm is relatively small compared to the other specimens. For this specimen, almost no visible strain occurred before complete failure, as shown in the bottom DIC image, where only one strain line corresponds to the final failure crack.

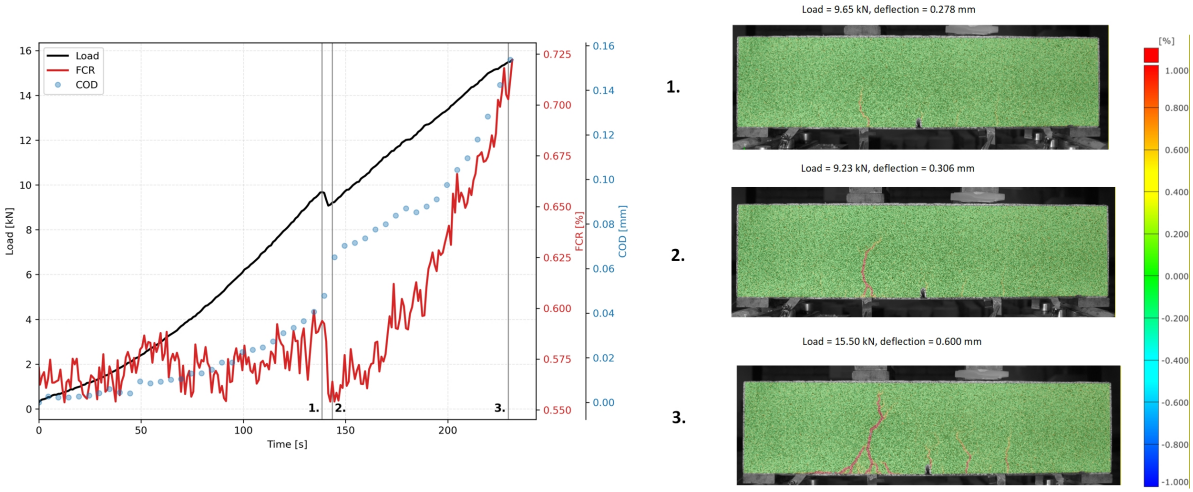

Figure 4.13: RLD1: Load, FCR, COD vs Time with DIC images

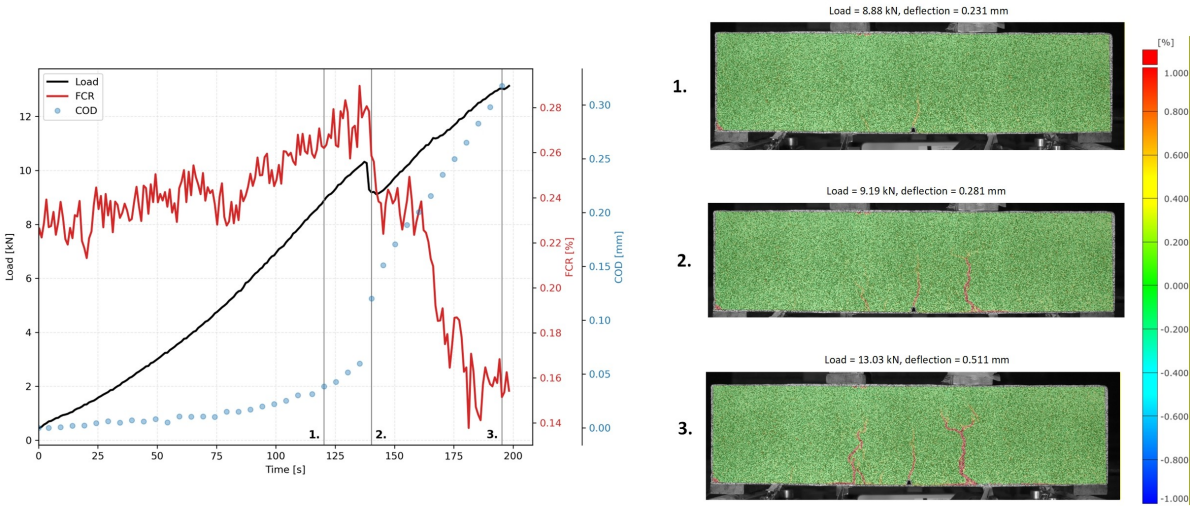

Figure 4.14: RLD2: Load, FCR, COD vs Time with DIC images

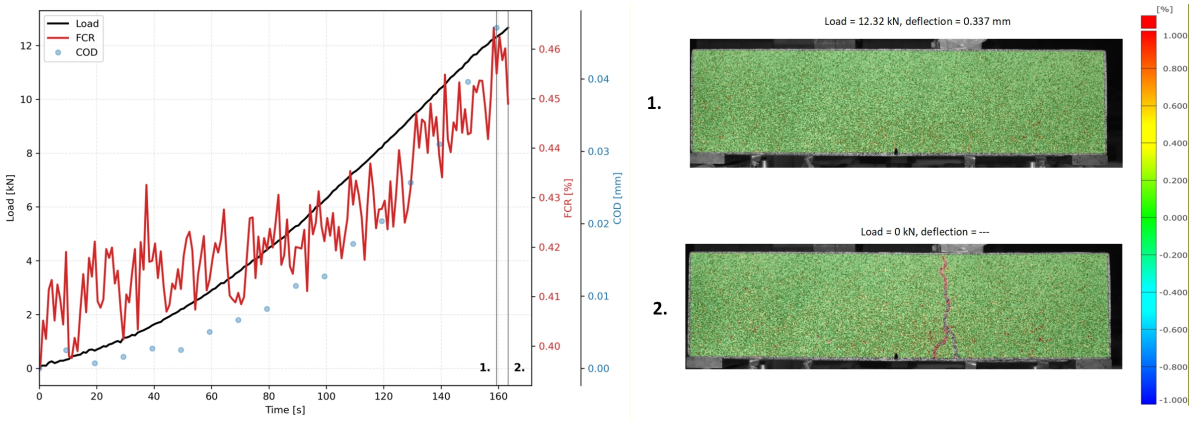

Figure 4.15: RLD3: Load, FCR, COD vs Time with DIC images

RHD - specimens

Specimen RHD1, shown in Figure 4.16, exhibits a gradual increase in FCR. From the initial unstrained stage to the stage where multiple localized strain lines appeared, FCR increased by approximately 0.1%. At later time steps, FCR rises more steeply, while COD increases from 0.1 mm to 0.25 mm. For specimen RHD2, shown in Figure 4.17, the appearance of the first localized strain line coincides with a small peak in FCR and a gradual increase in COD, although no corresponding feature is visible in the Load curve. At later stages, a clear increase in FCR is observed, again following the trend of the COD curve. Small drops in the Load curve are not clearly reflected in the other measurements. Specimen RHD3 failed at the highest load of Stage I. From Figure 4.18, a distinct increase in both FCR and COD is observed starting from t = 160 s, corresponding to the occurrence of the first localized strain line. For all RHD specimens, multiple localized high-strain zones developed prior to failure, including zones originating from the notch. This behavior differs from the other specimen groups, where in most cases a single localized strain line with side branches are observed.

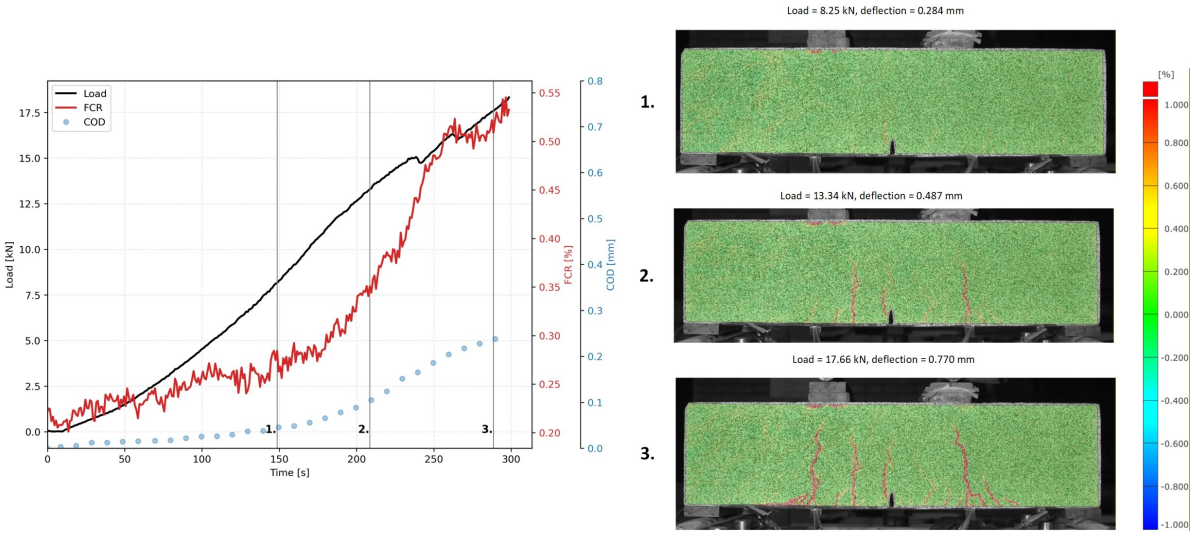

Figure 4.16: RHD1: Load, FCR, COD vs Time with DIC images

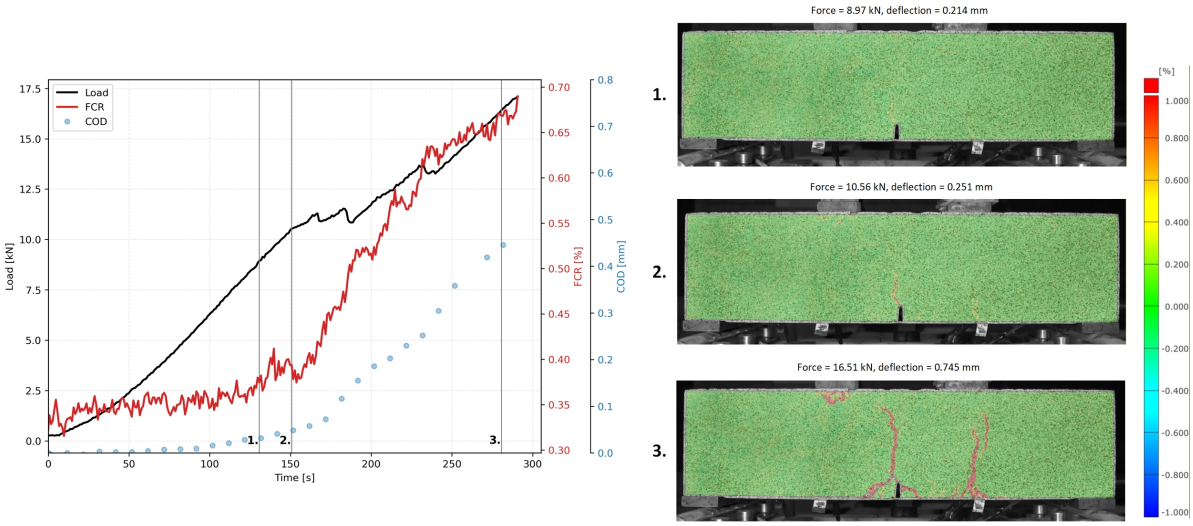

Figure 4.17: RHD2: Load, FCR, COD vs Time with DIC images

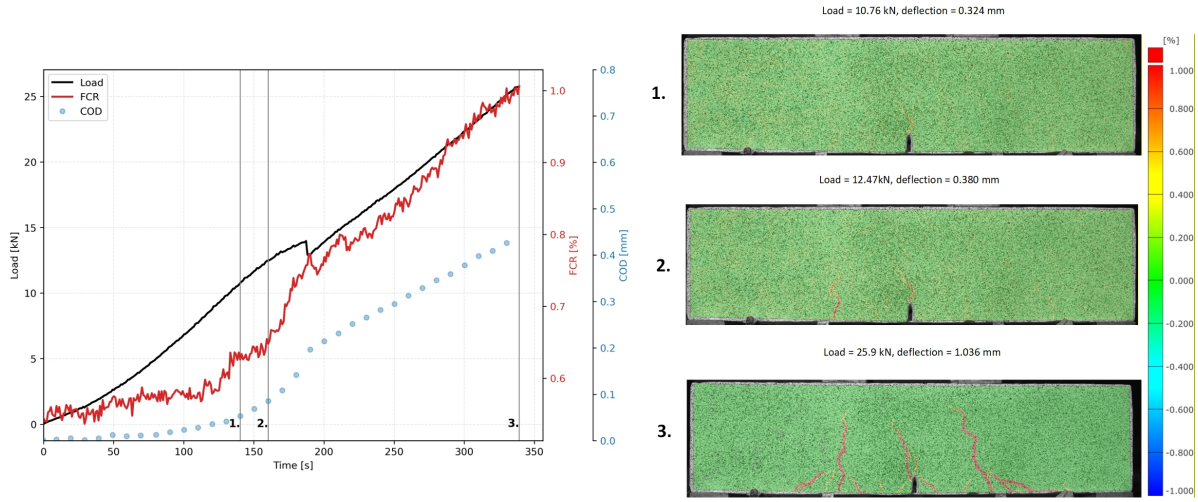

Figure 4.18: RHD3: Load, FCR, COD vs Time with DIC images

4.2. Iteration 2

4.2.1. Pre-testing: Qualitative Results

In Iteration 2, the specimens were cured using an autoclave, which applies pressure during the curing process. After curing, the surface of the composite was flat and smooth. At none of the specimens hollow sounds by tapping or an uneven surface were found.

Comparison
Some specimens in Iteration 1 exhibited an uneven surface and hollow sounds, whereas this was not observed in Iteration 2. Additionally, the copper strips were clearly visible in all specimens from Iteration 1, as indicated by the red ovals in Figure 4.19. In contrast, Iteration 2 specimens had flat surfaces, and the copper strips were mostly not visible after curing. These observations suggest that autoclave curing in Iteration 2 improved both the surface quality and bonding of the composite.

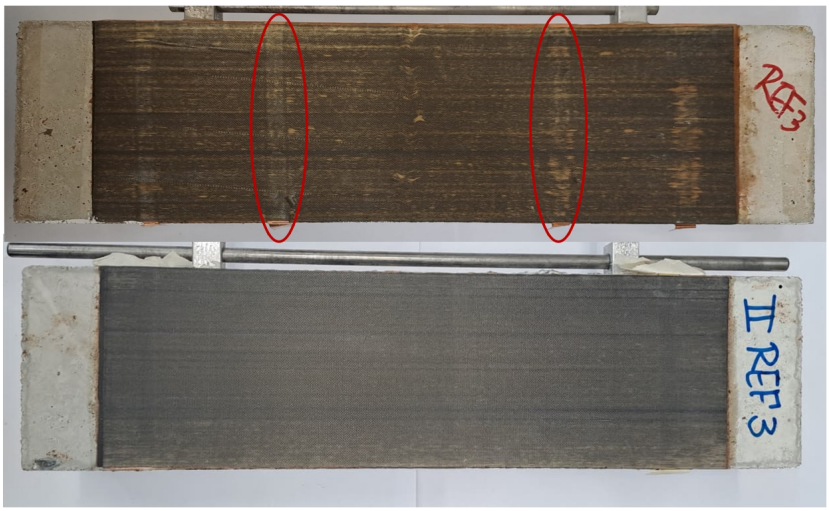

Figure 4.19: Comparison visual results between REF 3 from Iteration 1 (top image) and 2-REF 3 from Iteration 2 (bottom image)

4.2.2. Initial Resistance Measurements

The initial, static resistance of the specimens were measured using a multimeter. All three specimens, showed an initial resistance (R_0) of approximately 1 Ohm with a STD less 5%.

The change in resistance is measured using a bridge configuration, explained in section 3.7.2. During the tests, the measurements are in relative current change with an amplification factor of 1000. In order to relate these relative current change back to the resistance change, formulas 3.10 and 3.11 are used.

Using formula 3.10 gives a nominal current of:

$I = \frac{6}{(350+350+1)} = 0.0085592A$

Using formula 3.11, gives:

$\Delta R = \frac{U_U}{I*1000} = \frac{U_U}{8.5592}$.

Where U_U is the measured relative current change. To determine the resistance R, the initial resistance R_0 need to be subtracted from the relative resistance change ΔR. From Formula 3.10, it can be noticed that a difference in initial resistance result in minor and neglible changes. Therefore, the initial resistance of the specimens are considered to be 1 Ohm.

Comparison
An initial resistance of approximately 1 Ω is about 2–3 times higher than the initial resistance of the specimens in Iteration 1. This difference can be explained by the change in the distance over which the resistance is measured: in Iteration 1, the distance is 120 mm, whereas in Iteration 2 it is 280 mm.

From Formula 2.1, it can be seen that an increase in the effective length L can lead to higher initial resistance values. Considering a length $L = 260$ mm, the theoretical resistance R_{CFRP} is 0.78 Ω, which is again of the same order of magnitude as the experimentally obtained initial resistance of 1 Ω.

4.2.3. Overview of Mechanical and Electrical Behaviour

The three retrofitted specimens in Iteration 2 are tested without any pre-damage. Although retrofitting is typically applied to cracked or damaged structures, testing intact specimens allows for a clear baseline assessment of the retrofit's effect on stiffness, load and electrical response. Furthermore, measurements were conducted through the composite, enabling direct observation of the material's internal behavior under load, independent of pre-existing cracks. The mechanical and electrical test results are shown in Table 4.4. As mentioned in section 3.7.3, the specimens were tested with and without glued support plates and with and without overlap to the composite. It can be clearly seen that specimen 2-REF3:gluedoverlap, which had glued supports and had overlap with the composite, reached the highest load of 94.60 kN after which the test was stopped because the ultimate loading of the machine (100 kN) was nearly reached and no further risks were taken. It can also be seen that the ultimate failure load of specimens 2-REF1:glued and 2-REF2:nonglued are close to eachother, although one had glued supports and the other not. Furthermore, it can be noticed that the maximum FCR value from specimens 2-REF1 and 2-REF2 are close to eachother, while this it not the case for the minimum FCR value. Further analysis on this will be done in the next section.

Group	Specimen	F_{max} [kN]	Deflection [mm]	Strain at F_{max} [%]	FCR min. [%]	FCR max. [%]
2-REF	1	26.52	0.920	0.2286	-0.809	73.55
	2	26.82	0.994	0.2457	-119.86	73.23
	3*	94.60	2.33	0.7370	-7.50	924.22

Table 4.4: Overview test results Iteration 2
*Experiment stopped before the specimen reached ultimate load due to the load capacity limit of the testing setup.

4.2.4. Post-testing: Qualitative Results

Mechanochromic effects
No color change corresponding to cracks are detected in the composite layer. From Table 4.4, it can be noticed that for specimens 2-REF1 and 2-REF2 the carbon strain-to-failure limit of 0.3% is not reached

in order to experience visual color change. This is not the case for specimen 2-REF3, where a strain is reached of around 0.7%.

Failure Modes
Again, DIC images and post-test inspections were used to determine the failure mode. For specimens 2-REF1 and 2-REF2, the observed failure mode was a diagonal shear crack at the plate end. Since specimen 2-REF3 did not reach its ultimate failure load, no failure mode could be identified.

Figure 4.20: Specimen 2-REF1 after testing

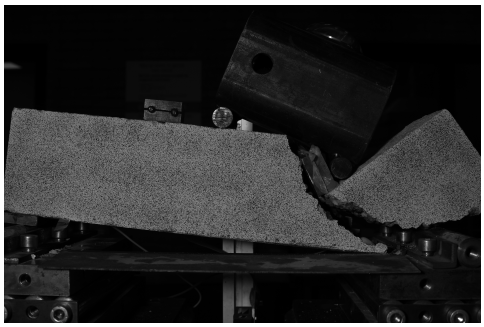

Figure 4.21: Specimen 2-REF2 after testing

Bonding
In Figures 4.22 and 4.23, the cross sections of specimens 2-REF1 and 2-REF2 are shown. Some differences in the break lines can be seen. Specimen 2-REF1 shows a clear break line along the edge of the composite, while for specimen 2-REF2 part of the composite is still attached and some debonding between the concrete and the composite can be observed.

Figure 4.22: Cross section specimen 2-REF1 with glued support plates after testing

Figure 4.23: Cross section specimen 2-REF2 without glued support plates after testing

4.2.5. Piezoresistive behaviour

The piezoresistive behaviour of all three specimens is presented in Figures 4.24, 4.25, and 4.26. Each graph shows the load and the fractional change in resistance (FCR) over time during the experiment. A similar pattern can be observed across the specimens. For each specimen, Phases I, II, and III are identified, while specimen 2-REF3 exhibits an additional Phase IV.

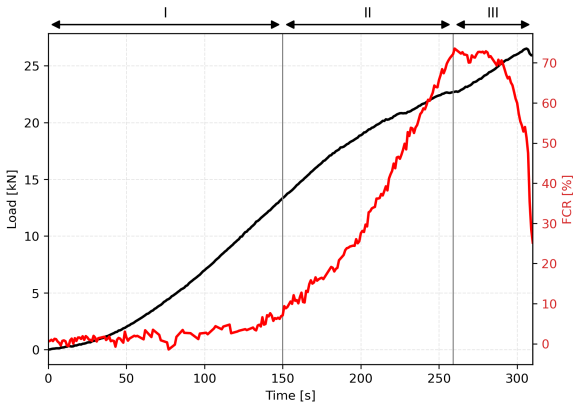

Figure 4.24: Piezoresistive behaviour specimen 2-REF1

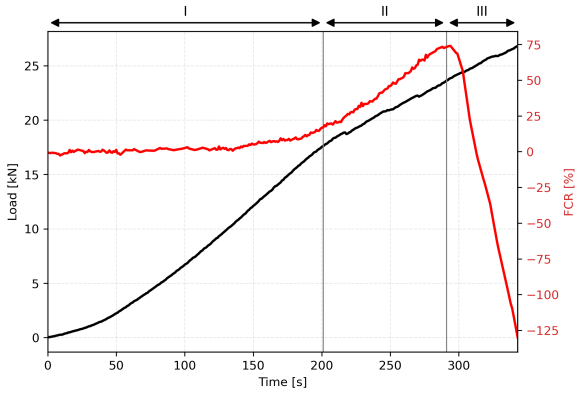

Figure 4.25: Piezoresistive behaviour specimen 2-REF2

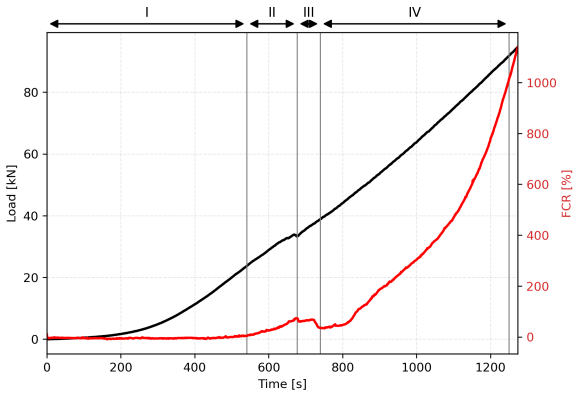

Figure 4.26: Piezoresistive behaviour specimen 2-REF3

Phase I corresponds to the period before cracking of the beam, representing the linear-elastic behaviour. In this phase, the load increases gradually, while the FCR remains below 10% for all specimens.

Phase II marks the onset of concrete cracking. The slope of the load curve decreases slightly compared to Phase I. The FCR shows a pronounced increase, reaching a peak value of approximately 75% for each specimen.

Phase III is characterized by a continued increase in load, while the FCR begins to decrease. The minimum FCR values vary among the specimens.

For specimen 2-REF3, an additional **Phase IV** is observed. During this phase, after a brief period of stability, the load continues to increase linearly, whereas the electrical response rises more rapidly than in Phase I.

A peak in FCR followed by a subsequent drop during Phases II and III is observed for all specimens. To allow for comparison, all specimens are plotted together in a single graph. From Figure 4.27, several observations can be made. First, the peak FCR values are all approximately 73%, although they occur at different load levels. For specimens 2-REF1 and 2-REF2, the peak FCR is observed between 20 and 25 kN, whereas for specimen 2-REF3, the peak occurs at around 35 kN. Second, specimens 2-REF1 and 2-REF2 reach their peak FCR approximately 50 seconds prior to their respective ultimate loads. In contrast, for specimen 2-REF3, the load continues to increase beyond the point of peak FCR.

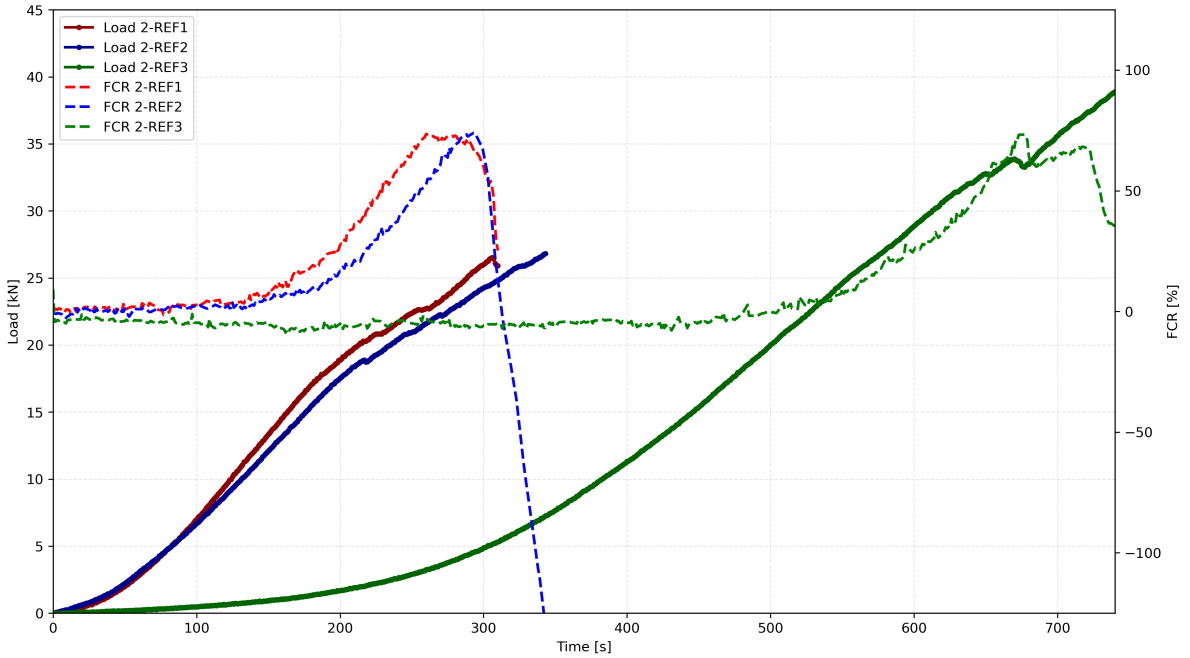

Figure 4.27: Phases I-III: Comparison Load & FCR all specimens

4.2.6. Correlation between Load, FCR and COD

Similar to Iteration 1, the relationship between Load, FCR, and COD is analyzed. The COD is measured using a virtual extensometer between the two strips. This time, the measurement is taken over a larger area, as illustrated in Figure 4.28.

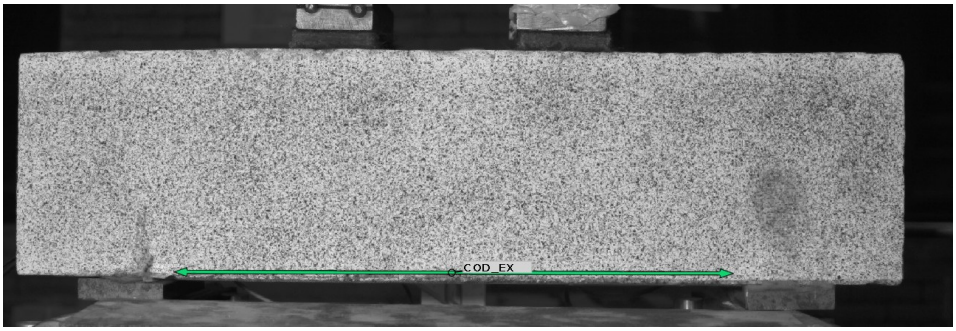

Figure 4.28: Placement virtual COD extensometer between electrodes Iteration 2

The load, COD and FCR response in time are shown in Figures 4.29, 4.30 and 4.31. Next to it, different timesteps with different strain levels in the concrete are shown, indicated with vertical lines in the main graph. For specimen 2-REF1, three main timepoints are plotted. The first one, indicated at the start of the increase for both FCR and COD, where no high strain level can be observed in the DIC. At the second and third timestep, the FCR is at its highest and from the DIC image multiple high strainlevels can be noticed.

A clear difference with Iteration 1, are the amount of high strain lines. In Iteration 1, often a single localized high strain zone was observed. While in Iteration 2, there are clearly multiple high strain zones.

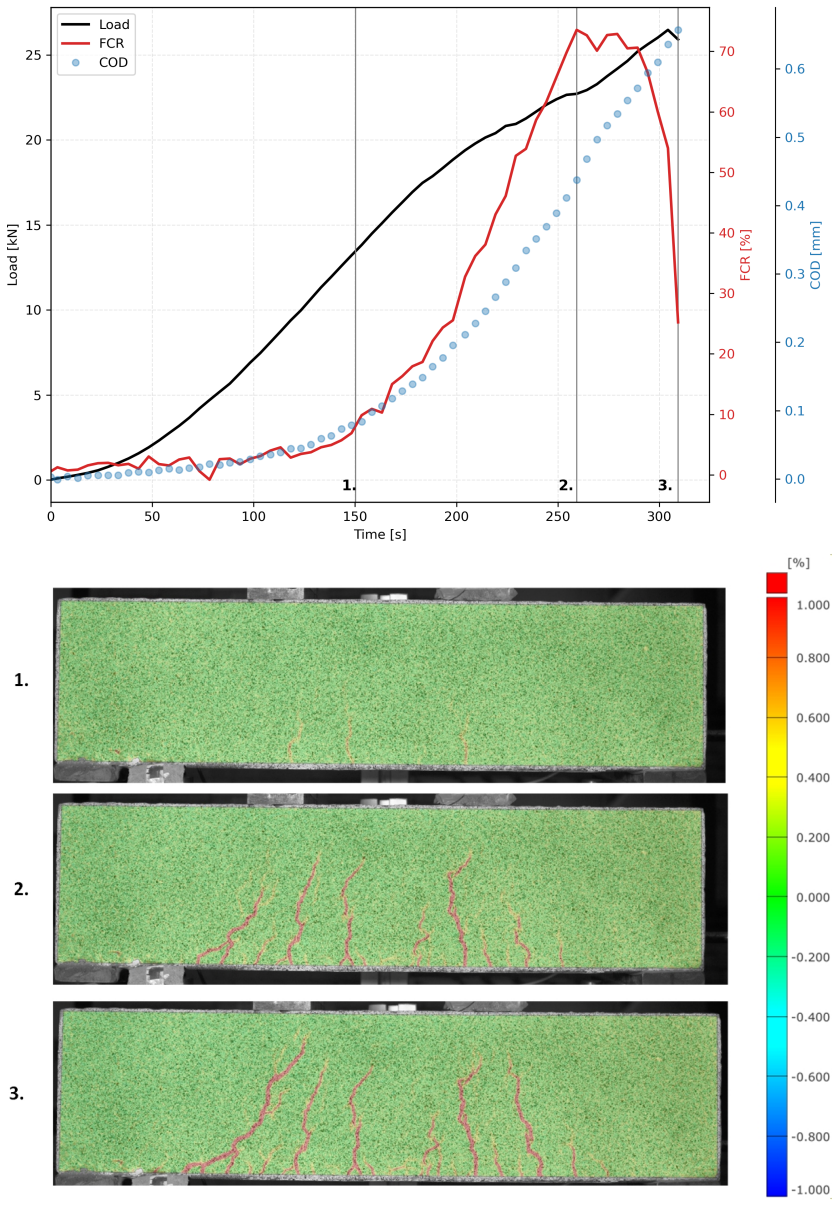

Figure 4.29: 2-REF1: Load, FCR, COD vs Time with DIC images at different timesteps

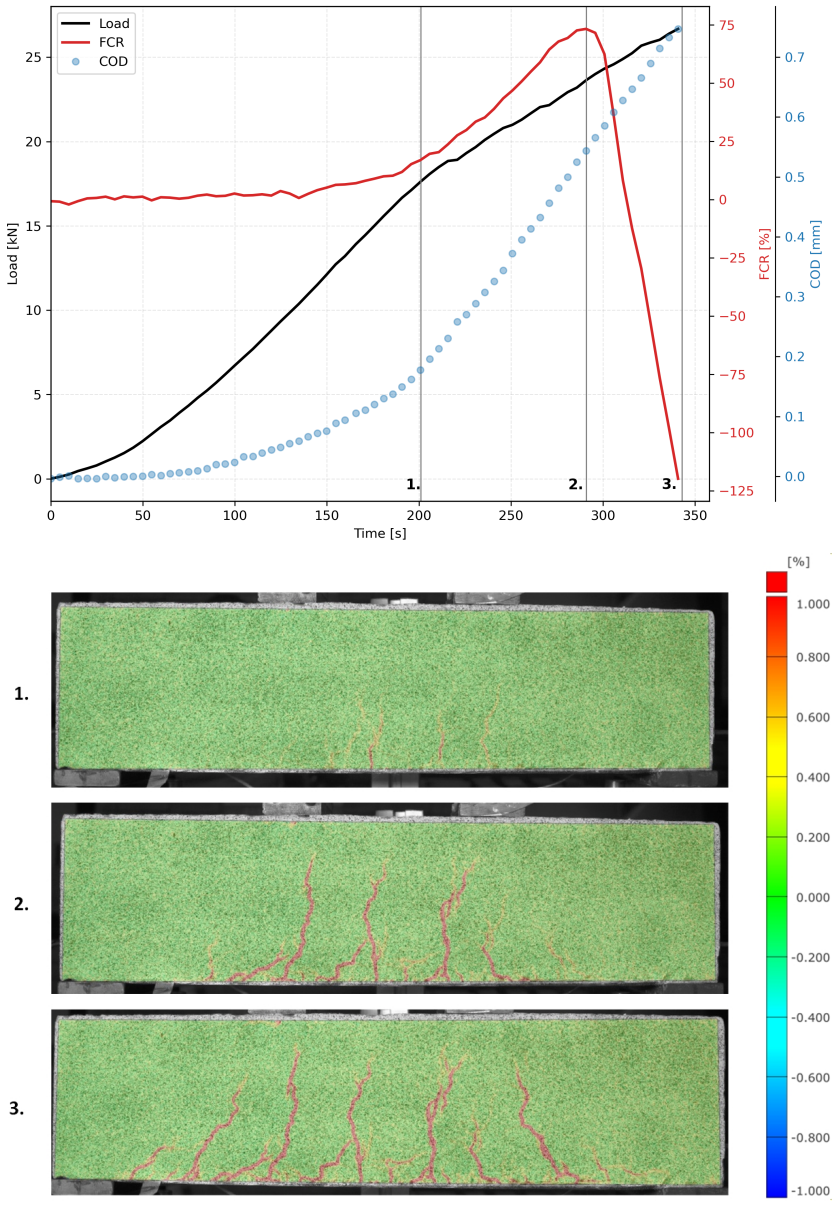

Figure 4.30: 2-REF2: Load, FCR, COD vs Time with DIC images at different timesteps

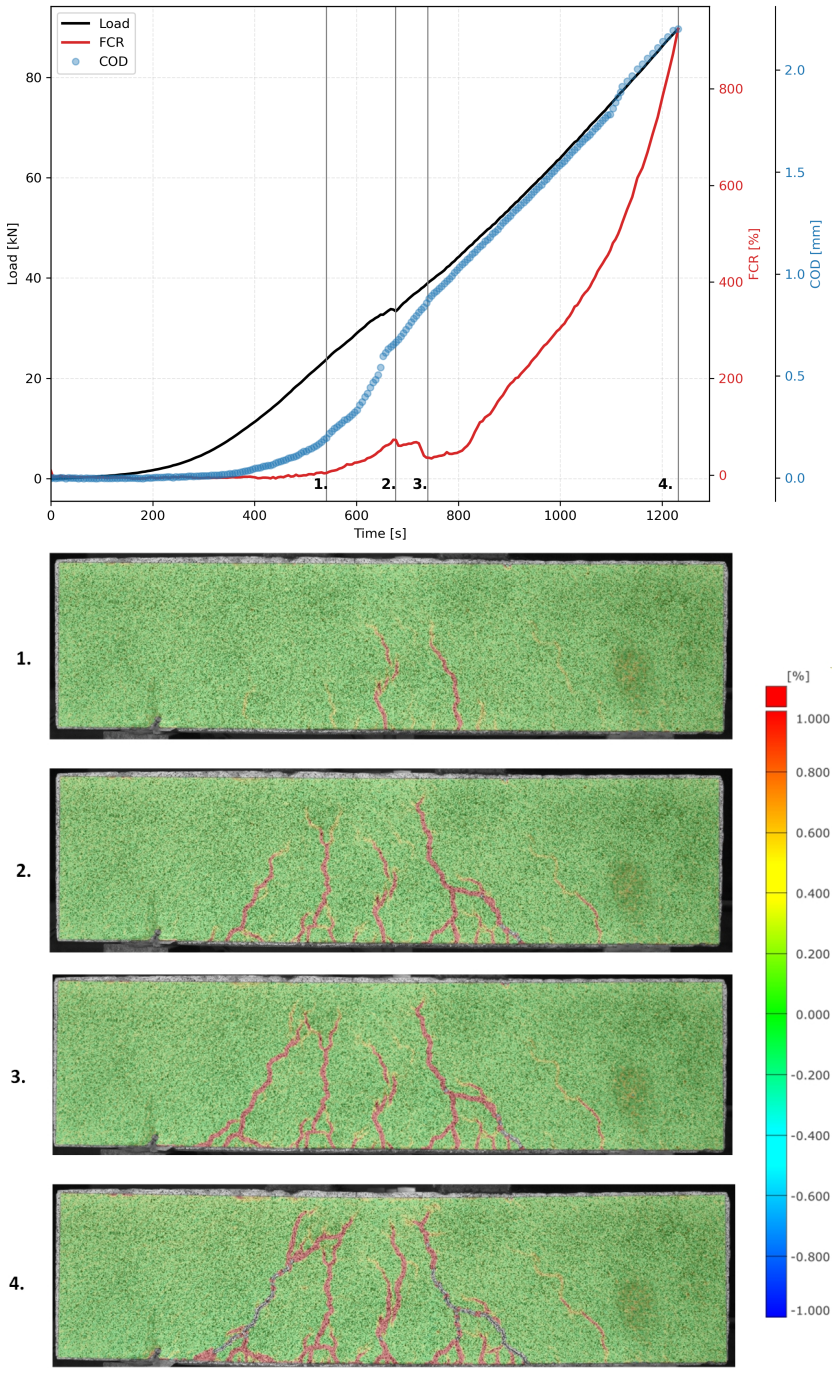

Figure 4.31: 2-REF3: Load, FCR, COD vs Time with DIC images at different timesteps

4.2.7. Sensor Sensitivity Analysis

To quantify the sensitivity of the carbon layer as a sensor, the gauge factor is an important parameter. As described in Section 3.3.2, the GF is defined as the derivative of the resistance change with respect to strain. The GF curve reflects the sensor's sensitivity, with peaks indicating strain levels at which the sensor responds most strongly. The second derivative of FCR with respect to strain highlights transitions in the sensor response. Peaks in this second derivative typically correspond to a high sensor sensitivity which is caused by damage events, such as microcracks or fiber–matrix debonding. Regions where the second derivative is close to zero indicate continuous, linear sensor response despite ongoing damage. This information can be used to define different phases of sensor behavior and to verify whether the sensor response is consistent across specimens. From Section 4.2.5, it became clear that the resistance change over time exhibits three similar phases across the specimens. Based on the timing of these phases, the corresponding strain level are summarized in Table 4.5.

In the next paragraph, the FCR-strain curve and its first and second derivative are plotted against for each specimen. For each graph, vertical lines are plotted to highlight the different phases described in Section 4.2.5. This makes it easier to compare the FCR in time with the FCR against strain. The goal is not to analyse specific peaks since relating but to find a relation in sensor response between the different specimens.

Specimen	ϵ_I **[%]**	ϵ_{II} **[%]**	ϵ_{III} **[%]**	ϵ_{IV} **[%]**
2-REF1	0.019	0.161	0.250	-
2-REF2	0.036	0.167	0.247	-
2-REF3	0.025	0.161	0.229	0.738

Table 4.5: Strain levels at transitions between different phases

In Figure 4.32, the FCR–strain response and its first and second derivatives are shown for specimen 2-REF1. It can be seen that the FCR against strain show a linear region in phase I and II, followed by a drop and showing negative linearity between FCR and strain in phase III.

As mentioned, the GF vs strain shows the sensitivity of the sensor. It can be seen that the sensitivity in phase I is high, showing multiple peaks for little strain difference. At higher strain levels, the sensor becomes more stable with some distinct peaks. From the second derivative, transition points can be noticed. It follows that the transition from phase I to phase II, is also visible in this graph. In phase II and phase III, the second derivative becomes a stable value, meaning that the response of the sensor stays the same.

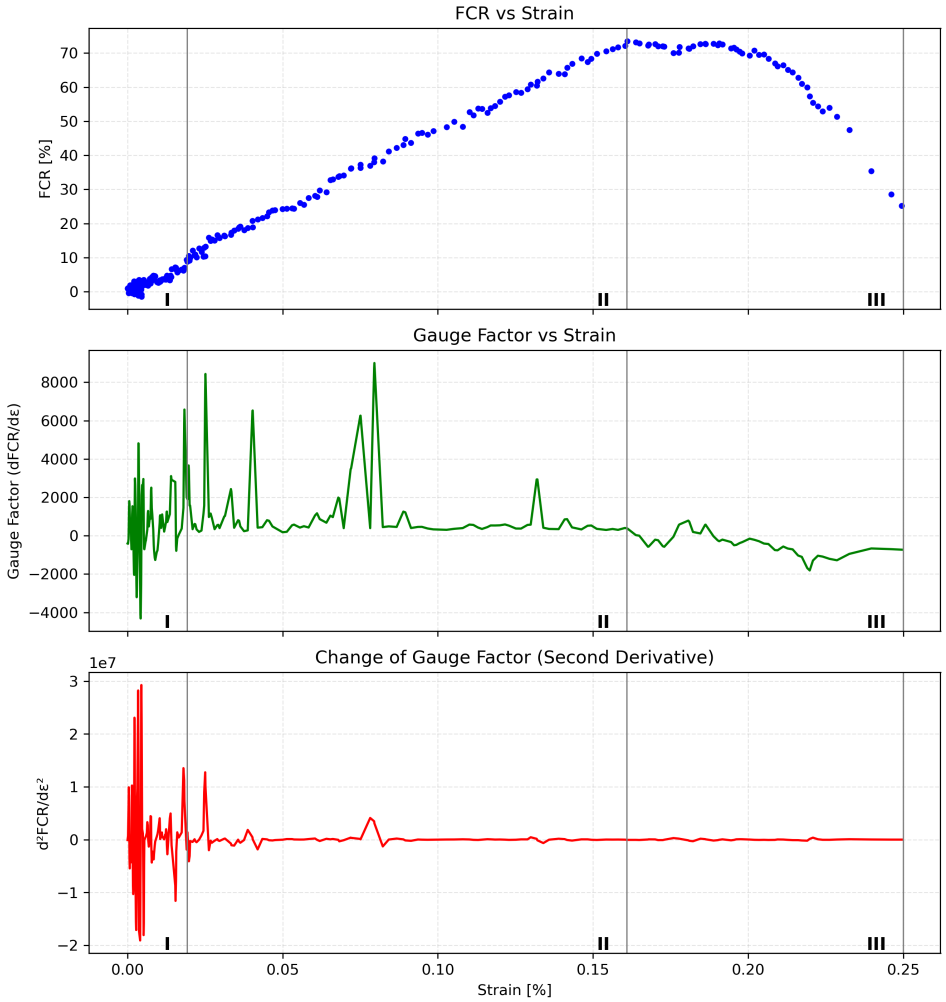

Figure 4.32: Specimen 2-REF1 sensor sensitivity: FCR vs Strain, GF vs Strain, Second derivative vs Strain

Similar approach can be done for specimen 2-REF2, 2-REF3, showing similar results in Figures 4.33 and 4.34. For specimen 2-REF3, a clear sensor response can be seen at the drop in FCR. An additional phase IV can be seen for specimen 2-REF3. In phase IV a nonlinear FCR-strain response is seen. Showing a clear transition at a strainlevel higher than 0.3%. It can be seen that the peaks in the second derivative are more spread out over different strainlevels compared to phase I.

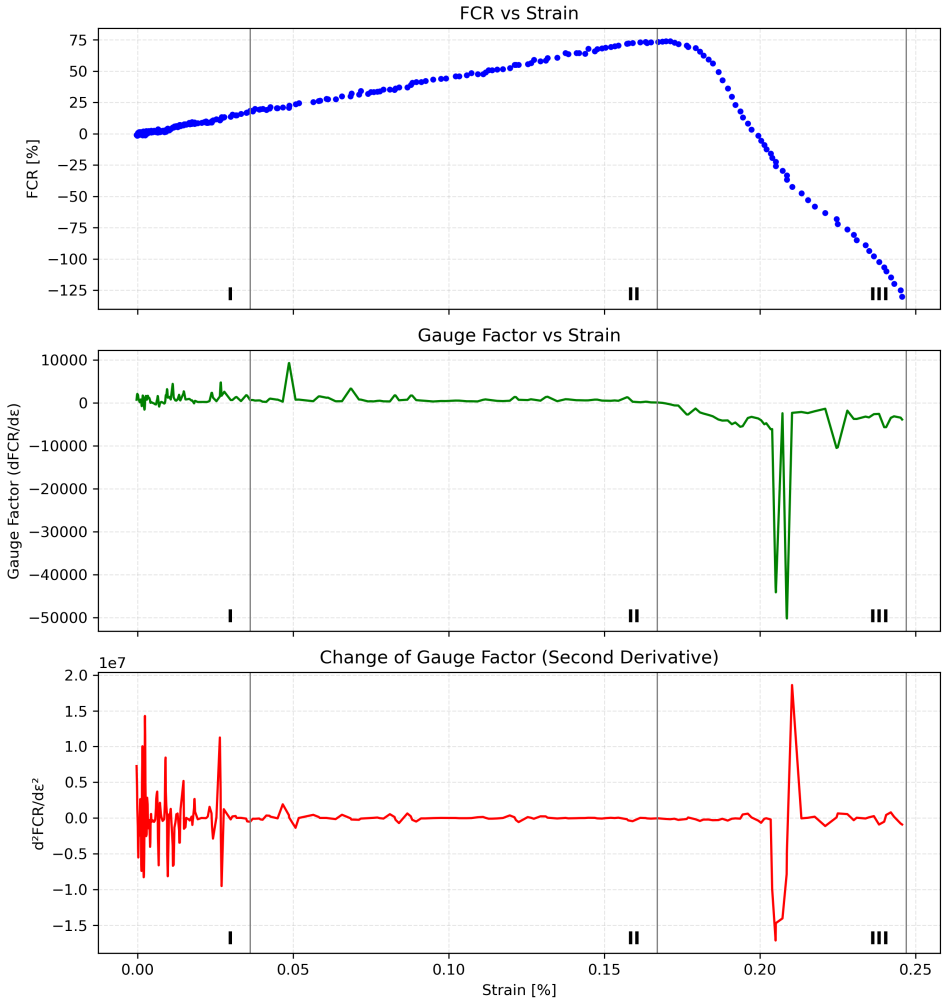

Figure 4.33: Specimen 2-REF2 sensor sensitivity: FCR vs Strain, GF vs Strain, Second derivative vs Strain

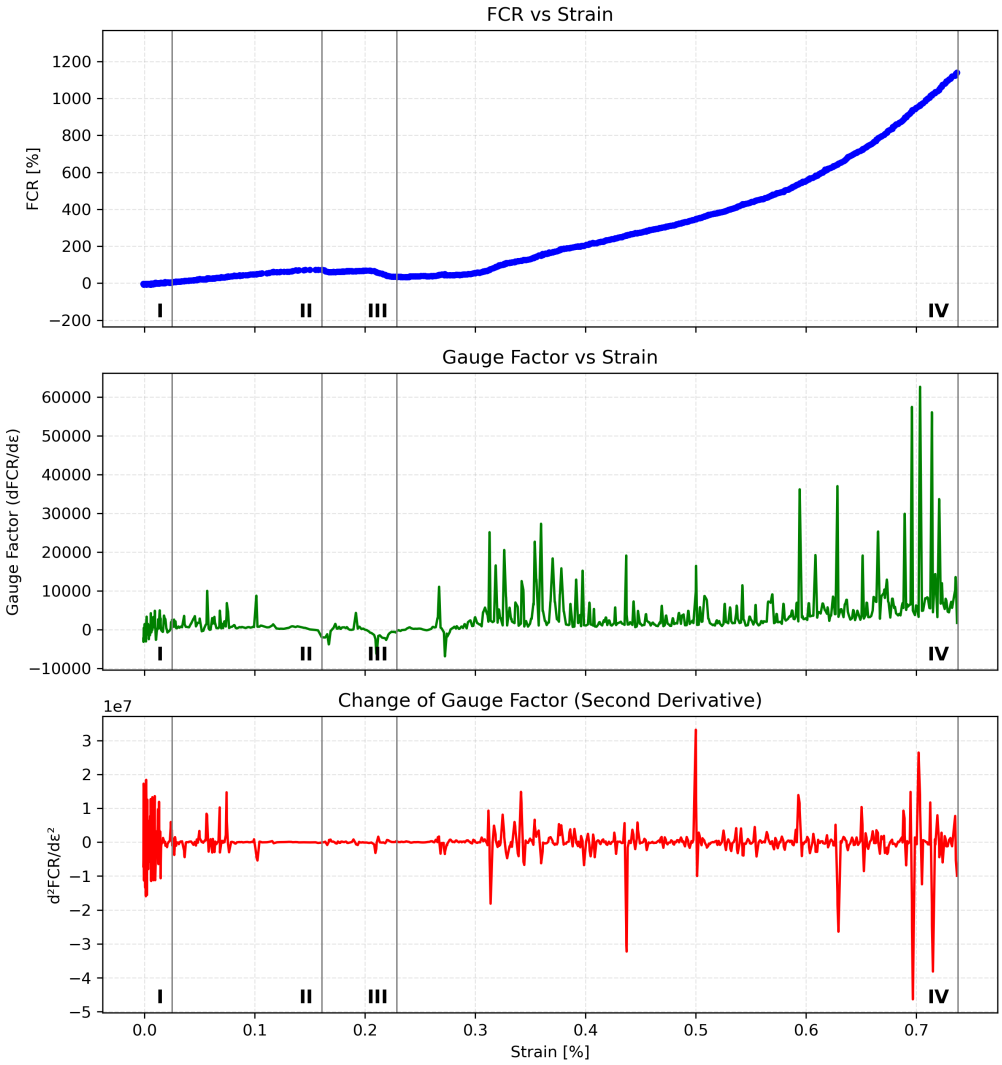

Figure 4.34: Specimen 2-REF3 sensor sentivity: FCR vs Strain, GF vs Strain, Second derivative vs Strain

Gauge Factor

It can be seen that a linear region in the FCR/strain curve is visible in phases I and II. Since, it can also be noticed that the sensor is highly sensitive in phase I and becomes more stable in phase II, it is decided to determine the GF for each specimen in both phases. A linear fit is used to determine the gauge factor for each specimen in phase I and phase II. This can be seen in Figures 4.35, 4.36 and 4.37.

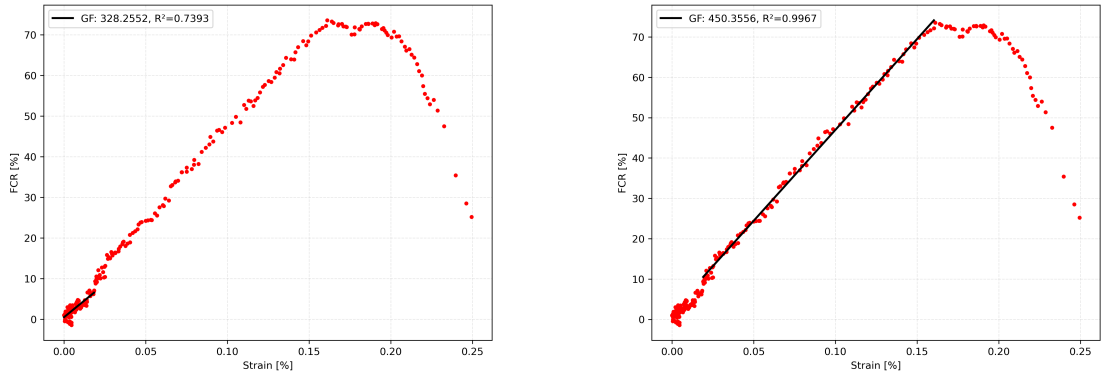

Figure 4.35: Gauge Factor fits specimen 2-REF1

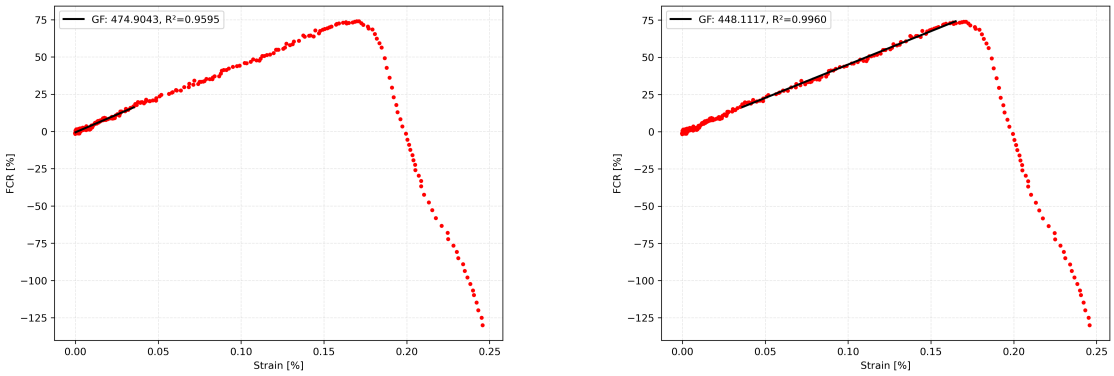

Figure 4.36: Gauge Factor fits specimen 2-REF2

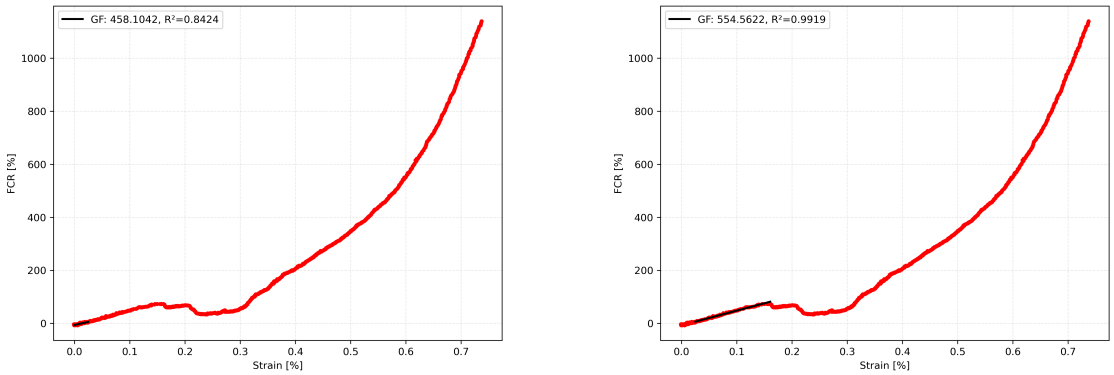

Figure 4.37: Gauge Factor fits specimen 2-REF3

In Table 4.6, the calculated GF values are presented along with the corresponding R^2 values, which indicate the quality of the linear fit. A value of R^2 closer to 1 implies a better fit to the data. It can be observed that the R^2 values in Phase II are generally closer to 1 compared to Phase I, indicating that the linear fits in Phase II represent the sensor response more accurately. Moreover, the GF values in Phase II are more consistent across specimens, reflecting a more stable and reproducible sensor behavior in this phase.

Specimen	GF Phase I [-]	R² Phase I [-]	GF Phase II [-]	R² Phase II [-]
2-REF1	328.26	0.740	450.36	0.997
2-REF2	474.90	0.960	448.11	0.996
2-REF3	458.10	0.842	554.56	0.992
Mean	420.42	0.847	484.34	0.995
Std	78.61	0.115	59.37	0.003

Table 4.6: Gauge Factor (GF) and R^2 of linear fit for each specimen in Phase I and Phase II, including mean and standard deviation.

5 Discussion

This chapter focuses on the interpretation of the experimental results and the implication and limitations of this research. The results show a consistent pattern in piezoresistive behaviour across the different specimens. This indicates that integrating copper strips into the carbon layer enables reliable electrical measurements within the carbon network. Moreover, the observed resistance changes correspond closely with the crack opening displacement, suggesting that the electrical measurements are capable of detecting crack formation and propagation. In this chapter, a reflection is performed on the results of Iteration 1 and a further analysis and interpretation of on the piezoresistive behaviour and the sensor sensitivity is conducted for the three specimens from Iteration 2.

5.1. Reflection of Iteration 1

Iteration 1 did not perform as expected, and based on its outcomes Iteration 2 was conducted, in which the issues identified in Iteration 1 were addressed. The first major issue observed in Iteration 1 concerned the bonding directly after curing. Earlier research [10] reported a flat and smooth composite surface after curing. In contrast, the specimens in this study showed a bubbly and locally hollow surface, with clear variation between individual specimens. It is expected that the copper strips would cause only a small local discontinuity, but not the hollow regions observed in the composite. Two explanations can therefore be given for the uneven surface.

First, an additional layer of electric paint was applied between the copper strips and the carbon layer, intended to improve electrical contact. However, it is likely that this paint spread during curing, interfering with the prepreg layers and creating bubbles especially near the copper strips.

Second, the curing method differed from previous research: Iteration 1 used oven curing, whereas the reference study relied on autoclave curing. Although oven curing was chosen because it is easier to apply and more representative of real-life practice, autoclave curing provides additional pressure during curing, which enhances bonding. The poor bonding observed is supported by the post-test images, showing that air was entrapped between the composite and the concrete. These hollow regions inhibited proper interaction between concrete and composite and reduced the reliability of the electrical measurements.

This inadequate bonding is also reflected in the mechanical and electrical results. The ultimate loads showed unexpected behaviour: specimens with a large notch (high damage) reached higher ultimate loads than undamaged specimens. This contradictory outcome is likely related to the variations between specimens in bonding quality. Since the specimens had to be produced individually, stable curing conditions along the specimens could not be ensured. The early failure of the specimens, combined with low ultimate loads and strains, meant that no color change occurred in any specimen. A color change is expected to occur above 0.3% strain, which was only reached by one specimen (RLD3, 0.32%). However, this strain was measured on the concrete surface, but due to poor bonding, the composite likely experienced a lower strain.

The electrical measurements also showed substantial scatter. All specimens exhibited a maximum resistance change below 1%, corresponding to only a few tenths of an ohm, raising questions about the reliability of these results. Nevertheless, six out of nine specimens showed a clear positive relation between load and resistance change, and in several specimens the initiation of crack opening could be identified by a change in slope of the resistance curve. Furthermore, six specimens showed a load drop accompanied by a corresponding drop in resistance, which is consistent with unloading of the carbon fibers. Only in specimen REF2 a load drop coincided with an increase in resistance. Before this drop, no measurable resistance change was observed, suggesting that the load drop may have activated the fibers, which aligns with the DIC observations showing first cracking at the same load level. In specimen RLD2, a clear negative relation between load and resistance change was observed after some time. Negative piezoresistivity has been reported in cases of poor electrical contact causing inhomogeneous current flow [31], suggesting a localised issue in the copper–electric-paint–fiber interface for this specimen.

In conclusion, the results of Iteration 1 were primarily affected by poor bonding, likely due to the spreading of the electric paint or the use of oven curing instead of autoclave curing, which does not apply additional pressure during curing. This insufficient bonding strongly influenced the mechanical and electrical be-

haviour of the specimens. Despite these limitations, several specimens still showed a clear relationship between load, crack opening and resistance change, indicating potential for this method in crack monitoring. As outlined in the Methodology, the factors that likely caused poor bonding, along with an improved electrical setup, were addressed in Iteration 2.

5.2. Iteration 2 - Piezoresistive behaviour

An important factor to indicate the performance of the sensor, is the electrical resistance over time compared to the load and crack opening displacement. From the results, it can be obtained that the manufacturing method has a large influence on the mechanical and electrical behaviour of the specimens. Although, the results from Iteration 1 are dominated by the bonding behaviour, a similar positive piezoresistivity can be observed between the results from Iteration 1 and Iteration 2.

5.2.1. Analysis different phases

Iteration 2 shows comparable phases in piezoresistive behaviour for all three specimens, as described in Section 4.2.5. This consistency suggests that the sensing behaviour primarly originates from the material itself, rather than from differences between the specimens.
Phase I corresponds to the linear-elastic behaviour of the beam, the electrical response remains below 10%. This limited sensitivity can be explained by the microstructure remaining largely intact, with only small changes in the number of fiber-to-fiber contact points. Figure 5.1, shows Phase I of specimen 2-REF3. It can be seen that a short period of a lower (negative) resistance change is observed. This initial negative resistance change followed by an increase can be assigned to the fact that the fibers will go from wavy to straight state, where new contact points between the carbon fibers will shortly occur and result in decrease of the resistance change [46].

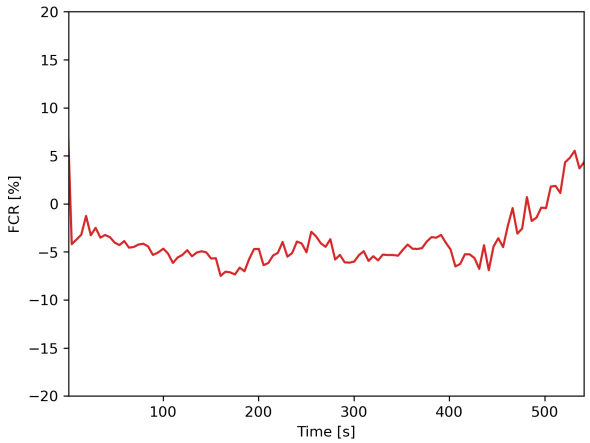

Figure 5.1: Negative resistance change in Phase I of specimen 2-REF3

Phase II shows a clear increase in electrical resistance as the applied load continues to rise. During this phase, the electrical resistance is influenced by the evolution of fiber-to-fiber contact points as well as by the stretching of the fibers [47] [48]. This fiber stretching is primarily induced by the initiation of concrete cracking. The width-to-length ratio affects the number of fiber-to-fiber contacts and, consequently, the electrical resistance measurements. In the present study, the width-to-length ratio is relatively large (0.3), which increases the likelihood of fiber-to-fiber contacts and has a significant influence on the longitudinal electrical resistance measurements of the CFRP. In contrast, for specimens with a low width-to-length ratio, the change in electrical resistance is mainly governed by the change in fiber length due to the Poisson effect [49]. FCR–strain curves in Section 4.2.7 indicate that Phase II occurs below a strain of approximately 0.2%. Since this is below the failure strain of the carbon fibers, actual fiber fracture is unlikely. This confirms that the resistance increase in Phase II is primarily caused by ongoing changes in fiber contacts and fiber stretching rather than structural damage.
Phase III is characterized by a drop in electrical resistance while the load continues, corresponding to

significant concrete cracking. For specimens 2-REF1 and 2-REF2, this occurs before reaching its ultimate load. Similar behaviour was reported by Goldfeld et al. [50], where a decrease in electrical resistance was measured simultaneously with an increase in load. This reduction in electrical resistance can be associated with a local reduction of internal stresses in the carbon layer caused by local debonding. Debonding prevents load transfer between the concrete and the composite in the affected area, leading to a reduction of stress in the carbon layer. Similar to cyclic loading tests, the unloading phase corresponds to a decrease in electrical resistance. On microstructural level, the electrical resistance reduces due to the decrease in length during unloading and the increase in cross-section of the fibers, which leads to higher electrical resistance. However, this reduction in internal stresses is not immediately reflected in the global load curve. The observed delay between changes in electrical resistance and the load response can be explained by the difference in scale: the electrical resistance is sensitive to micro structural changes, whereas the load curve reflects macro structural behavior of the beam. The results from this study show a delay of approximately 50 seconds between the peak in electrical resistance and the ultimate load for both specimens 2-REF1 and 2-REF2. In the study by Goldfeld et al. [50], a similar delay of 350 seconds was reported, which was attributed to the asymmetrical development of cracks along the beam. The electrical roving used to measure resistance was located close to a specific crack, detecting microstructural damage before it was reflected in the global load response. The similar delay times and FCR values observed suggest that the sensor is capable of detecting the onset of failure at an early stage.

Taking a closer look at the drop in FCR for specimen 2-REF3, it becomes clear that this reduction aligns with the formation of two distinct shear cracks in the concrete. Post-test observations reveal delamination towards the support plate, indicating that this specimen followed the same failure mechanism as the other two specimens, shown in Figure 5.2. However, complete failure at the time that FCR drops was prevented due to the overlap between the support plate and the composite, which mechanically restrained the beam from failure.

(a) Left side **(b)** Right side

Figure 5.2: Post-test images of Specimen 2-REF3 showing delamination in the regions highlighted with red circles.

Therefore, the drop in resistance change is closely related to crack formation in the concrete and ultimate failure of the beam. This can be related to early detection of reduction of internal stresses on microstructural level, which is not shown in the global load curve yet. The negative response can be confirmed by specimen 2-REF3, which was unloaded after reaching the maximum load capacity of the test set-up. In Figure 5.3, the unloading response is shown. It shows that the load curve decreases in less than 100 seconds from ultimate load to zero. It can also be seen that there is a slight offset with the resistance change, which first further increases and after some time shows a decrease. First of all, this confirms that the sensor is correctly measuring the crack response, as the cracks of the concrete will close during the unloading stage. As a result, the carbon fibers will be less tensed and the resistance will become lower. Important aspect here is that the ultimate resistance change value becomes a negative value around -70%, indicating a better resistance compared to the initial resistance. It is likely that the resistance after unloading will not return to its initial value. Due to changes in the fiber network and the formation of microcracks in the epoxy matrix, the composite may undergo a structural rearrangement during unloading. This reconfiguration can create additional contact points within the conductive network, resulting in a lower resistance than in the original, unloaded state. This supports the observation that unloading is accompanied by a downward electrical resistance response, resulting in a negative resistance change at the ultimate state, as also observed for specimen 2-REF2.

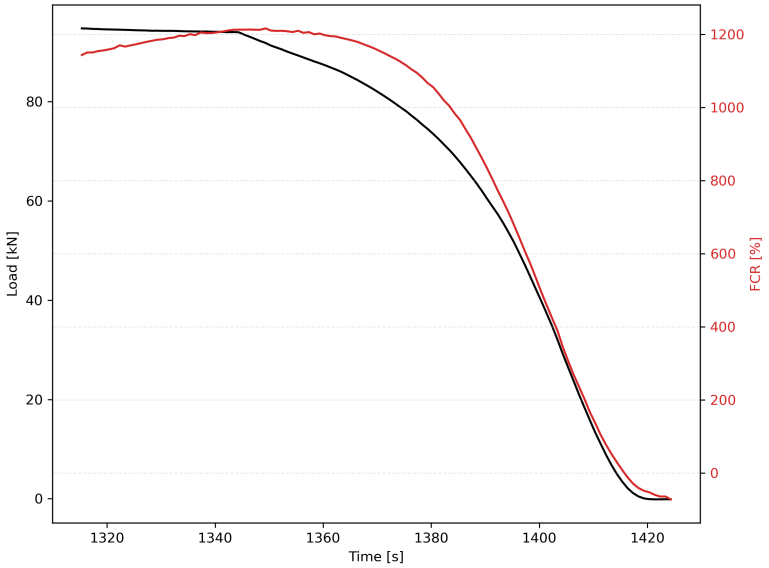

Figure 5.3: Unloading response 2-REF3

An alternative explanation reported in the literature is that redistribution of electrical potential between cracked and uncracked regions can cause sudden FCR reductions [43]. This hypothesis would suggest that the drop is due to the initiation of a major shear crack adjacent to the measurement area. However, both specimens failed on shear cracks next to the support plate, outside the measurement area. Furthermore, the crack opening displacement within the measurement area continues to increase while the resistance drops. Therefore, the drop in resistance is unlikely to result from crack opening elsewhere, supporting the conclusion that it arises from microstructural reduction of internal stresses.

Phase IV was observed for specimen 2-REF3, in which the load continues to increase while the electrical resistance rises even more rapidly. This phenomenon can be explained by the fact that the flexural beam effectively behaves as two rigid segments, with the composite layer carrying the tensile load in this stage. The carbon fibers become increasingly stretched and, due to the overlap region where the composite is bonded to the support plate, fiber movement is restricted. Consequently, the electrical resistance continues to rise. This behaviour is consistent with the findings previous research [50], and is further supported by Figure 4.34, which shows a clear sensor response immediately following the formation of the concrete crack.

5.3. Support plates

The results show that debonding at the concrete–composite interface, triggered by flexural or shear cracking, remains the governing failure mechanism. The specimens with glued and non-glued support plates exhibit nearly identical load–COD–FCR behavior. Post-testing images indicate that the glued specimen tends to develop cracks towards the end of the composite, while the non-glued specimen shows cracks more towards the middle and some debonding. Although it cannot be confirmed whether these differences are solely due to the presence of glued plates, it is clear that support plates with overlap on the composite help delay early failure. In real-life applications, this overlap is difficult to realize, since retrofitting typically occurs at a later stage.

5.4. Mechanochromic effects

No color change was observed during one of the tests. As mentioned, the carbon fibers used, have a strain-to-failure of 0.3%. In this type of mechanochromic composite, color change occurs when the carbon fibers fail, causing incident light to reveal light strips in the composite. From the measured strain values, it can be seen that only two specimens exceeded this 0.3% threshold, so a color change would have been expected. It should be noted that the strain values were obtained from LVDT sensors placed at the

bottom of the concrete substrate. It is assumed that the complete FRP layer exhibits the same strain as the concrete. However, due to imperfect bonding, it is likely that the actual strain in the composite is lower than the values measured by the LVDT.

A difference compared to the study by Mohammadi et al. [10] is that only notched retrofitted specimens were tested. A notch induces stress concentrations, which lead to higher local strains. This could explain why no color change was observed. However, this reasoning is not fully consistent with the reported mechanism of color change. While local strain concentrations can trigger color change, it is not strictly required to initiate color change [2]. In the experimental setup of this research, two rollers were used to allow free horizontal movement and to achieve pure bending. For brittle failures, this configuration is preferred over a pinned–roller support, since the roller support can suddenly slide away in the test setup when the specimen fails. A pinned–pinned support configuration is rarely used, as it introduces additional axial forces in the specimen along with bending moments. Higher axial forces can lead to increased stresses and strains. For very stiff materials, such as FRP, this can result in higher ultimate loads because hinged supports restrict horizontal movement. It is sure that these aspects should be further investigated on mechanochromic effects.

5.5. Sensitivity of the sensor

From the FCR/strain graph, a clear linear region can be distinguished in Phases I and II for each specimen. The first derivative indicates a high sensor sensitivity in Phase I, which decreases in Phase II; this behavior is also reflected in the second derivative.
As described in Section 5.2.1, Phase I is dominated by the loss of contact points between the carbon fibers due to settling of the fiber network. The graphs clearly show that the sensor response is high during this phase, as contact points change rapidly at low strain levels. After this phase, the sensor responds differently, which is again reflected in both the first and second derivatives. Although the FCR/strain curve remains linear, the second derivative stabilizes around zero, indicating a more stable sensor response. During Phase II, the carbon fibers are mainly stretched, which results in less variation compared to the loss of contact points, as this is a more stable and less random process. In Phase III, a decay in the FCR/strain response is observed. However, only specimen 2-REF2 exhibits a pronounced peak in the second derivative, indicating a different type of behavior compared to the earlier phases.
For comparison purposes, the FCR/strain curves of all three specimens are shown in Figure 5.4. It becomes evident that specimen 2-REF2 shows a sharper decay in FCR with increasing strain during Phase III compared to the other specimens. Upon closer inspection, specimen 2-REF2 clearly experienced debonding, as shown in Figure 4.23 in Section 4.2.4. After failure, the fibers are visibly exposed. In contrast, specimen 2-REF1 did not show this behavior and failed due to shear failure of the concrete near the support plate.

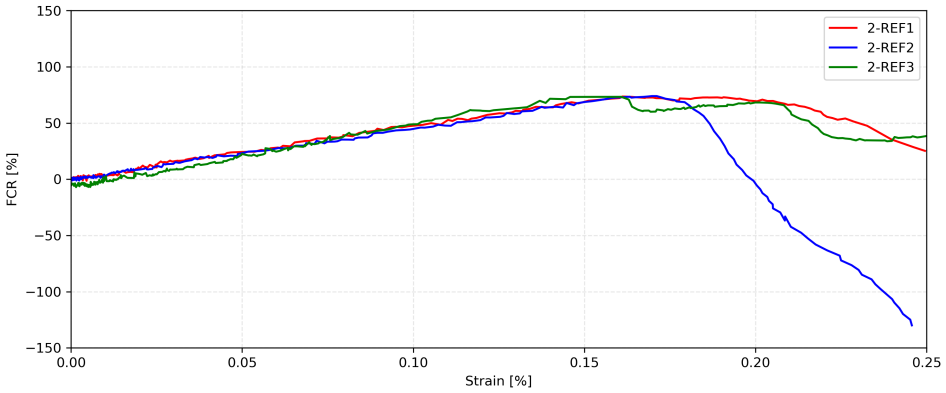

Figure 5.4: Comparison of FCR/strain curves for all specimens in Phases I–III

The observed decay in the FCR/strain response is therefore believed to originate from differences in the failure mechanism rather than from concrete cracking. In the case of debonding, local separation occurs at the concrete–composite interface, leading to the formation of interfacial cracks directly beneath the composite sensor layer. These interfacial cracks are expected to increase sensor sensitivity, as they develop in close proximity to the composite surface.
Debonding does not occur instantaneously but rather progressively, with localized regions of the composite losing adhesion to the concrete surface in discrete steps. Each partial loss of adhesion results in a sudden, short-term redistribution of strain within the composite layer, effectively causing local unloading of the sensor. This unloading is observed as a decrease in electrical resistance, which is reflected by the sharp decay in the FCR/strain curve.
During the experiments, the debonding process was accompanied by audible cracking sounds from the composite layer. Initially, this was interpreted as fracture of the composite itself; however, this is considered less likely than interfacial debonding, as complete fracture of the composite would result in a more abrupt and irreversible electrical response. As debonding progresses, additional small openings develop at the interface, further reducing the effective strain transferred to the composite sensor and leading to a continued reduction in FCR as the carbon fibers become increasingly unloaded. This mechanism explains the pronounced decay observed in specimen 2-REF2.
Although debonding also occurred in specimen 2-REF3, the exact onset is difficult to identify due to continued loading after initiation. Consequently, it cannot be stated with certainty that debonding occurred at higher strain levels as the crack further developed. Nevertheless, the response of specimen 2-REF3 differs from that of specimen 2-REF2, as the fibers were mechanically restrained by glued support plates. This constraint prevents complete detachment of the composite layer from the concrete, thereby limiting strain release and resulting in a less pronounced decay in the FCR/strain response.
Furthermore, Digital Image Correlation (DIC) measurements confirm that no significant changes in surface crack formation occur at the strain levels corresponding to the observed decay. This suggests that the sensor response is not governed by concrete cracking and supports the hypothesis that the observed changes in slope are primarily related to interface phenomena rather than global concrete damage.

Previous studies have demonstrated that variations in bond–slip behavior and interfacial adhesion can be detected through electrical and impedance-based measurements, supporting the general interpretation that sensor response is influenced by interface degradation [51] [52]. In the present study, specimen 2-REF2 shows a more pronounced decay in FCR compared to specimens without debonding, which is attributed to progressive interfacial debonding, as confirmed by post-testing observations. Although such comparative trends are not documented in the literature, our observation is consistent with the known sensitivity of electrical sensors to interface damage.

A limitation of the experimental setup is that strain measurements were obtained on the concrete surface rather than within the composite sensor itself. As a result, local unloading of the composite due to interfacial debonding cannot be directly captured by the strain measurements. While a local reduction in strain within the composite sensor would be expected during unloading, the measured strain continues to increase during this phase, reflecting the global deformation of the concrete rather than the local mechanical state of the composite. This mismatch further supports the hypothesis that the observed decay in FCR is governed by a reduction in strain transfer efficiency at the concrete–composite interface, rather than by global unloading or concrete cracking.

Phase IV specimen 2-REF3
From the sensor response, it becomes evident that specimen 2-REF3 exhibits a higher sensitivity. This is observable from the non-linear FCR/strain behavior, which is further supported by the first and second derivatives showing multiple peaks. As discussed in Section 5.2.1, during this phase the composite, together with the overlap of the support plates, helps hold the beam in place. The carbon fibers are highly engaged in this region, as illustrated in Figure 5.5, which shows a pronounced response at strain levels exceeding 0.3%. This strain limit corresponds approximately to the failure strain of the carbon fibers, suggesting that the fibers begin to fail beyond this point. However, no evidence of failure is observed from mechanochromic effects, as noted previously.

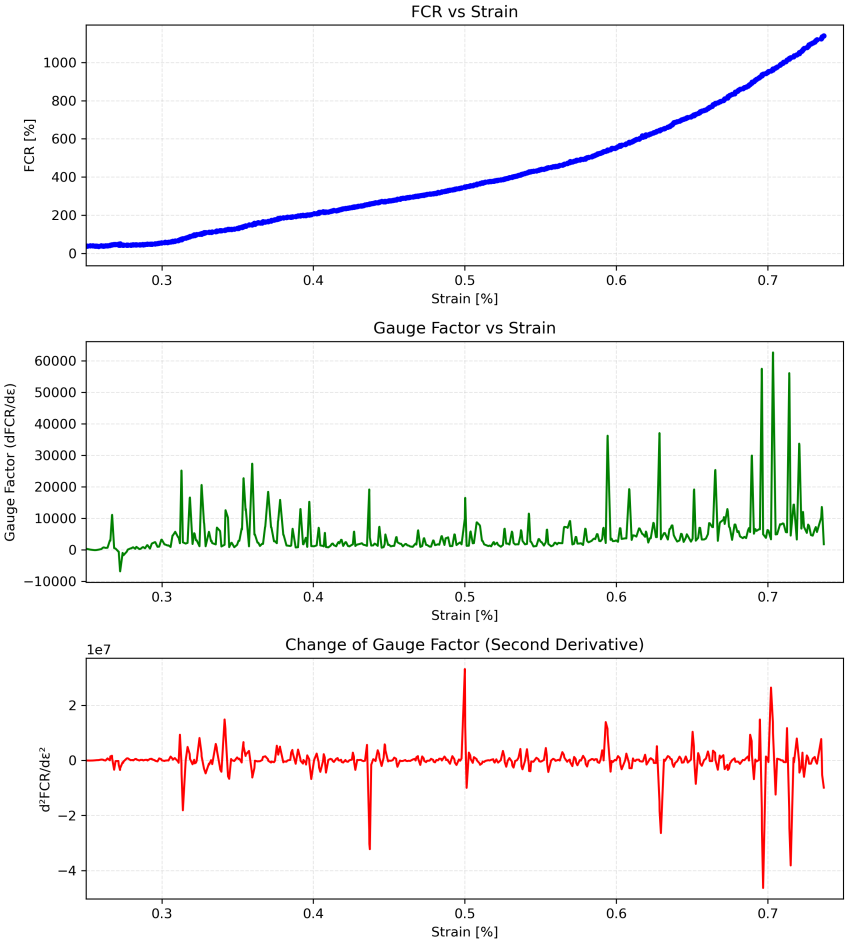

Figure 5.5: Specimen 2-REF3 sensor sentivity phase IV

Gauge Factor

Devices such as conventional metal strain gauges typically have a gauge factor (GF) around 2 [45], which limits their sensitivity for detecting small strains. The GF of carbon fibers depends on their elastic modulus, resistivity, and, in composites, the fiber volume fraction. In this study, the fit to the Phase II data was better than for Phase I, indicating that the sensor was more sensitive in Phase II, possibly due to minor differences in sensor placement or calibration. Despite these variations, the measurements were consistent across specimens, demonstrating the reliability of the carbon fiber sensing approach.

The mean GF of the specimens in Phase II is 484 with a standard deviation of 59, which is significantly higher than that of conventional metal strain gauges. This high value can be attributed to the intrinsic piezoresistive behavior of the carbon fibers and their alignment within the composite layer. Previous studies have reported GFs between 100–400 for carbon fibers [53], highlighting that variations in fiber type, orientation, or fabrication process can strongly influence sensitivity. Overall, the results suggest that carbon fiber layers are promising for highly sensitive strain sensing applications.

5.6. Implications

The results of this study demonstrate that carbon fiber–based electrical resistance sensors integrated in FRP-retrofitted concrete beams can effectively capture damage initiation, progression, and pre-failure behavior under flexural loading. A clear relationship between applied load, crack opening displacement, and electrical resistance response was observed, highlighting the sensitivity of the conductive network to mechanically induced changes.

The measurements further reveal that the electrical response of the carbon layer reflects local mechanical behavior, which may precede changes observed at the global structural level. In two specimens, this resulted in a measurable time delay of approximately 50 seconds, indicating the potential of the sensing system to provide early warning of approaching structural failure. Across all specimens, a consistent drop in electrical resistance occurred prior to ultimate failure at a similar fractional resistance change level of approximately 75%. It should be noted that this value is specific to the current experimental setup, including the carbon layer configuration and sensor calibration; in other setups, such as reported by Goldfeld et al [50], the corresponding fractional change may differ (e.g., 5.8mΩ). This indicates that while the 75% threshold is robust within this study, it should be interpreted relative to the specific system rather than as a universal value.

The high gauge factor of the composite sensor emphasizes its ability to detect small strain levels, outperforming conventional metallic strain gauges. Although overlapping the composite with the support plates increased the ultimate load capacity in one specimen, the electrical response associated with concrete cracking remained comparable to specimens without overlap. This indicates that the increased capacity resulted from mechanical restraint rather than improved concrete performance, underscoring the importance of designing the composite system in compatibility with the concrete behavior.

The observation that concrete failure occurred before the carbon fibers reached their strain-to-failure limit suggests that the current configuration does not fully exploit the sensing potential of the composite, particularly for mechanochromic or high-strain sensing applications. Moreover, the results highlight the critical role of boundary conditions, as variations in support and loading constraints significantly influence local stress and strain distributions, thereby affecting both sensor response and structural behavior.

5.7. Limitations

This research has several limitations related to the experimental setup that may affect the interpretation of the results.

Strain measurements on the concrete surface
Strain measurements were performed on the concrete surface using an LVDT positioned close to the composite layer. For simplicity, it was assumed that strain transfer is optimal and that the composite, including the carbon layer, experiences similar strains. However, this study highlighted the importance of bonding between concrete and composite. Local drops in electrical resistance caused by unloading of the carbon fibers cannot be directly confirmed by these strain measurements, which limits the ability to fully capture local interface phenomena.

Interpretation of FCR drops
The observed slope and drops in FCR are associated with debonding or interface mechanisms. However, direct measurements of interface behavior were not available, so other contributing factors cannot be completely excluded.

2D/3D measurement limitations
Electrical resistance was measured on the bottom surface, while DIC measurements were taken from the side of the specimen. It is assumed that strain levels propagate uniformly through the specimen, but local variations in fiber orientation and distribution may cause differences in strain and electrical response that are not captured. Additionally, electrical measurements were recorded as single values, preventing the identification of the exact location or mode of crack formation.

Environmental factors
Electrical resistance of carbon fibers can be influenced by environmental factors such as humidity, temperature, and light. During Iteration 2 experiments, a light source was directed at the composite surface to enable bottom-side recordings. Although the observed increase in current was minor (<1%) and measurements were started only after stabilization, environmental effects cannot be completely ruled out.

5.7.1. Sample size and repeatability

The limited number of specimens reduces the statistical significance of the observed gauge factors and FCR values. Measurement noise, instrument resolution, and local material variability may also introduce small errors, emphasizing caution when generalizing these results to other specimens or larger-scale applications.

6 Conclusion

This chapter answers the research question and the supporting subquestions. The main research question of this research is:

"To what extent can electrical resistance measurements through a conductive network in mechanochromic composites be used to detect damage in FRP-retrofitted concrete beams under flexural loading?"

To support the main research question, several subquestions have been formulated. Answering these subquestions, will help to answer the main research question.

1. What methods can be employed to integrate a conductive network within mechanochromic composites for the purpose of electrical resistance-based damage detection?

Different methods have been investigated to integrate a conductive network within the mechanochromic composites. As discussed, the conductive carbon layer is enclosed by glass layers. First of all, the use of prepregs gives also limited options. Integration of conductive components such as carbon black and carbon nanotubes in the epoxy to enhance the conductivity of the composite are often used methods, but relatively difficult to use.

Several approaches were evaluated to establish electrical contact with the embedded carbon layer in mechanochromic composites:

- Access through the top glass layer: creating holes or removing epoxy can provide direct contact, but carries a high risk of damaging the composite and compromising its mechanical integrity.
- Edge connection: contacting the carbon layer from the prepreg edge is challenging due to the insulating polymer matrix and the thin ply, leading to unreliable measurements.
- Ply drop (shortened top glass layer): exposing part of the carbon layer at the edge is simpler and avoids direct surface modification, but may introduce local stress concentrations and reduce structural strength.
- Embedded conductive elements: inserting copper wires or strips between glass and carbon layers provides reliable electrical contact. Copper strips, in particular, offer a wide interface for improved signal reliability and acceptable mechanical performance.

Among the methods evaluated, embedding copper strips between the glass and carbon layers was found to be the most effective and practical solution, combining reliable electrical connectivity with minimal compromise of the composite's mechanical integrity. Results show a stable and reliable connection using copper strips.

2. How does the electrical resistance of the mechanochromic composite change under flexural loading in retrofitted concrete beams?

Under flexural loading of retrofitted concrete beams, the mechanochromic composite exhibits a clear and consistent electrical resistance response that can be divided into three phases. Initially, the electrical resistance remains stable or slightly decreases due to settlement and rearrangement of the carbon fibers, which increases the number of electrical contact points. In the intermediate phase, the resistance increases steadily as fiber stretching becomes dominant and concrete cracking initiates, demonstrating effective strain transfer and sufficient bonding between the composite and the concrete. Shortly before failure, a reduction in resistance change is observed, which is attributed to local unloading of the conductive network caused by crack localization and stress redistribution, while the applied load continues to increase at the global structural level.

3. To what extent do changes in electrical resistance correlate with cracks identified by DIC and visual color changes?

No visual color change was observed during the experiments; therefore, a correlation between color response and damage development could not be established. Nevertheless, increases in electrical resistance show a strong correlation with crack initiation and crack opening displacement measured using DIC, confirming the sensitivity of the conductive network to damage evolution. However, the crack opening value can not be related to a specific value of resistance change in this study, due to differences in test-setup.

4. How sensitive are the conductive network sensors embedded in the mechanochromic composite, as quantified by their gauge factor?

The conductive network sensors embedded in the mechanochromic composite are highly sensitive, as quantified by a mean gauge factor of 484, which is orders of magnitude higher than that of conventional metal strain gauges. This indicates excellent capability for detecting small strains. The high sensitivity arises from the intrinsic piezoresistive behavior of the carbon fibers and their alignment within the composite layer. Measurements across multiple specimens were consistent and reliable, confirming the reproducibility of the sensors. The data show a better fit at higher strain levels (Phase II) compared to lower strain levels at the beginning of the experiment (Phase I), likely because the sensors are initially very sensitive due to rapid changes in electrical resistance caused by fewer fiber contact points. Overall, these results demonstrate that the composite sensors are promising for applications requiring highly sensitive and repeatable strain monitoring in structural materials.

The main research question: **"To what extent can electrical resistance measurements through a conductive network in mechanochromic composites be used to detect damage in FRP-retrofitted concrete beams under flexural loading?"**

This study demonstrates that electrical resistance measurements through a conductive carbon fiber network using copper strips can be used to reliably detect damage initiation, damage progression, and approaching failure in FRP-retrofitted concrete beams under flexural loading, provided that sufficient bond quality between the composite and the concrete is ensured.

The sensing approach is highly sensitive to small strain levels well below the strain-to-failure of the carbon fibers, enabling early-stage damage detection associated with concrete crack initiation and crack opening. Furthermore, a consistent and reproducible drop in electrical resistance was observed prior to ultimate failure at a similar fractional resistance change level of approximately 75% across all specimens. This characteristic response occurred up to 50 seconds before failure in well-bonded specimens, demonstrating the potential of the method as an early-warning indicator of critical structural damage states.The 75% threshold appears to be primarily damage-related rather than load-related, reflecting local crack development within the composite layer rather than the global applied load. It should be noted that this value is specific to the current experimental setup, including sensor configuration, bonding quality, and measurement conditions, and may differ in other systems.

The results also show that the applicability of the technique is limited in poorly bonded retrofitted specimens, where electrical resistance responses are highly specimen-specific and do not exhibit a clear or consistent trend. In such cases, damage localization and quantitative interpretation of the electrical signal are considered unreliable.

Overall, electrical resistance measurements in conductive carbon fiber composites are most effective as a global structural health monitoring tool for detecting damage onset, progression, and pre-failure behavior in FRP-retrofitted concrete beams, rather than for precise damage localization or visual mechanochromic indication under the tested conditions.

7 Future recommendations

The recommendations presented in this chapter focus on four key aspects that should be addressed to further improve the effectiveness of mechanochromic composites for damage detection in FRP-retrofitted concrete structures.

Strain measurements within the composite system
Future research should include direct strain measurements on the composite layer or embedded within the carbon fibers themselves. Such measurements would enable a more accurate correlation between mechanical strain, electrical resistance change, and damage development, and would help to better interpret the electrical sensing response.

Optimization of the concrete–composite interface and sensor design
Further optimization of the interface between the concrete substrate and the composite layer is recommended. In the current configuration, the full potential of strain sensing is not fully utilized, as strain transfer to the conductive network may be incomplete. Additionally, the influence of sensor geometry, particularly the effect of larger sensing areas on electrical resistance change, should be systematically investigated to improve sensitivity and reliability.

Influence of boundary conditions and test configuration
The experimental boundary conditions and loading setup should be carefully evaluated in future studies. Boundary conditions strongly affect strain distribution and crack development, which in turn influence both electrical and mechanochromic responses. Improved test configurations may enable higher and more uniform strain levels, potentially activating mechanochromic effects.

Crack localization and spatial resolution of damage detection
To enhance damage localization, future sensing approaches should focus on measuring electrical resistance between defined, smaller sensing regions rather than across a bulk area. Segmenting the conductive network or employing multi-electrode measurement layouts would provide improved spatial resolution, enabling more accurate identification of crack locations and a better assessment of measurement performance and accuracy. In theory, this would be relatively easy to achieve, but it requires specific equipment which could not be obtained in this research.

Microstructural analysis and CFRP behavior
Finally, detailed microstructural analysis of the CFRP and the conductive network is recommended to better understand damage mechanisms, fiber interaction, and electrical percolation behavior. Such analysis would support the interpretation of electrical resistance changes and contribute to improved material design and performance prediction.

Test on specific damage levels
In this research, no distinction between predefined damage levels was made during the second test iteration due to time constraints, as the focus was placed on capturing the overall structural response rather than responses influenced by artificial damage such as notches. For future research, it is strongly recommended to investigate sensor performance at well-defined and realistic damage levels that are representative of real-life structural conditions.

Instead of introducing notches to simulate damage, damage should preferably be induced through mechanical loading. For example, in the case of retrofitted steel-reinforced concrete beams, specimens could be loaded until initial cracking occurs, after which the retrofit is applied and subsequent loading is performed. This approach would provide a more realistic assessment of the sensor response to damage initiation and progression in practical applications.

References

[1] TNO. *Duurzaam Infrastructuur*. Accessed: 2023-04-03. 2023. URL: https://www.tno.nl/nl/duurzaam/infrastructuur/.

[2] Tamas Rev et al. “A simple and robust approach for visual overload indication UD thin-ply hybrid composite sensors”. In: *Composites Part A: Applied Science and Manufacturing* 121 (2019), pp. 376–385. DOI: 10.1016/j.compositesa.2019.03.005.

[3] Jonas N. Fuhg, Stefan Kollmannsberger, and Ernst Rank. “Physics informed neural networks for computational engineering: A selective review of recent advances”. In: *Archives of Computational Methods in Engineering* 29 (2022), pp. 715–756. DOI: 10.1007/s11831-021-09665-9.

[4] CRL. *Grouting and Injection*. Accessed: 2025-04-02. 2025. URL: https://crl.uk.com/grouting_injection.php.

[5] G. Czél. “Demonstration of pseudo-ductility in high performance concrete by means of engineered microstructure”. In: *Cement and Concrete Research* 53 (2013), pp. 1–10. DOI: 10.1016/j.cemconres.2013.06.001. URL: https://www.sciencedirect.com/science/article/pii/S1359835X13001176.

[6] Christoph Weder. “Mechanochromic Polymers”. In: *Encyclopedia of Polymeric Nanomaterials*. Ed. by Editor(s) Name. Springer, 2014. DOI: 10.1007/978-3-642-36199-9_6-4. URL: https://link.springer.com/referenceworkentry/10.1007/978-3-642-36199-9_6-4.

[7] Reza Mohammadi et al. “Bending performance of concrete beams retrofitted with mechanochromic glass/carbon hybrid composites: Combining structural reinforcement and visual health monitoring”. In: *Construction and Building Materials* ((2024)). doi: 10.1016/j.conbuildmat.2024.047391, https://www.sciencedirect.com/science/article/pii/S0950061824047391.

[8] Sujeong Pyeon et al. “Crack Evaluation of Concrete Using Mechanochromic Sensor”. In: *Materials* 16.2 (2023), p. 662. DOI: 10.3390/ma16020662. URL: https://www.researchgate.net/publication/367004311_Crack_Evaluation_of_Concrete_Using_Mechanochromic_Sensor.

[9] Christian Viets, Simon Kaysser, and Karl Schulte. “Damage mapping of GFRP via electrical resistance measurements using nanocomposite epoxy matrix systems”. In: *Materials Science and Engineering: A* 588 ((2013)), pp. 8–14. DOI: 10.1016/j.msea.2013.02.032. URL: https://www.sciencedirect.com/science/article/pii/S1359836813005623.

[10] Mohammad Fotouhi et al. “Mechanochromic Hybrid Composites for Structural Health Monitoring”. In: *Proceedings of the 21st European Conference on Composite Materials (ECCM21), Volume 3 – Material and Structural Behavior – Simulation & Testing*. Ed. by Christophe Binetury and Frédéric Jacquemin. Nantes, France: European Society for Composite Materials (ESCM) and École Centrale de Nantes, 2024, pp. 855–862. ISBN: 978-2-912985-01-9.

[11] C.S. Poon and C. Jaillon. “The development and application of a prefabrication installation sequencing model”. In: *Construction and Building Materials* 20.8 (2006), pp. 669–679. ISSN: 0950-0618. DOI: 10.1016/j.conbuildmat.2005.02.008.

[12] NEN. *NEN-EN 1992-1-1:2005 en – Eurocode 2: Design of concrete structures – Part 1-1: General rules and rules for buildings*. Retrieved from https://www.nen.nl/en/nen-en-1992-1-1-2005-en-64758. 2005.

[13] Witteveen+Bos. *Crack Width Analysis App*. Geraadpleegd op 8 oktober 2025. 2025. URL: https://www.witteveenbos.com/digital-solutions/crack-width-analysis-app.

[14] BetonLexicon. *Scheurwijdte*. Geraadpleegd op 8 oktober 2025. 2018. URL: https://www.betonlexicon.nl/S/Scheurwijdte.

[15] C.F. Maier Composites. *Composites and FRP: A brief Overview*. https://www.cfmaier.com/processes/composites-and-frp-a-brief-overview. Accessed: 2025-10-10. 2025.

[16] PE F. Keith Bohren. *Fiber-Reinforced Polymer (FRP) – Simpson - Composite Strengthening Systems*. Presentation (PDF). Slides from Foundation Performance Association past presentations. Oct. 2017. URL: https://www.foundationperformance.org/pastpresentations/BohrenPresSlides-11Oct17.pdf.

[17] T. Triantafillou et al. *Externally Bonded FRP Reinforcement for RC Structures: Technical Report on the Design and Use of Externally Bonded Fibre Reinforced Polymer (FRP EBR) for Reinforced Concrete Structures*. fib Bulletin 14. Accessed: 10 October 2025. Lausanne, Switzerland: fédération internationale du béton (fib), 2001.

[18] Sarth Khunt. "Retrofitting of Concrete Structures: A Review". In: *International Research Journal of Engineering and Technology (IRJET)* 9.8 (2022). Geraadpleegd op 25 september 2025, pp. 197–202. ISSN: 2395-0056. URL: https://www.irjet.net/archives/V9/i8/IRJET-V9I834.pdf.

[19] Yasmeen Taleb Obaidat. "Structural Retrofitting of Concrete Beams using FRP – Debonding Issues". Geraadpleegd op 25 september 2025. Doctoral Thesis. Lund, Sweden: Lund University, Department of Construction Sciences, Structural Mechanics (LTH), 2011. ISBN: 978-91-7473-194-1. URL: https://www.byggmek.lth.se/fileadmin/byggnadsmekanik/publications/tvsm1000/web1023.pdf.

[20] Sika Belgium. *Koolstofwapening*. Accessed: 10 October 2025. 2025. URL: https://bel.sika.com/nl/producten/betonherstelling-bescherming/structurele-versterking/koolstofwapening.html.

[21] S. Durgadevi. "A review on retrofitting of reinforced concrete elements". In: *Journal of Building Engineering* 38 (2021), p. 102186. DOI: 10.1016/j.jobe.2021.102186. URL: https://www.sciencedirect.com/science/article/pii/S2214785320319283.

[22] D. Kachlakev. "Behavior of full-scale reinforced concrete beams retrofitted with FRP". In: *Construction and Building Materials* 14.5 (2000), pp. 281–291. DOI: 10.1016/S1359-8368(00)00023-8. URL: https://www.sciencedirect.com/science/article/pii/S1359836800000238.

[23] Sangdo Hong and Ronald S. Harichandran. "Sensors to Monitor CFRP/Concrete Bond in Beams Using Electrochemical Impedance Spectroscopy". In: *Journal of Composites for Construction* 9.6 (2005). DOI: 10.1061/(ASCE)1090-0268(2005)9:6(515). URL: https://www.researchgate.net/publication/240504814_Sensors_to_Monitor_CFRPConcrete_Bond_in_Beams_Using_Electrochemical_Impedance_Spectroscopy.

[24] Daniel A. Pohoryles et al. "Use of DIC and AE for Monitoring Effective Strain and Debonding in FRP and FRCM-Retrofitted RC Beams". In: *Journal of Composites for Construction* 21.1 (2017). DOI: 10.1061/(ASCE)CC.1943-5614.0000715. URL: https://doi.org/10.1061/(ASCE)CC.1943-5614.0000715.

[25] Quanquan Guo and Xinxing Zhang. "A review of mechanochromic polymers and composites: From material design strategy to advanced electronics application". In: *Composites Part B: Engineering* 227 (2021), p. 109434. DOI: 10.1016/j.compositesb.2021.109434.

[26] Céline Calvino et al. "Approaches to polymeric mechanochromic materials". In: *Journal of Polymer Science, Part A: Polymer Chemistry* 55.4 (2017), pp. 640–652. ISSN: 0887-624X. DOI: 10.1002/pola.28445.

[27] M. Jalalvand et al. "UD thin-ply hybrid composite sensors". In: *Composites Part B: Engineering* 174 (2019), pp. 107–116. DOI: 10.1016/j.compositesb.2019.107116.

[28] Mohamad Fotouhi et al. "Detection of fibre fracture and ply fragmentation in thin□ply UD carbon/-glass hybrid laminates using acoustic emission". In: *Composites Part A: Applied Science and Manufacturing* 86 (2016), pp. 66–76. DOI: 10.1016/j.compositesa.2016.04.003.

[29] Qian Zhao et al. "Review on the Electrical Resistance/Conductivity of Carbon Fiber Reinforced Polymer". In: *Applied Sciences* 9.11 (2019). Open access, p. 2390. DOI: 10.3390/app9112390.

[30] Jie Wen, Zhenhai Xia, and Fred K. Choy. "Damage Detection of Carbon Fiber Reinforced Polymer Composites via Electrical Resistance Measurement". In: *Composites Part B: Engineering* 42.1 (2011), pp. 77–86. DOI: 10.1016/j.compositesb.2010.08.005.

[31] N. Angelidis. "The electrical resistance response of continuous carbon fibre composite laminates to mechanical strain". In: *Composites Science and Technology* 64.7-8 (2004), pp. 1001–1010. DOI: 10.1016/j.compscitech.2004.01.002.

[32] X. Zhou et al. “Structural health monitoring of glass fiber reinforced polymers using carbon nanotube fibers”. In: *Composites Science and Technology* 70.3 (2010), pp. 452–457. DOI: 10.1016/j.compscitech.2009.11.014. URL: https://www.sciencedirect.com/science/article/pii/S0266353809003807.

[33] Bolin Jiang and Shanshan Wu. “Resistance measurement for monitoring bending cracks in steel fiber concrete beams test”. In: *Alexandria Engineering Journal* 66.6 (2023). Open access under CC BY license, pp. 691–699. DOI: 10.1016/j.aej.2022.10.074.

[34] Sheik Abdul Malik et al. “Robust Electrical Contact With Low Interface Resistance Using Embedded Co-cured Electrodes in Carbon Fibre Composites”. In: *Applied Composite Materials* (2025). Early online publication, pp. 1–28. DOI: 10.1007/s10443-025-10345-1.

[35] Yogesh R. and J.M. Chandra Kishen. “Effect Of Notch Size On The Fracture Behaviour Of Concrete”. In: *11th International Conference on Fracture Mechanics of Concrete and Concrete Structures (FraMCoS-11)*. Dec. 2023. DOI: 10.21012/FC11.0923110. URL: https://www.researchgate.net/publication/377230202_Effect_Of_Notch_Size_On_The_Fracture_Behaviour_Of_Concrete.

[36] A. Yudhanto et al. “Surface preparation strategies in secondary bonded thermoset composites”. In: *Composites Part A: Applied Science and Manufacturing* 151 (2021), p. 106600. DOI: 10.1016/j.compositesa.2021.106600.

[37] D. S. Cairns et al. “Design and manufacturing considerations for ply drops in composite structures”. In: *Composites Part B: Engineering* 30.5 (1999), pp. 523–534. DOI: 10.1016/S1359-8368(98)00043-2.

[38] B. R. Vidyashankar and A. V. Krishna Murty. “Analysis of laminates with ply drops”. In: *Composites Science and Technology* 61.5 (2001), pp. 749–758. DOI: 10.1016/S0266-3538(01)00010-0.

[39] R. Harikumar et al. “Fabrication and Experimental Analysis of Copper Wire Embedded Glass Fiber Reinforced Polymer Composites”. In: *Materials Today: Proceedings* 5.1, Part 3 (2018), pp. 17520–17526. DOI: 10.1016/j.matpr.2018.03.015.

[40] P.E. Irving and C. Thiagarajan. “Fatigue damage characterization in carbon fibre composite materials using an electrical potential technique”. In: *Smart Materials and Structures* 7.4 (1998), pp. 456–466. DOI: 10.1088/0964-1726/7/4/004. URL: https://doi.org/10.1088/0964-1726/7/4/004.

[41] Ming-Hsiang Shih and Wen-Pei Sung. “Application of Digital Image Correlation Method for Analysing Crack Variation of Reinforced Concrete Beams”. In: *Sādhanā – Academy Proceedings in Engineering Sciences* 38.4 (Aug. 2013). MS received 1 October 2012; revised 23 February 2013; accepted 23 March 2013, pp. 723–741. DOI: 10.1007/s12046-013-0141-5.

[42] LVDT.co.uk. *How LVDTs Work – The LVDT Operating Principle*. https://lvdt.co.uk/lvdt-info/how-lvdts-work/. Accessed: 2025-10-15. n.d.

[43] Genjin Liu and Yining Ding. “Self-monitoring and Localization of Crack of Concrete Beam with Fibers and Carbon Black Subjected to Bending”. In: *Proceedings of the 5th International Conference on Rehabilitation and Maintenance in Civil Engineering*. Ed. by Genjin Liu and Yining Ding. Vol. 225. Lecture Notes in Civil Engineering. Springer, 2022, pp. 179–188. DOI: 10.1007/978-981-16-9348-9_16. URL: https://link.springer.com/chapter/10.1007/978-981-16-9348-9_16.

[44] Lianxi Shen et al. “Modeling and analysis of the electrical resistance measurement of carbon fiber polymer–matrix composites”. In: *Composites Science and Technology* 67.11-12 (2007), pp. 2513–2520. DOI: 10.1016/j.compscitech.2006.12.020.

[45] National Instruments. *Application Note 078: Strain Gauge Measurement – A Tutorial*. Accessed on October 25, 2025. 2004. URL: https://www.ni.com/pdf/manuals/3700/ni_an078.pdf.

[46] Shu-Yang Wang et al. “A Review on Resistance-Based Self-Sensing of Carbon Fiber-Reinforced Polymer Subjected to Loads”. In: *Advanced Engineering Materials* 27.13 (2025). DOI: 10.1002/adem.202500244. URL: https://onlinelibrary.wiley.com/doi/10.1002/adem.202500244.

[47] B.-G. Kang, J. Hannawald, and W. Brameshuber. “Electrical resistance measurement for damage analysis of carbon yarns”. In: *Materials and Structures* 44.7 (2011), pp. 1113–1122. DOI: 10.1617/s11527-010-9687-4.

[48] Xiaojun Wang and Deborah D.L. Chung. “Real-time monitoring of fatigue damage and dynamic strain in carbon fiber polymer-matrix composite by electrical resistance measurement”. In: *Composites Science and Technology* 59.1 (1999), pp. 51–61. DOI: 10.1016/S0266-3538(98)00158-4.

[49] Huang Huang, Caiqian Yang, and Zhishen Wu. “Electrical sensing properties of carbon fiber reinforced plastic strips for detecting low-level strains”. In: *Smart Materials and Structures* 21.3 (2012), p. 035013. DOI: 10.1088/0964-1726/21/3/035013.

[50] Y. Goldfeld, T. Quadflieg, and T. Gries. “Sensing capabilities of carbon based TRC beam from slack to pull-out mechanism”. In: *Composite Structures* 181 (2017), pp. 294–305. DOI: 10.1016/j.compstruct.2017.08.102.

[51] Jun Deng et al. “Debonding damage detection of the CFRP–concrete interface based on piezoelectric ceramics by the electromechanical impedance method”. In: *Construction and Building Materials* 303 (2021), p. 124431. DOI: 10.1016/j.conbuildmat.2021.124431. URL: https://www.sciencedirect.com/science/article/pii/S0950061821021899.

[52] M. Zhu, Y. Liu, and X. Li. “Bond degradation and EMI□based monitoring of CFRP to concrete interfaces subjected to cyclic environmental exposure”. In: *International Journal of Adhesion and Adhesives* 116 (2022), p. 103191. DOI: 10.1016/j.ijadhadh.2022.103191. URL: https://www.sciencedirect.com/science/article/pii/S0141029622003546.

[53] J.K. Kim et al. “Measurement of the gauge factor of carbon fiber and its application to sensors”. In: *Microelectronic Engineering* 85.5–6 (2008), pp. 787–791. DOI: 10.1016/j.mee.2008.01.067.

A Concrete Manufacturing

(a) (b) (c)

(d) (e) (f)

Figure A.1: : (a) Oiled moulds, (b) Concrete mix in concrete mixer, (c) Mix in moulds, (d) Moulds on vibration tables, (e) Specimen sealed and cured for one day at room temperature, (f) Unmoulded specimens in humidity chamber for next 27 days

B Composite preparation

B.1. Sample Preparation

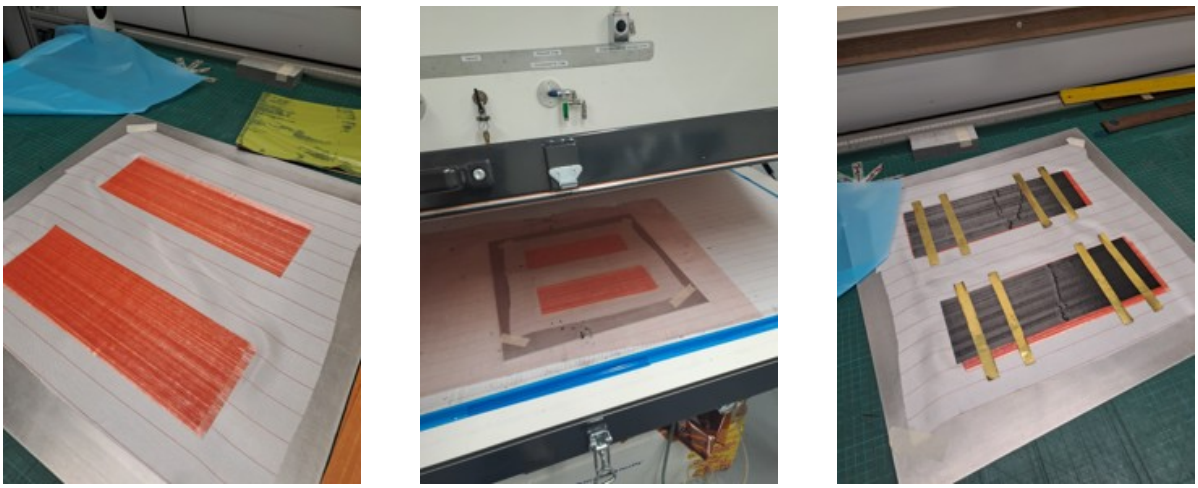

(a) (b) (c)

Figure B.1: (a) Glass prepregs on peelply and aluminium plate, (b) Debulking at 1 Bar after every 3 plies, (c) Adding carbon prepreg with copper strip and electric paint

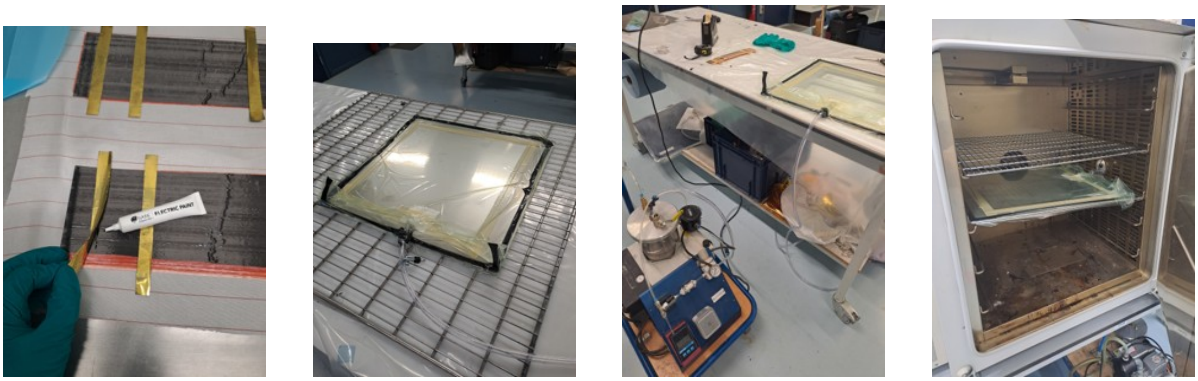

(d) (e) (f) (g)

Figure B.1: (d) Result before adding top glass layer, (e) Specimen sealed with aluminium plate and vacuum bag, (f) Testing vacuum bag with machine, (g) Specimen in oven for one hour at 125°C while applying continuous vacuum

B.2. Autoclave Curing process

Autoclave settings

Pressure: Ramp endlevel = 7.00 Bar, Rate 1.00 Bar/min Temperature: Ramp Endlevel = 125 Celcius, Rate: 1.00 Celcius/min Hold: 1 hour Cool: Ramp Endlevel = 40 Degrees Celcius, Rate 2.00 Celcius/min Pressure Release: 1.00 Bar, Rate 1.00 Bar/min

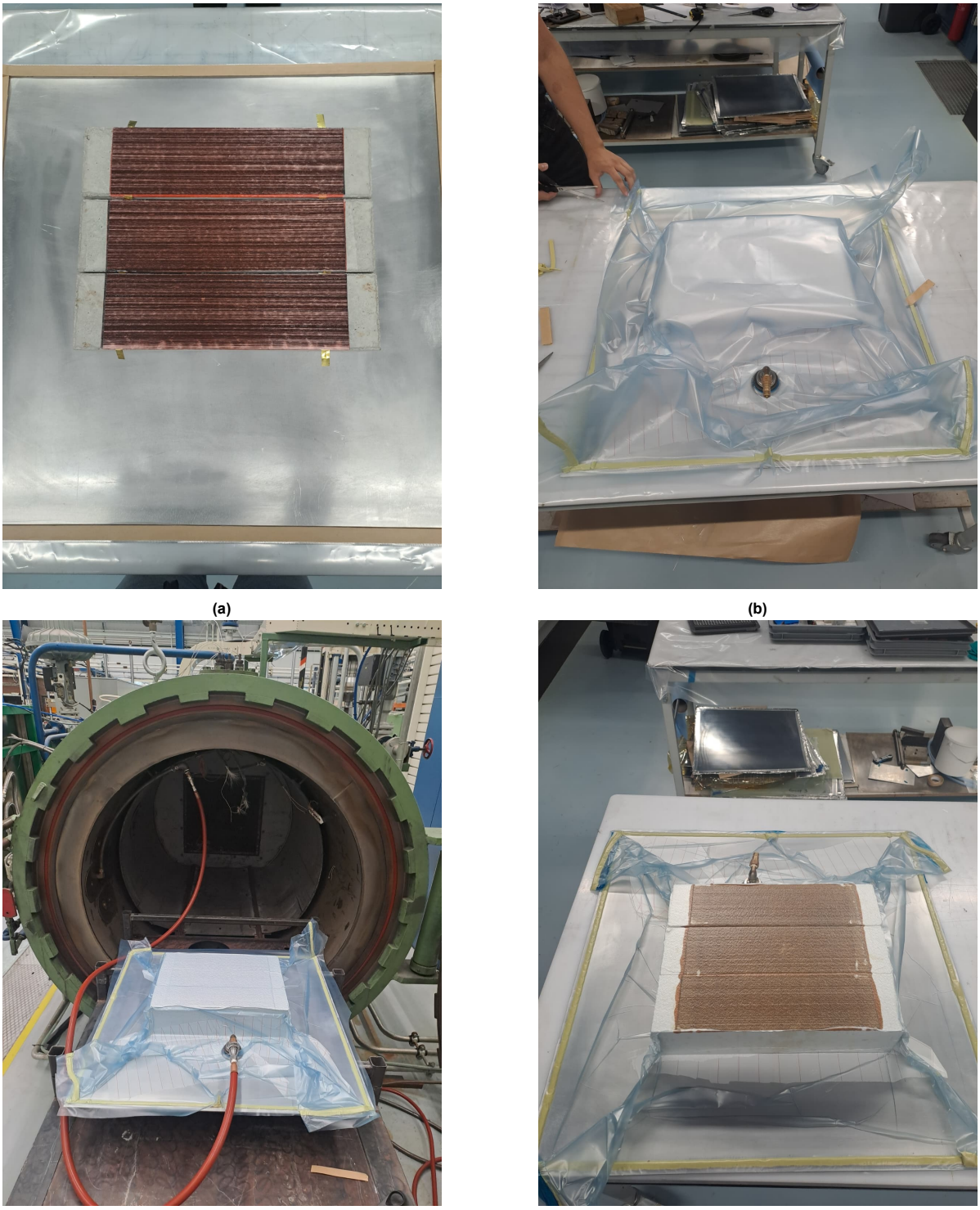

(a) (b) (c) (d)

Figure B.2: (a) Specimens before curing, (b) Preparing vacuumbag with additional peelply and breather on top of the composite, (c) Specimen before placing in autoclave, (d) Specimens after autoclave

C Mechanochromic effect

C.1. Iteration 1

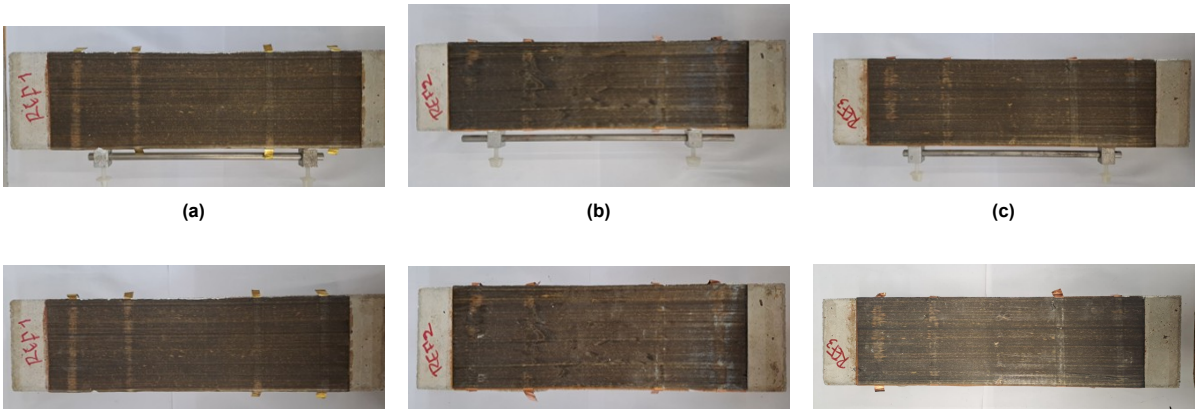

(a) (b) (c)

(d) (e) (f)

Figure C.1: (a) REF1 before testing, (b) REF2 before testing, (c) REF3 before testing, (d) REF1 after testing, (e) REF2 after testing, (f) REF3 after testing.

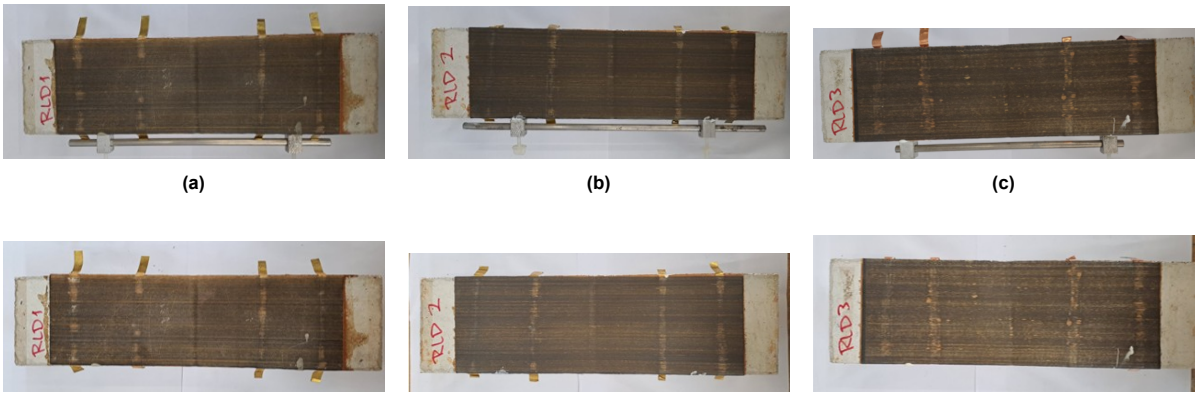

(a) (b) (c)

(d) (e) (f)

Figure C.2: (a) RLD1 before testing, (b) RLD2 before testing, (c) RLD3 before testing, (d) RLD1 after testing, (e) RLD2 after testing, (f) RLD3 after testing.

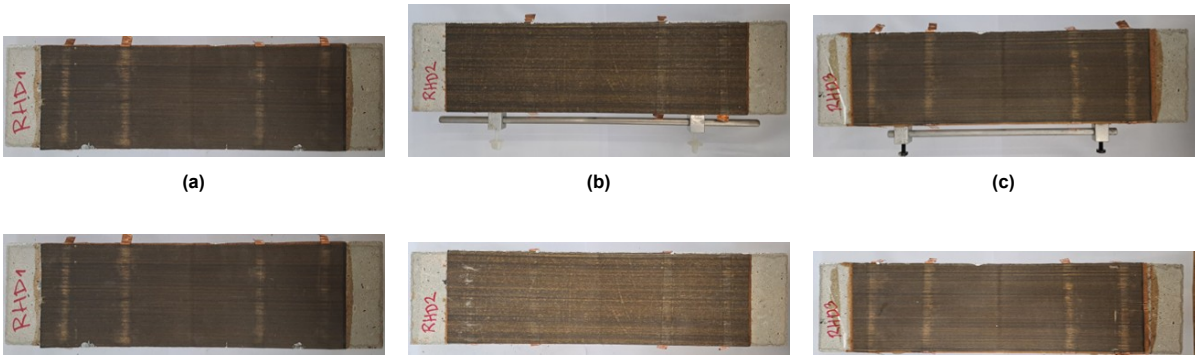

(a) (b) (c)

(d) (e) (f)

Figure C.3: (a) RHD1 before testing, (b) RHD2 before testing, (c) RHD3 before testing, (d) RHD1 after testing, (e) RHD2 after testing, (f) RHD3 after testing.

C.2. Iteration 2

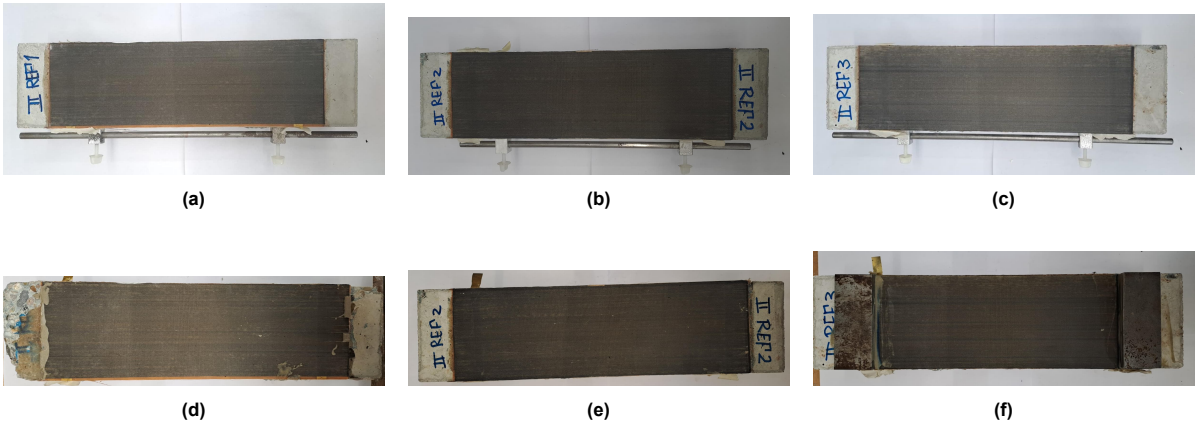

(a) (b) (c)

(d) (e) (f)

Figure C.4: (a) 2-REF1 before testing, (b) 2-REF2 before testing, (c) 2-REF3 before testing, (d) 2-REF1 after testing, (e) 2-REF2 after testing, (f) 2-REF3 after testing.

D Observed crack patterns after testing

D.1. Iteration 1 specimens

Figure D.1: Specimen REF1 after testing

Figure D.2: Specimen REF2 after testing

Figure D.3: Specimen REF3 after testing

Figure D.4: Specimen RLD1 after testing

Figure D.5: Specimen RLD2 after testing

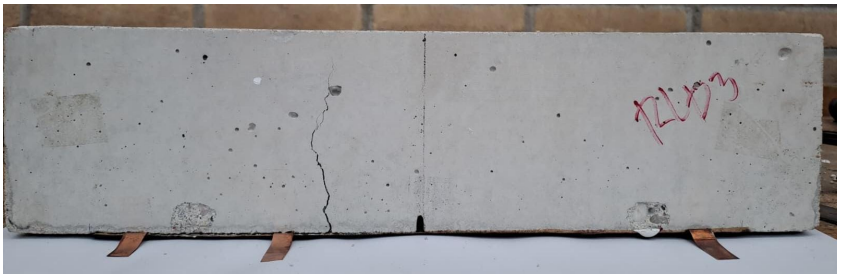

Figure D.6: Specimen RLD3 after testing

Figure D.7: Specimen RHD1 after testing

Figure D.8: Specimen RHD2 after testing

Figure D.9: Specimen RHD3 after testing

D.2. Iteration 2 specimens

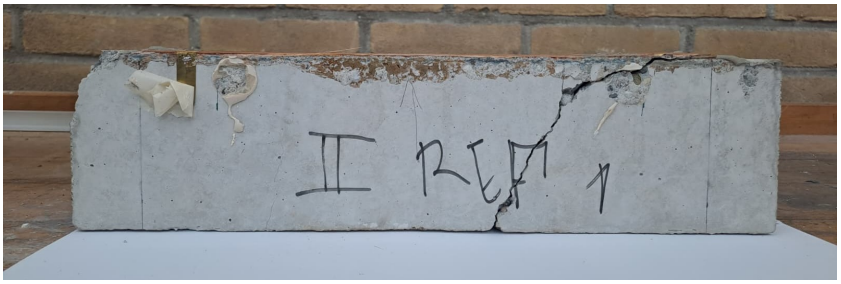

Figure D.10: Specimen 2-REF1 after testing

Figure D.11: Specimen 2-REF2 after testing

Figure D.12: Specimen 2-REF3 after testing

Figure D.13: Close up crack

Figure D.14: Close up crack, including crackline along composite